Universidade de São Paulo
Instituto de Astronomia, Geofísica e Ciências Atmosféricas
Departamento de Astronomia

Edgar Bueno dos Santos

Numerical modeling of mantle dynamics and its interaction with cratonic keels of the continental lithosphere

São Paulo
2024

Edgar Bueno dos Santos

Numerical modeling of mantle dynamics and its interaction with cratonic keels of the continental lithosphere

Tese apresentada ao Departamento de Geofísica do Instituto de Astronomia, Geofísica e Ciências Atmosféricas da Universidade de São Paulo como requisito parcial para a obtenção do título de Doutor em Ciências.

Área de Concentração: Geofísica
Orientador: Prof. Dr. Victor Sacek

São Paulo

2024

Agradecimentos

Gostaria de agradecer primeiramente ao meu orientador Prof. Dr. Victor Sacek que me inspirou e participou da minha formação científica. Agradeço pela amizade e por todos os ensinamentos e diálogos, que não só me guiaram no desenvolvimento desta tese e da minha carreira, mas também me ajudaram no meu desenvolvimento como pessoa. Além de um excelente orientador eu ganhei um grande amigo. Obrigado.

Agradeço à Coordenação de Aperfeiçoamento de Pessoal de Nível Superior - Brasil (CAPES) pela concessão da bolsa de doutorado. À Petrobras e à Fundação de Amparo à Pesquisa do Estado de São Paulo (FAPESP) pelo apoio financeiro para a realização desta pesquisa. Aos professores, funcionários, alunos do IAG e à comunidade USP que de alguma forma contribuíram para o desenvolvimento deste trabalho.

Um agradecimento em especial à Cris, Fefo, Gianee e Moon, por todos os momentos que compartilhamos nos últimos anos. Vocês sempre estiveram presentes e dispostos a me ajudar e me ouvir. Amo vocês!

Agradeço a toda minha família. Em especial, aos meus pais Valter e Nelci por todo o amor, carinho e educação. Por sempre acreditarem no meu potencial e por todos os sacrifícios que permitiram que eu pudesse concluir este trabalho.

Esta tese/dissertação foi escrita em LaTeX com a classe IAGTESE, para teses e dissertações do IAG.

Resumo

SANTOS, E. B. (2024). Modelagem numérica da dinâmica do manto e sua interação com quilhas cratônicas da litosfera continental, Tese de Doutorado, Instituto de Astronomia, Geofísica e Ciências Atmosféricas, Universidade de São Paulo, São Paulo.

Diferentes modelos de espessura da litosfera baseados em tomografia sísmica indicam que variações laterais da espessura litosférica podem ser abruptas, especialmente ao longo das bordas dos crátons, onde a espessura pode variar mais de 100 km ao redor dos limites da quilha cratônica. Essas variações laterais podem afetar o fluxo do manto astenosférico durante o movimento das placas litosféricas, o que pode eventualmente impactar o campo de esforços no interior do manto e da crosta e afetar a evolução topográfica das margens continentais. A quantificação correta da interação geodinâmica entre a astenosfera e as quilhas cratônicas envolve processos de escoamento não-lineares e cenários com configuração geométrica complexa. Por essa razão, o uso de códigos numéricos é uma abordagem natural para estudar esses problemas geodinâmicos. No presente trabalho, modelos numéricos termo-mecânicos foram usados com reologia realista para a crosta e o manto para avaliar como o fluxo astenosférico sob quilhas cratônicas afetou a topografia e o campo de esforços no interior da placa litosférica. Foram testados diferentes valores de espessura para a quilha cratônica e a velocidade relativa entre a litosfera e a base do manto superior. Foi possível observar que o fluxo horizontal da astenosfera sob a quilha cratônica induz esforços distensivos na crosta quando o fluxo astenosférico ocorre da litosfera mais fina em direção ao cráton, definido aqui como “proa cratônica”. Por outro lado, esforços compressivos na crosta são observados na região onde o fluxo astenosférico ocorre do cráton em direção à litosfera mais fina, uma porção definida aqui como “popa cratônica”. A magni-

tude dos esforços aumenta com maiores velocidades e uma quilha cratônica mais espessa, alcançando uma magnitude de ±8 - 10 MPa na crosta cratônica nos cenários com uma quilha cratônica com 200 km de espessura. O fluxo astenosférico sob a quilha cratônica induz convecção de borda (do inglês *edge-driven convection*) com maior vigor adjacente à popa cratônica, onde são observadas perturbações topográficas, especialmente em cenários com quilha cratônica espessa, resultando em topografia dinâmica negativa de centenas de metros. Propomos que esse mecanismo de subsidência dinâmica pode explicar parte da topografia residual negativa observada ao longo da margem sul da Austrália, induzida pelo rápido movimento para o norte (7,4 cm/ano) da placa combinado com a presença de uma quilha litosférica espessa no continente. Adicionalmente, a inclinação continental norte-sul observada na Austrália durante o Mioceno pode ser parcialmente explicada como a desaceleração da placa e a consequente redução da amplitude da topografia dinâmica no continente e nas regiões marginais durante os últimos 30 milhões de anos.

Palavras-chaves: esforços intraplacas, modelagem numérica, quilhas cratônicas, covecção do manto

Abstract

SANTOS, E. B. (2024). Numerical modeling of mantle dynamics and its interaction with cratonic keels of the continental lithosphere, Tese de Doutorado, Instituto de Astronomia, Geofísica e Ciências Atmosféricas, Universidade de São Paulo, São Paulo.

Different lithosphere thickness models based on seismic tomography indicate that lateral variations of lithospheric thickness can be abrupt, especially along the borders of cratons, where the thickness can vary more than 100 km around the limits of the cratonic keel. These lateral variations can affect the flow of the asthenospheric mantle during the movement of the lithospheric plates which can eventually impact the stress field in the interior of the mantle and crust and affect the topographic evolution of continental margins. The correct quantification of the geodynamic interaction between asthenosphere and cratonic keels involves non-linear flow and scenarios with complex geometric configurations. For this reason, the use of numerical codes is a natural approach to study these geodynamic problems. In the present work, thermo-mechanical numerical models were used with realistic rheology for the crust and mantle to assess how the asthenospheric flow under cratonic keels affected the topography and intraplate stress field. Different thickness values for the cratonic keel and the relative speed between the lithosphere and the base of the upper mantle were tested. It was possible to observe that the horizontal flow of the asthenosphere under the cratonic keel induces extensional stresses in the crust when the asthenospheric flow occurs from the thinner lithosphere towards the craton, defined here as the "cratonic bow". On the other hand, compressional stresses in the crust are observed in the region where the asthenospheric flow occurs from the craton towards the thinner lithosphere, a portion defined here as the "cratonic stern". The magnitude of the stresses

increases with higher speeds and a thicker cratonic keel, reaching a magnitude of $\pm 8 - 10$ MPa in the cratonic crust in the scenarios with a cratonic keel with 200 km in thickness. The asthenospheric flow under the cratonic keel induces edge-driven convection with larger vigor adjacent to the cratonic stern, where topographic perturbations are observed especially in scenarios with thick cratonic keel, resulting in negative dynamic topography of hundreds of meters. I propose that this mechanism of dynamic subsidence can explain part of the negative residual topography observed along the southern Australian margin, induced by the fast ($\sim$ 7.4 cm/year) northward movement of the plate combined with the presence of a thick lithospheric keel in the continent. Furthermore, the north-south continental tilt observed in Australia during the Miocene can be partially explained as the slowdown of the plate and consequent reduction of the dynamic topography amplitude in the continent and marginal regions during the last 30 Myr.

Key-words: intraplate stress, numerical modeling, cratonic keels, mantle convection

List of Figures

List of Tables

List of Symbols

The main variables and parameters used in the manuscript are listed here. Other temporary symbols used in specific parts of the thesis are not presented in this list.

Symbol	Meaning
x, y	Horizontal coordinates
z	Vertical coordinate
t	Time
g	Gravity
T	Temperature
T_b	Basal temperature
T_0	Top temperature
α	Coefficient of thermal expansion
R	Gas constant
κ	Thermal diffusivity
u	Velocity of the fluid
ρ	Density
A	Pre-exponential scaling factor
C	Viscosity scaling factor
P	Pressure
V	Activation volume
E_a	Activation Energy
H	Heat production
c_p	Specific heat witch constant pressure

Symbol	Meaning
η	Viscosity
σ	Stress tensor
ϵ	Strain rate tensor
c_0	Internal cohesion
μ	Coefficient of friction
n	Power law exponent

Contents

Chapter 1

Introduction

1.1 Thick continental lithosphere and the asthenospheric mantle flow

Plate tectonics is mainly guided by the downward pull of relatively cold oceanic plates in subduction (Lithgow-Bertelloni and Richards, 1998). In this context, the continental lithosphere, with thicker crust relative to the oceanic lithosphere, are buoyant and gravitationally stable, being preserved at the surface in the geological time scale, and the horizontal movement of the continents in the plate tectonics regime is mainly guided by the interaction with adjacent oceanic plates. In general, lithospheric plates with a large fraction of continental area present lower horizontal speed relative to oceanic plates (Forsyth and Uyeda, 1975), indicating that continental plates can exert a relevant drag force resisting the plate movement. Furthermore, the thick continental lithosphere, especially in cratonic domains, can impose an additional resistance to the horizontal movement of the lithosphere (Conrad and Lithgow-Bertelloni, 2006). Conversely, the viscous flow of the asthenosphere around the cratonic keels can impose stress in the lithosphere that can propagate to the crust. This interaction depends on the rheology of the mantle and the lateral variation of lithospheric thickness.

The largest lateral variations of lithospheric thickness occur mainly along the edges of cratonic keels, where the thickness of the lithosphere can reach over 300 km in Archean cratons (Steinberger and Becker, 2016), significantly thicker than the oceanic lithospheres (Figure 1.1). In cratonic regions in Africa, South America, North America, and Australia, the lithospheric thickness surpasses 250 km depth. The stability of cratons for billions of years is probably a consequence of the distinct chemical composition relative to the mean composition of the upper mantle, with the cratons more depleted in volatile and mafic

components (Jordan, 1975; Pollack, 1986). The depletion in volatiles, specially water, increases the effective viscosity of the depleted mantle, contributing for the rigidity and stability of cratons (Doin et al., 1997; O'Neill et al., 2008).

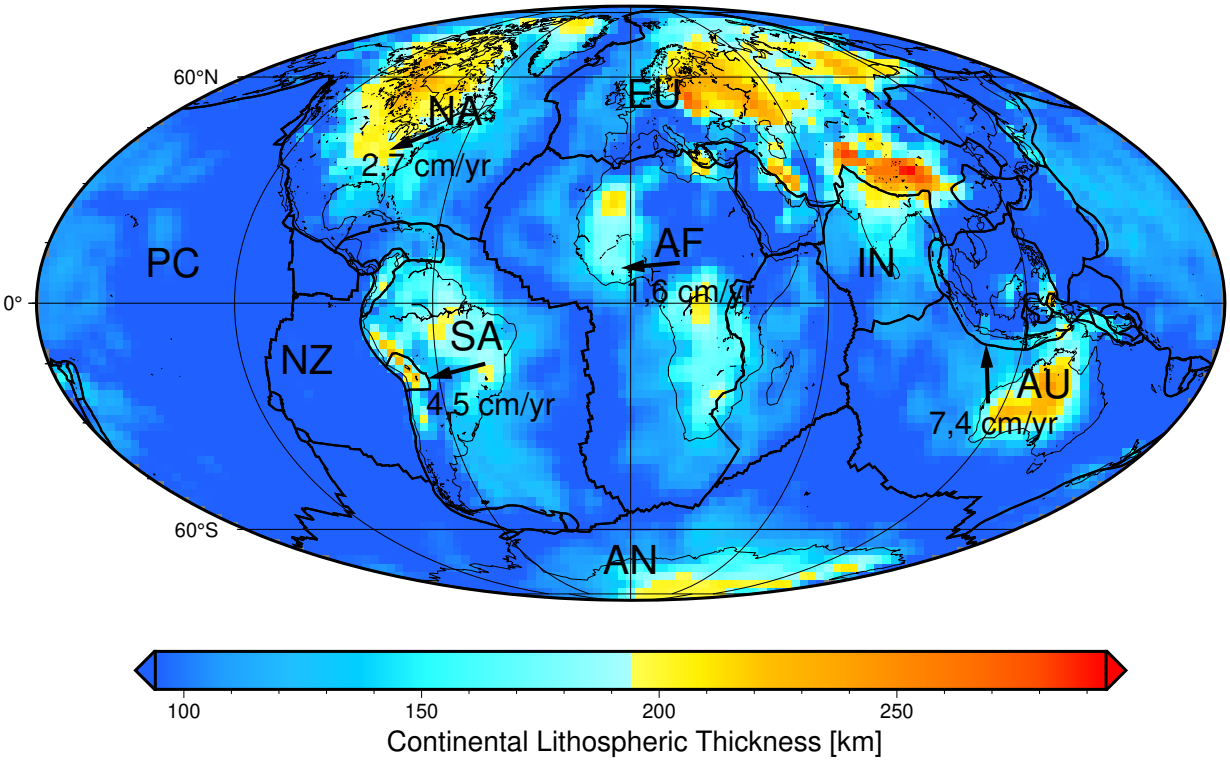

Figure 1.1: Continental lithospheric thickness map showing plate boundaries and the velocity in the hotspot reference frame. Continental thickness based on Priestley and McKenzie (2013). The plate boundaries are given by Bird (2003). The velocities are based on the hotspot reference frame HS3- Nuvel 1A from Gripp and Gordon (2002).

Due to the complex rheology of the mantle and geometry of the cratonic keel, the use of numerical geodynamic models is essential to appropriately simulate the interaction between the asthenospheric mantle and the base of the continental lithosphere. In the last decades, many works explored the lateral variation in continental lithospheric thickness by analyzing the interaction between the continental lithosphere and mantle convection in numerical models (e.g. Lenardic et al., 2003; Cooper et al., 2004).

One important effect of the geographical variation in lithospheric thickness is induced by the large lateral temperature differences, where King and Anderson (1998) showed that such variations in lithospheric thickness can induce small-scale convection cells in the asthenospheric mantle (Figure 1.2). These small-scale convections have been used to explain intraplate volcanism without the presence of mantle plumes and may contribute to volcanic activity (King, 2005; King and Ritsema, 2000), and relatively high shear wave velocities

due to the presence of cold material in downward convective motion (King and Ritsema, 2000). These small-scale convections generated at the edges of the thick lithosphere can contribute to anomalies in dynamic topography (Shahnas and Pysklywec, 2004; Sacek, 2017). Petersen et al. (2010) verified the influence of small-scale convection on the stratigraphy of sedimentary basins. Sacek and Ussami (2013) demonstrated how the geometry of divergent margins can induce differential subsidence along the margin. Salazar-Mora and Sacek (2021) showed that the lithospheric mantle viscosity and density contrast control the behavior of the edges of cratonic keels and the development of convective cells in the asthenospheric mantle adjacent to the lithospheric keel.

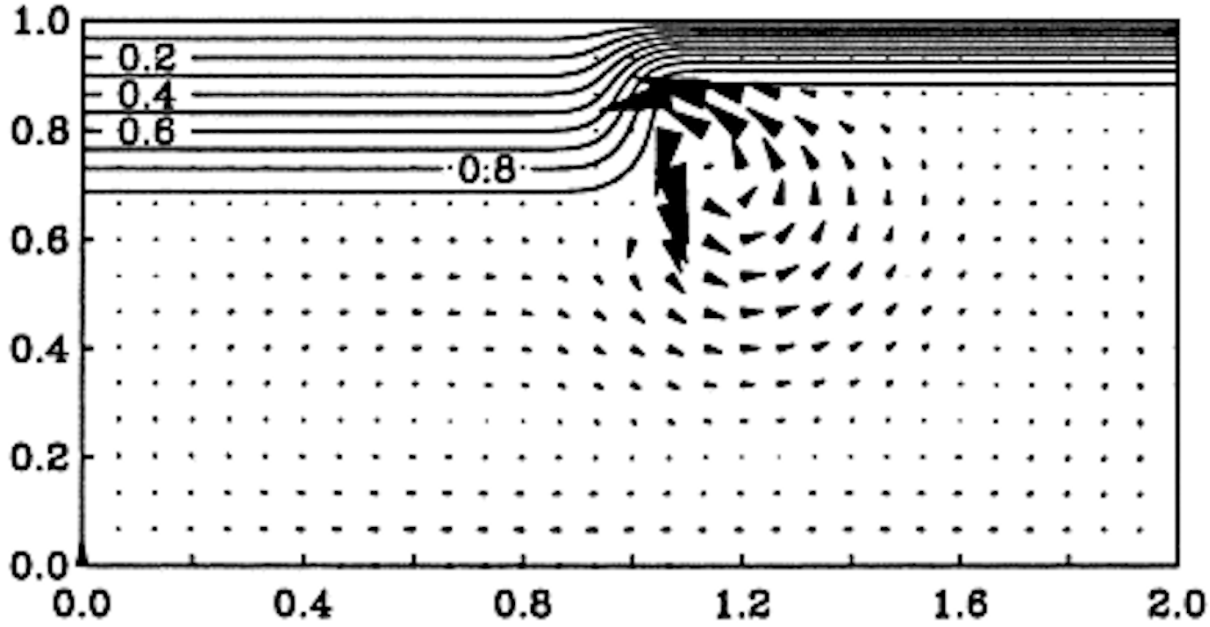

Figure 1.2: Edge-driven convection observed in a numerical scenario with a lithosphere with lateral variation in thickness. The numbers in the axes and isotherms are non-dimensional. Extracted from King and Anderson (1998).

Additionally, Farrington et al. (2010) investigated how continents with lateral variation in lithospheric thickness interact with the asthenospheric mantle in different continental velocity regimes, analyzing how these small-scale convections evolve in 3D models with linear rheology, showing that the convective pattern under and around the continents depends on the speed of the plate.

Hu et al. (2017) simulated the flow of the asthenospheric mantle around cratonic keels in South America, using a linear rheology function of temperature, pressure, and composition, where continents and cratons are 1000 times more viscous than the asthenosphere, allowing

them to be preserved during the subduction process. Hu et al. (2017) point out that the role of cratonic keels in the anisotropy of the mantle is smaller than that of the subducting plate.

However, the correct representation of the stress field in the lithosphere and the impact on the topographic evolution due to the interaction of the asthenospheric mantle flow around a thick continental lithosphere depends on the incorporation of non-linear rheology, especially in the lithosphere, where non-linear creep flow and plastic behavior dominate (Burov, 2011).

1.2 The purpose of this work

Aimed to further contribute to the study of the interactions between thick cratonic lithosphere and the asthenospheric mantle, this work evaluates the interaction between asthenospheric mantle flow and a thick cratonic lithosphere, taking into account realistic rheology for the mantle and crust. In this work, I used a thermo-mechanical numerical model to simulate the relative movement of cratonic keels over the asthenospheric mantle to evaluate how this motion affects the mantle flow around cratonic regions, modifies the intraplate stress field, and induces vertical displacements in the lithosphere.

Chapter 2 presents the theoretical principles underlying mantle convection, leading to the formulation of the key equations for the conservation of mass, momentum, and energy. Furthermore, it includes a review of the main approximations and constitutive equations of material properties.

Chapter 3 describes the thermo-mechanical numerical model setup used to simulate the relative movement of cratonic keels over the asthenospheric mantle. Chapter 4 shows the application of the model described in the previous chapter evaluating the influence of the asthenospheric flow under cratonic keels and its impact on the intraplate stress field and dynamic topography.

Chapter 5 presents a discussion on the implications of the results, especially for a fast-moving lithosphere (v = 8.0 cm/yr). The results are compared with the Indo-Australia plate which presents a thick cratonic keel and a high velocity.

Finally, Chapter 6 provides the conclusions of the thesis, highlighting the contributions of the numerical models presented and offering perspectives for future work.

Chapter 2

The Physics of Mantle Convection

2.1 Introduction

Usually, the term fluid is used to refer to a state of matter, either liquid or gaseous. However, the definition of a fluid is a material that continuously deforms under applied shear stress, or external force, and in its tendency to deform irrecoverably (Ricard, 2015). Therefore, any material with elastic or non-deformable behavior, whether possessing a crystalline or disordered structure, can undergo deformation when subjected to an external force or shear stress for a sufficiently prolonged time.

Geologic processes associated with mantle convection typically occur over millions of years (on the order of 10 My). Over such extended timescales, the mantle, despite being a solid capable of transmitting shear waves and possessing greater strength than steel, can be considered as a fluid.

Many materials can behave as solids over a short period and like fluids over a long period. The rheological behavior of a material can be defined by the Maxwell time (τ_M), a characteristic time given by the ratio between the dynamic viscosity (η) and the elasticity (μ_r):

$$\tau_M = \frac{\eta}{\mu_r} \tag{2.1}$$

Typical values of dynamic viscosity and elasticity in the mantle are $\eta \approx 10^{21}$ Pa.s and $\mu_r \approx 10^{11}$ Pa, so the Maxwell time for the mantle is of the order of a few hundreds or thousands of years.

The physics of fluid behavior is based on the continuum hypothesis, so quantities such as density, temperature, and velocity must be defined continuously at all points. The

following sections will describe the mathematical formulations for fluid dynamics in mantle convection.

2.2 Heat Transfer

The rheology of solids is a temperature-dependent function (Turcotte and Schubert, 2014). The rheology of mantle rocks is directly related to temperature as a function of depth, which, in turn, depends on the rate at which the Earth's interior dissipates heat through its surface. Thus, to understand the mechanical behavior of the Earth, it is necessary to understand its thermal structure. In this chapter, the basic equations of heat transfer through thermal conduction will be introduced.

2.2.1 Types of Heat Transfer

There are three mechanisms for heat transfer, they are conduction, convection, and radiation. Heat transfer by conduction is a diffusive process and occurs through the step-by-step transmission of the kinetic energy of a molecule when it collides with other molecules. Thus, for heat conduction to occur, there must be a temperature gradient. Heat conduction occurs without noticing the movement of matter on a macroscopic scale.

Unlike thermal conduction, thermal convection is associated with movements in the material medium. It occurs when a hotter fluid enters a region of lower temperature, and thus heats that region. Similarly, when a cooler fluid enters a warmer region it will cool the region, producing mass displacement.

The transfer of heat by thermal radiation occurs through electromagnetic waves emitted by heated bodies. Examples of this type of heat transfer include the thermal radiation from the Sun and incandescent lamps.

In the interior of rocky planets, the free path of electromagnetic waves is very small, being absorbed by the rock and retransmitted essentially by thermal conduction. Consequently, the transport of heat within the planet can be effectively represented by thermal conduction and convection, and it is reasonable to neglect thermal radiation for the study of the thermal dynamics of the planet.

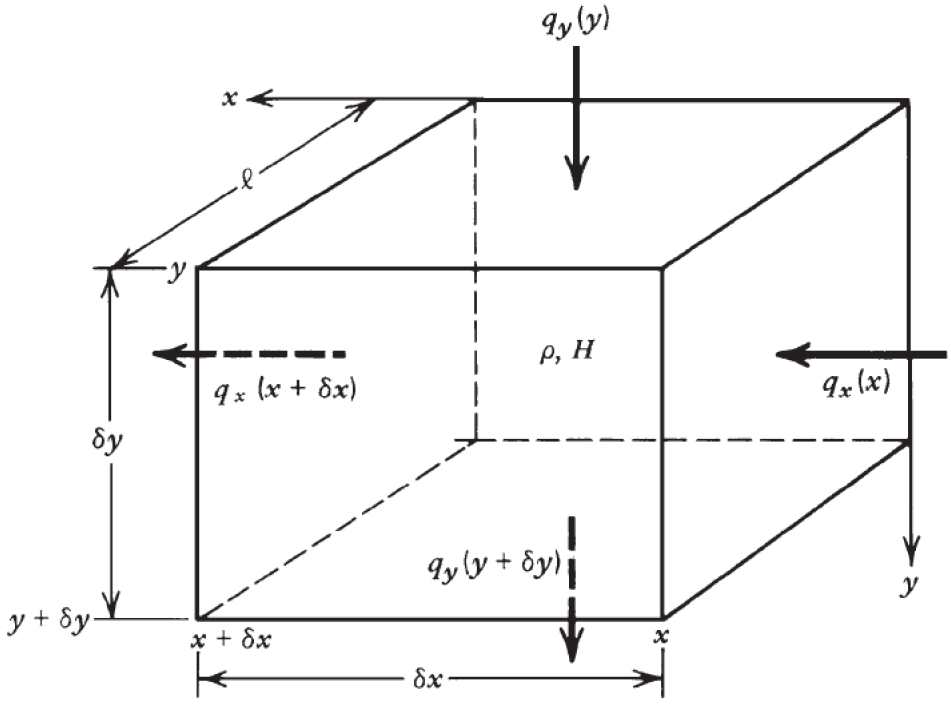

Figure 2.1: Heat flow diagram in a rectangular box. Extracted from Turcotte and Schubert (2014).

2.2.2 Fourier's Law

Fourier's law, also known as the law of thermal conduction, is the principle for the transport of heat by conduction. Such a law states that the heat flow through a material is proportional to the negative temperature gradient.

$$q = -k\boldsymbol{grad}(T) \tag{2.2}$$

or in tensor form

$$q_i = -k\frac{dT}{dx_i} \tag{2.3}$$

where k is the coefficient of thermal conductivity. The minus sign in 2.3 is because heat flows in the direction of decreasing temperature.

2.2.3 Heat Conduction in the Steady State

Consider a rectangular box with infinitesimal thicknesses δx_i, δx_j and δx_k as shown in Figure 2.1.

We can write the heat flux in each direction as q_{x_i}. The rate at which heat flows into the box in the direction x_i can be expressed as $q_{x_i}(x_i)\delta x_j \delta x_k$ and the rate at which heat

flows out of the box in the same direction as $q_{x_i}(x_i + \delta x_i)\delta x_j \delta x_k$.

Thus, the heat flux leaving the box can be written as

$$\begin{aligned} &\left[q_{x_i}(x_i + \delta x_i) - q_{x_i}(x_i)\right] \delta x_j \delta x_k + \\ &+ \left[q_{x_j}(x_j + \delta x_j) - q_{x_j}(x_j)\right] \delta x_i \delta x_k + \\ &+ \left[q_{x_k}(x_k + \delta x_k) - q_{x_k}(x_k)\right] \delta x_i \delta x_j \end{aligned} \tag{2.4}$$

or in tensor form

$$\left[q_{x_i}(x_i + \delta x_i) - q_{x_i}(x_i)\right] \delta x_j \delta x_k \tag{2.5}$$

Since δx_i, δx_j and δx_k are infinitesimals we can expand the terms $q_{x_i}(x_i + \partial x_i)$ through the Taylor series. So, we can write the terms as

$$q_{x_i}(x_i + \delta x_i) = q_{x_i}(x_i) + \delta x_i \frac{\partial q_i}{\partial x_i} + ... \tag{2.6}$$

Using the Taylor series approximation given by 2.6 in 2.5 we obtain

$$q_{x_i}(x_i + \delta x_i) - q_{x_i}(x_i) = \frac{\partial q_{x_i}}{\partial x_i} \delta x_i \delta x_j \delta x_k \tag{2.7}$$

replacing 2.3 in the above equation, we have:

$$\delta x_i \delta x_j \delta x_k \left[-k \frac{\partial}{\partial x_i} \left(\frac{\partial T}{\partial x_i}\right)\right] \tag{2.8}$$

The equation 2.8 gives the flow leaving the rectangular box, per unit of time and unit of area. As we are dealing with a stationary case, i.e., without variations in flow or temperature over time, if the flow leaving the box is non-zero, this heat must be generated internally. Thus, if we consider H to be the rate of heat production per unit of mass and volume, then the heat generated internally is given by $\rho H \delta x_i \delta x_j \delta x_k$. So, from 2.8 we have

$$\delta x_i \delta x_j \delta x_k \left[-k \frac{\partial}{\partial x_i} \left(\frac{\partial T}{\partial x_i}\right)\right] = \rho H \delta x_i \delta x_j \delta x_k \tag{2.9}$$

$$-k \frac{\partial}{\partial x_i} \left(\frac{\partial T}{\partial x_i}\right) = \rho H \tag{2.10}$$

if there are no heat sources inside the box ($H = 0$) and considering k constant the equation

turns into the Laplace's equation

$$\frac{\partial}{\partial x_i}\left(\frac{\partial T}{\partial x_i}\right) = 0 \tag{2.11}$$

2.2.4 Time Dependent Heat Conduction

In the previous section, we obtained an equation that represents the thermal conduction of heat for a steady state, however many of the geological problems involving thermal conduction are time-dependent. Thus, it is necessary to find a relationship to time-dependent thermal conduction.

Starting from equation 2.9, we consider a case in which there is no heat production inside the box ($H = 0$). Thus, a decrease in the temperature of the medium must occur so that the conservation of energy is not violated. This decrease in temperature is proportional to $\partial T/\partial t$, so c is the specific heat of the medium, a volume element of this box $\delta x_i \delta x_j \delta x_k$ needs an energy flow per unit of time given by

$$-\rho c \frac{\partial T}{\partial t} \delta x_i \delta x_j \delta x_k \tag{2.12}$$

the negative sign indicates that the temperature of the box is decreasing as the heat flow is leaving the box, to maintain this rate of decrease in temperature. Thus, we must add the above equation to the right side of equation 2.9, thus obtaining

$$k\frac{\partial}{\partial x_i}\left(\frac{\partial T}{\partial x_i}\right) = \rho c \frac{\partial T}{\partial t} \tag{2.13}$$

this equation is known as the diffusion equation and can commonly be written as

$$\frac{\partial T}{\partial t} = \kappa \frac{\partial}{\partial x_i}\left(\frac{\partial T}{\partial x_i}\right) \tag{2.14}$$

where κ is the thermal diffusivity and is given by

$$\kappa = \frac{k}{\rho c} \tag{2.15}$$

The heat transport presented in equation 2.14 is valid in a medium where thermal convection can be neglected, as in the lithosphere which behaves essentially like a solid in

geological time. However, to adequately represent the heat transport in the asthenospheric mantle, thermal convection must be incorporated, modifying the heat equation. This modification of the heat transport equation together with the mathematical formulation of fluid dynamics will be presented in the next chapter.

2.3 Fluid Dynamics

It is known that the sub-lithospheric mantle behaves like a fluid on geological timescales (Schubert et al., 2001). Thus, to study convective processes in the Earth's mantle, knowledge of fluid mechanics is necessary. In this chapter, the basic equations governing the movement of fluid will be introduced.

2.3.1 Continuity Equation

Let's consider a volume V of space. We can write the mass of fluid present in this volume as:

$$\int_V \rho dV \tag{2.16}$$

where ρ is the fluid density given as a function of the position x_j ($j = 1, 2, 3$, the first two representing the horizontal components, and the third the vertical component). The mass of fluid per unit of time passing through an element $d\boldsymbol{s}$ of the surface around V can be expressed by $\rho\boldsymbol{u} \cdot d\boldsymbol{s}$ where $\boldsymbol{u}$ is the velocity of the fluid, and the direction of $d\boldsymbol{s}$ is along the normal. By convention, we assume $d\boldsymbol{s}$ with the normal pointing outward, and therefore $d\boldsymbol{s}$ is positive if fluid is leaving volume V, and negative if fluid is entering in V. Thus, to obtain the total mass of fluid leaving the volume V per unit of time, we must integrate across the entire closed surface around V, as follows:

$$\oint \rho u_i ds_i \tag{2.17}$$

The change in mass contained in volume V can be written as

$$-\frac{\partial}{\partial t} \int \rho dV \tag{2.18}$$

the negative sign indicates that the mass is leaving the volume V. Thus, from equations (2.17) and (2.18) we have:

$$\frac{\partial}{\partial t}\int \rho dV = -\oint \rho u_i ds_i \tag{2.19}$$

The surface integral can be transformed into a volume integral by the Divergent Theorem

$$\oint \rho u_i ds_i = -\int \frac{\partial}{\partial x_i}(\rho u_i) dV \tag{2.20}$$

and so we have

$$\int \left[\frac{\partial \rho}{\partial t} + \frac{\partial}{\partial x_i}(\rho u_i)\right] dV = 0 \tag{2.21}$$

Since this integral must be true for any volume, the integrand must be zero. Therefore

$$\frac{\partial \rho}{\partial t} + \frac{\partial}{\partial x_i}(\rho u_i) = 0 \tag{2.22}$$

This is the continuity equation, also called the conservation of mass.

2.3.2 Euler's equation

Let us now consider the volume of the fluid. The total force acting on this volume is given by the pressure integral, taken on the surface surrounding the volume. In mathematical terms:

$$-\oint P d\boldsymbol{s} \tag{2.23}$$

where P is the pressure. We can again use the Divergent Theorem and transform this integral into a volume integral

$$-\oint P d\boldsymbol{s} = -\int \boldsymbol{grad}(P) dV \tag{2.24}$$

We can then say that a force $-\boldsymbol{grad}(P)$ acts on a unit volume of the fluid. Thus, we can write Newton's second law for a fluid volume element by equating the force $-\boldsymbol{grad}(P)$, with the mass per unit volume (ρ, density) times the acceleration ($d\boldsymbol{u}/dt$), so we have:

$$\rho \frac{d\boldsymbol{u}}{dt} = -\boldsymbol{grad}(P) \tag{2.25}$$

or in tensor form

$$\rho \frac{du_i}{dt} = -\frac{\partial P}{\partial x_i} \tag{2.26}$$

The derivative on the left side of the above equation does not represent the change in velocity of a fixed point in space, but the change of a given fluid element as it moves through space. We can write this derivative as

$$\frac{du_i}{dt} = \frac{\partial u_i}{\partial t} + u_k \frac{\partial u_i}{\partial x_k} \tag{2.27}$$

Substituting equation (2.27) into equation (2.26) we get

$$\frac{\partial u_i}{\partial t} = -u_k \frac{\partial u_i}{\partial x_k} - \frac{1}{\rho}\frac{\partial P}{\partial x_i} \tag{2.28}$$

The above equation is the fluid's equation of motion, also known as Euler's equation.

2.3.3 Equation of motion of a viscous fluid

So far we have only considered the case of an ideal fluid without viscosity. The continuity equation (2.22) is valid for any fluid, however the Euler equation (2.28) needs some changes when dealing with viscous fluids.

When dealing with a viscous fluid, we must take into account the internal friction between fluid particles, as a function of the viscosity of the medium. Thus, we must sum this contribution due to viscosity in the fluid's equation of motion.

$$\rho \left(\frac{\partial u_i}{\partial t} + u_k \frac{\partial u_i}{\partial x_k} \right) = -\frac{\partial P}{\partial x_i} + \frac{\partial \sigma'_{ik}}{\partial x_k} \tag{2.29}$$

The σ'_{ik} tensor is called the viscosity stress tensor. This tensor is usually written as (Landau and Lifshitz, 1987):

$$\sigma'_{ik} = \eta \left(\frac{\partial u_i}{\partial x_k} + \frac{\partial u_k}{\partial x_i} - \frac{2}{3}\delta_{ik}\frac{\partial u_l}{\partial x_l} \right) \tag{2.30}$$

where η is the viscosity of the fluid and δ_{ik} is the Kronecker delta. We can write the second term of the equation as:

$$\frac{\partial \sigma'_{ik}}{\partial x_k} = \frac{\partial}{\partial x_i}\left[\eta\left(\frac{\partial u_i}{\partial x_k} + \frac{\partial u_k}{\partial x_i} - \frac{2}{3}\frac{\partial u_l}{\partial x_l}\right)\right] \tag{2.31}$$

Therefore, the equation of motion for a viscous fluid can be written as:

$$\rho\left(\frac{\partial u_i}{\partial t} + u_k\frac{\partial u_i}{\partial x_k}\right) = -\frac{\partial P}{\partial x_i} + \frac{\partial}{\partial x_i}\left[\eta\left(\frac{\partial u_i}{\partial x_k} + \frac{\partial u_k}{\partial x_i} - \frac{2}{3}\frac{\partial u_l}{\partial x_l}\right)\right] \tag{2.32}$$

This is the general form of the equation of motion for a viscous fluid, also known as the Navier-Stokes equation (Landau and Lifshitz, 1987).

2.3.4 Energy Equation

Making use of the law of conservation of energy, we need to take into account all energy gains and losses E that occur in a given volume V of fluid per unit of time. So we have:

$$\frac{\partial}{\partial t}\int_V \rho E dV = \int_S u_i \sigma_{ik} dS_j + \int_V \rho u_i F_i dV - \int_S k\frac{\partial T}{\partial x_k} dS_k - \int_S \rho E u_k dS_k + \int_V \rho H dV \tag{2.33}$$

where σ_{ik} is the stress tensor and F_i is an external force acting on the fluid.

The first term on the right side of the equation (2.33) is the rate of work done in the edge region. The second term represents the work done by external forces on each element of the fluid contained in V. In the third term, we have the rate of heat conduction through the surface S of the volume V, and k is the heat conduction coefficient. The fourth term is the rate at which energy convection through S by the prevailing motion. And finally, we have the rate of energy obtained by internal sources of heat (for example, heat from the decay of radioactive elements). We can write the first term as follows:

$$\int_S u_i \sigma_{ik} dS_j = \frac{1}{2}\frac{\partial}{\partial t}\int_V \rho u_i^2 dV + \frac{1}{2}\int_S \rho u_i^2 u_k dS_k - \int_V \rho u_i F_i dV + \int_V \Phi dV \tag{2.34}$$

where

$$\Phi = \frac{\partial u_i}{\partial x_k}\sigma_{ik} \tag{2.35}$$

is called a viscous dissipation function.

The energy E can be written as:

$$E = \frac{1}{2}u_i^2 + c_V T \tag{2.36}$$

where c_V is the specific heat coefficient with constant volume and T is the temperature. In this way we can write the fourth term of the equation (2.33) as follows:

$$-\int_S \rho E u_k dS_k = -\int_S \rho \left(\frac{1}{2}u_i^2 + c_V T\right) u_k dS_k = -\frac{1}{2}\int_S \rho u_i^2 u_k dS_k - \int_V \frac{\partial}{\partial x_k}(\rho u_k c_V T) dV \tag{2.37}$$

Using the divergence theorem we can write the third term of the equation (2.33) as

$$\int_S k\frac{\partial T}{\partial x_k} dS_k = \int_V \frac{\partial}{\partial x_k}\left(k\frac{\partial T}{\partial x_k}\right) dV \tag{2.38}$$

Substituting equations (2.34), (2.37) and (2.38) in equation (2.33):

$$\int_V \frac{\partial}{\partial t}(\rho c_V T) dV = \int_V \frac{\partial}{\partial x_k}\left(k\frac{\partial T}{\partial x_k}\right) dV + \int_V \Phi dV - \int_V \frac{\partial}{\partial x_k}(\rho c_V T u_k) dV + \int_V \rho H dV \tag{2.39}$$

As the above equation must be valid for any volume V, we have:

$$\frac{\partial}{\partial t}(\rho c_V T) + \frac{\partial}{\partial x_k}(\rho c_V T u_k) = \frac{\partial}{\partial x_k}\left(k\frac{\partial T}{\partial x_k}\right) + \Phi + \rho H \tag{2.40}$$

We can also write the above equation in terms of c_P (specific heat coefficient with constant pressure)

$$\rho c_P\left(\frac{\partial T}{\partial t} + u_k\frac{\partial T}{\partial x_k}\right) - \alpha T\left(\frac{\partial p}{\partial t} + u_k\frac{\partial p}{\partial x_k}\right) = \frac{\partial}{\partial x_k}\left(k\frac{\partial T}{\partial x_k}\right) + \Phi + \rho H \tag{2.41}$$

where α is the thermal expansion coefficient. Equation 2.41 is the energy conservation equation for a fluid.

2.4 Fluid Dynamics and Mantle Convection

The previous section (2.3) presented the general fluid dynamics equations. However, for the application of these equations to the interior of the Earth, it is interesting to analyze these equations and identify what they represent in this context.

In the following sections, an analysis of each of the conservation equations presented above will be presented.

2.4.1 Mass Conservation

In the conservation of mass given in equation (2.22), the first term is the only one that is explicitly time-dependent. It describes the time required for a region where the pressure differs from the hydrostatic pressure to expand or compress against viscous forces. Also called viscous isentropic relaxation time scale (Curbelo et al., 2019). This viscous relaxation timescale is, in general, much shorter than the timescales of convective processes in the mantle.

Thus, many of the geodynamic models end up not including this term (Jarvis and Mckenzie, 1980), then we can express the equation (2.22) as:

$$\frac{\partial}{\partial x_i}(\rho u_i) = 0 \tag{2.42}$$

The above equation states that the variation between the mass input and output of a given volume of material is zero. Density may still vary if the material is advected to another region with different pressures, but density variations will always be associated with material movement to a new location. In this approximation, large density variations are considered, as is the case of the Earth's mantle where the density varies approximately 65% from the Earth's surface to the mantle interface with the (Schubert et al., 2001) core.

In some cases, even this density variation is small, as in the case of the Earth's upper mantle, where the average density varies by less than 20%. Thus, some geodynamic models, especially models that use smaller depths, make use of another approximation, assuming that the material is incompressible, i.e., the density is constant. For an incompressible fluid the equation (2.22) can be rewritten as:

$$\frac{\partial u_i}{\partial x_i} = 0 \tag{2.43}$$

2.4.2 Momentum Conservation

The Navier-Stokes equation (2.32) is a general equation for fluid dynamics. The terms on the left side of the equation are the terms that govern the effects of inertia, describing the

acceleration of the material. However, in the Earth's mantle, the movement of materials is so slow that the effects of inertia are negligible. The timescales of convective processes in the mantle are so large that we can neglect these acceleration effects. Thus, the equation (2.32), can be rewritten as:

$$-\frac{\partial P}{\partial x_i} + \frac{\partial}{\partial x_i}\left[\eta\left(\frac{\partial u_i}{\partial x_k} + \frac{\partial u_k}{\partial x_i} - \frac{2}{3}\frac{\partial u_l}{\partial x_l}\right)\right] = 0 \tag{2.44}$$

Removing the inertia term from the momentum equation and applying one of the two common approaches to the conservation of mass (equations 2.42 and 2.43), we have a description of an instantaneous problem. Thus, the velocity and pressure solution does not depend on evolutionary history and can be solved for any given time unless explicitly incorporated by material properties.

The equations 2.32 and 2.44 consider only the stresses applied to the surface of the material. Thus, it is necessary to add the external forces acting on the material. In mantle convection generally, the force of gravity is the only one considered in the models, as its contribution is much greater than that of other forces, such as the electromagnetic force or the Coriolis force. Adding the gravitational force, we can write the momentum conservation equation as:

$$-\frac{\partial P}{\partial x_i} + \frac{\partial}{\partial x_i}\left[\eta\left(\frac{\partial u_i}{\partial x_k} + \frac{\partial u_k}{\partial x_i} - \frac{2}{3}\frac{\partial u_l}{\partial x_l}\right)\right] + \rho g = 0 \tag{2.45}$$

2.4.3 Energy Conservation

In the energy conservation equation (2.41), the first term on the left side of the equation represents changes in thermal energy over time, such changes can be due to numerous different processes. The second term on the left side of the equation accounts for advective heat transport, i.e., the transport of thermal energy with the movement of the material. Thus, it depends on the velocity at which the material is moving and on the temperature gradient.

The third and fourth terms on the left side of the equation represent adiabatic heating, i.e., they describe how the temperature of the material varies when it is compressed or expanded due to temperature variations, with no exchange of energy with the surrounding medium during the process. Consequently, the work done to compress the material is

released as heat. As the pressure inside the Earth varies mainly due to the increase in lithostatic pressure with depth, we usually neglect the time-dependent term. Thus, the adiabatic heating term of the equation (2.41), can be expressed as:

$$\alpha T u_k \frac{\partial P}{\partial x_k} \tag{2.46}$$

The first term on the right side of the equation is the heat conduction term. The remaining terms in the equation (2.41) describe other thermodynamic processes that may be significant for mantle convection.

The second term on the right side of the equation (2.41) describes viscous dissipation or frictional heating. This term describes the energy released as heat when the material is deformed. The greater the stress required to deform the material and the greater the deformation, the greater the heat released by this process.

And finally, the last term of the equation (2.41) represents the internal heat. Generally, this heat is due to the radioactive decay of unstable isotopes inside the Earth. Thus, this process is more significant in regions where the concentration of elements that produce heat is higher, such as the continental crust.

Other processes and heat sources may be present in the mantle, however, their contributions are smaller, and in most cases, they are neglected, to simplify the resolution of the problem.

2.5 Approximations of the Equations

In the 2.4 section some of the simplifications that can be adopted in the mass, momentum, and energy conservation equations when applied to mantle convection were presented, allowing the choice of which physical processes will be included. In geodynamics, some other approximations are commonly used (Schubert et al., 2001; Gassmöller et al., 2020).

2.5.1 Anelastic Liquid Approximation

The anelastic liquid approximation (Jarvis and Mckenzie, 1980) is based on two premises. The first assumes that lateral variations in density are small compared to the reference density profile (deep-dependent), and the second is that these variations in the depth-dependent density profile can be disregarded in the equations of conservation of

mass (2.22) and energy (2.41). Only the buoyancy term in the momentum equation (2.32) will use a temperature and pressure-dependent density, and this density is approximated by a Taylor series expansion.

This approximation is commonly used in whole-mantle convection models, where there are large variations in surface density up to the boundary between the lower mantle and the outer core, with fluid compressibility being an important effect to consider.

2.5.2 Truncated Anelastic Liquid Approximation

The truncated anelastic liquid approximation (Jarvis and Mckenzie, 1980) has the same premises as the anelastic liquid approximation, but it assumes that changes in density due to pressure effects are orders of magnitude smaller than those due to temperature. In this way, the pressure term in the buoyant forces is neglected in the moment equation.

This consideration implies an imbalance between the energy dissipation calculated by the Stokes equation and the heat dissipation in the energy equation, therefore, this approximation should not be used when the energy dissipation is an important factor for the model (Leng and Zhong, 2008; Alboussière and Ricard, 2013).

2.5.3 Boussinesq approximation

The Boussinesq approximation (Rayleigh, 1916) is a simplification of the anelastic liquid approximation, where the reference temperature and density are assumed to be constants. That is, changes in density are considered to be so small that it is ignored in all terms except the terms where it is multiplied by gravity (in the momentum equation 2.32). This simplification causes the mass conservation equation to assume its incompressible form. Furthermore, this approximation disregards adiabatic and viscous dissipation heating in the energy equation (2.41).

This is a good approximation in cases where the density variations are small, and the modeled processes do not cause significant amounts of adiabatic heating or viscous dissipation. The Boussinesq approximation is widely used in lithospheric scale models.

2.5.4 Extended Boussinesq Approximation

The extended Boussinesq approximation (Christensen and Yuen, 1985) uses the same premises as the Boussinesq approximation without neglecting adiabatic heating and vis-

cous dissipation. However, this approximation should only be used in models with small adiabatic temperature changes because even considering adiabatic heating, the associated volume and density variations are not considered, which leads to the generation of artificial energy in the model.

2.5.5 Dimensionless Equations

The laws of physics cannot vary according to the unit used for physical quantities. That said, it is valuable to express the three conservation equations in terms of dimensionless quantities, i.e., to establish a relationship between dimensional and dimensionless quantities and to verify what happens in the conservation equations when we apply these relationships.

The conservation equations (2.22), (2.32) and (2.41), when applying the approximation of a truncated anelastic liquid can be written as:

$$\frac{\partial \rho u_i}{\partial x_i} = 0 \tag{2.47}$$

$$-\frac{\partial P}{\partial x_i} + \frac{\partial}{\partial x_i}\left[\eta\left(\frac{\partial u_i}{\partial x_k} + \frac{\partial u_k}{\partial x_i} - \frac{2}{3}\frac{\partial u_l}{\partial x_l}\right)\right] + \delta\rho g = 0 \tag{2.48}$$

$$\rho c_P\left(\frac{\partial T}{\partial t} + u_k\frac{\partial T}{\partial x_k}\right) = -\alpha T \rho g u_3 + \rho c_P \frac{\partial}{\partial x_k}\left(k\frac{\partial T}{\partial x_k}\right) + \Phi + \rho H \tag{2.49}$$

We can then write $\delta\rho g$ as:

$$\delta\rho g = -\rho g \alpha (T - T_0) \tag{2.50}$$

Let's define the dimensionless constants to be:

$$x_i = x_i' l_0 \tag{2.51}$$

$$u_i = u_i' \frac{k_0}{l_0} \tag{2.52}$$

$$t = t' \frac{l_0^2}{k_0} \tag{2.53}$$

$$\rho = \rho' \rho_0 \tag{2.54}$$

$$\alpha = \alpha' \alpha_0 \tag{2.55}$$

$$g = g' g_0 \tag{2.56}$$

$$\eta = \eta' \eta_0 \tag{2.57}$$

$$k = k' k_0 \tag{2.58}$$

$$P = P' \frac{\eta_0 k_0}{l_0^2} \tag{2.59}$$

$$c_P = c_P' c_{P0} \tag{2.60}$$

$$T_0 = \Delta T T_0' \tag{2.61}$$

$$T = \Delta T (T' - T_0') \tag{2.62}$$

$$H = \frac{k_0}{l_0^2} c_{P0} \Delta T H' \tag{2.63}$$

where the terms with the lines are the dimensionless terms. Applying the above relations in the conservation equations we obtain:

$$\frac{\partial \rho' u_i'}{\partial x_i'} = 0 \tag{2.64}$$

$$-\frac{\partial P'}{\partial x_i'} + \frac{\partial}{\partial x_i'} \left[\eta' \left(\frac{\partial u_i'}{\partial x_k'} + \frac{\partial u_k'}{\partial x_i'} - \frac{2}{3} \frac{\partial u_l'}{\partial x_l'} \right) \right] + R_a \rho' g' \alpha' T' \delta_{i3} = 0 \tag{2.65}$$

$$\rho' c_P' \left(\frac{\partial T'}{\partial t'} + u_k' \frac{\partial T'}{\partial x_k'} \right) = -D_i (T' + T_0') \alpha' \rho' g' u_3' + \rho' c_P' k' \frac{\partial^2 T}{\partial x_k^2} + \frac{D_i}{R_a} \Phi' + \rho' H' \tag{2.66}$$

And these are the conservation equations for dimensionless quantities, where R_a and D_i are, respectively, the Rayleigh number and the dissipation number given by:

$$R_a = \frac{\rho_0 g_0 \alpha_0 \Delta T l_0^3}{k_0 \eta_0} \tag{2.67}$$

and

$$D_i = \frac{\alpha_0 g_0 l_0}{c_{P0}} \tag{2.68}$$

The Rayleigh number is a quantity that regulates the regime of a fluid. For small values of Ra, the perturbations decrease with time, and there will be no convective movements. For larger Ra, those perturbations will increase exponentially with time, generating convection in the fluid. Thus, it can be said that large values of Ra favor fluid convection. Turcotte and Schubert (2014) show that there is a critical value $Ra_{cr} \approx 600 - 3000$ that characterizes the beginning of convection for a given fluid and that the Ra number for the mantle is of the order of 10^7 which is much greater than the minimum Ra_cr to start thermal convection. It was this calculation that led Arthur Holmes in 1931 to propose that mantle convection was responsible for driving continental drift.

The dissipation number compares the natural range of variations in temperature with the thickness layer l_0 (Ricard, 2015). This number is only used in geophysics and astrophysics problems because it is infinitely small for other laboratory problems. For the Earth's mantle, it is approximately 0.5 (Ricard, 2015).

2.6 Constitutive Equations: Material Properties

In the previous sections, we described the equations that govern fluid dynamics, and how we can incorporate them into the Earth's interior study. However, it is also necessary to consider how materials in the Earth's interior behave under external conditions and forces. The so-called constitutive equations relate the material properties with the variables of the solutions of the conservation equations, such as temperature and pressure.

Which of these relationships and material properties are important to incorporate depends on what you intend to study. For example, as buoyancy is one of the main forces governing the flow of matter on Earth, it is often important to consider how density depends on other variables such as pressure and temperature and to include such dependencies in the equation for the conservation of momentum. Another example would be the studies of the lithosphere and the crust, where the relationships between stress and deformation are

crucial for the evolution of the modeled problem.

2.6.1 Rheology in the Earth's Interior

Rheology is the study of the deformations and flow of matter when exposed to stress. This relationship between stresses and strains is present in the equations of conservation of momentum (2.32) and energy (2.41)

A material when subjected to stress can undergo deformations in different ways. The main types of deformation that occur in rocks inside the Earth will be discussed below.

2.6.2 Elastic Deformation

Elastic deformation is a reversible deformation, when we remove the stresses that caused the deformation, it will return to its previous shape. In elastic deformation, the stress tensor and the strain tensor follow Hooke's Law (Landau et al., 1986).

For homogeneous and isotropic materials, this relationship is expressed as:

$$\sigma_{ij} = 2\mu\epsilon_{ij} + \lambda\delta_{ij}\epsilon_{kk} \tag{2.69}$$

where μ and λ are the first and second parameters of Lamé, respectively, and ϵ is the strain tensor. Lamé parameters describe how much the material deforms elastically when subjected to shear stresses.

2.6.3 Viscous Deformation

Viscous deformations are continuous and irreversible deformations suffered by the material when subjected to stress.

The stress tensor can be written using the viscosity stress tensor equation (2.30) as:

$$\sigma_{ik} = -P\delta_{ij} + \sigma'_{ik} \tag{2.70}$$

where δ_{ij} is the Kronecker delta. Or in terms of the strain rate tensor:

$$\sigma_{ik} = -P\delta_{ij} + 2\eta\dot{\epsilon}'(u) \tag{2.71}$$

where $\dot{\epsilon}$ is the strain rate tensor, and the line indicates the deviatoric portion of the

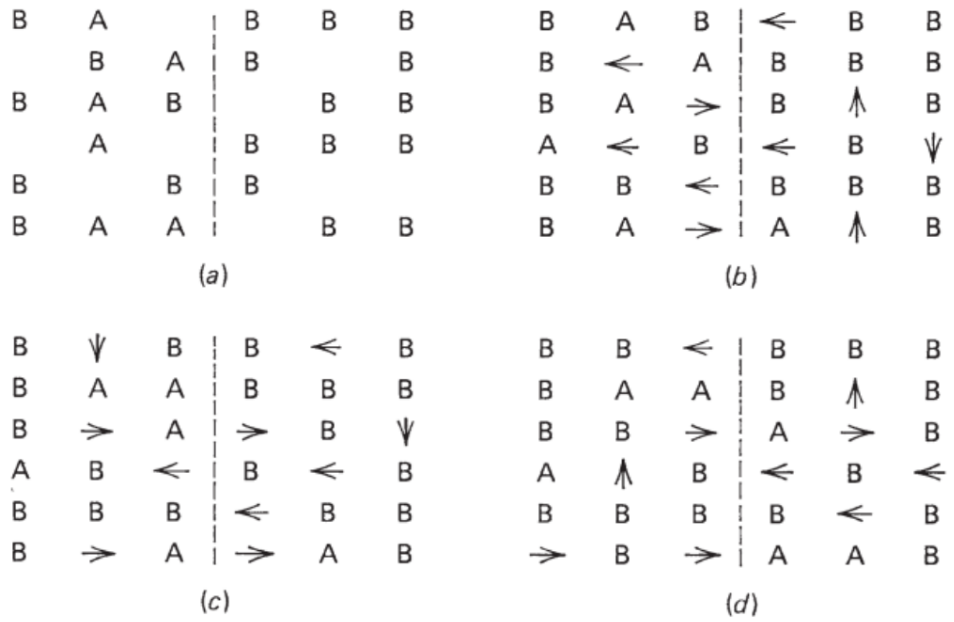

Figure 2.2: A diagram representing the diffusion creep mechanism. The blank spaces are vacancies on the crystalline lattice and the arrows represent the direction an atom moves from a to b, from b to c, and from c to d. Extracted for Turcotte and Schubert (2014)

tensor, i.e., the part where the shape changes refer. The strain rate tensor is directly related to the fluid velocity gradient and can be defined as (Schubert et al., 2001):

$$\dot{\epsilon}'(u) = \frac{1}{2}(\nabla u + \nabla u^T) \tag{2.72}$$

The strain rate tensor describes both volume and shape changes in the material.

In the Earth's interior, this is the dominant process of rock deformation on large time scales, such as mantle convection. Although the terrestrial mantle presents convective movements, this does not mean that the mantle is liquid. The mantle rocks are solid, but those crystalline rocks, when subjected to high pressures and temperatures, cease to present rigidity and begin to viscously deform when subjected to great stress for a long time. This deformation process is called crystalline drag.

In studies of mantle convection, the two main forms of crystalline drag are diffusion creep and dislocation creep.

In diffusion creep, vacancies, i.e., places in the crystal lattice where an atom is missing, migrate through the crystal. These imperfections in the crystal lattice move through the mineral grains generating large deformations over millions of years (Turcotte and Schubert, 2014). This process is the dominant deformation mechanism in the lower mantle.

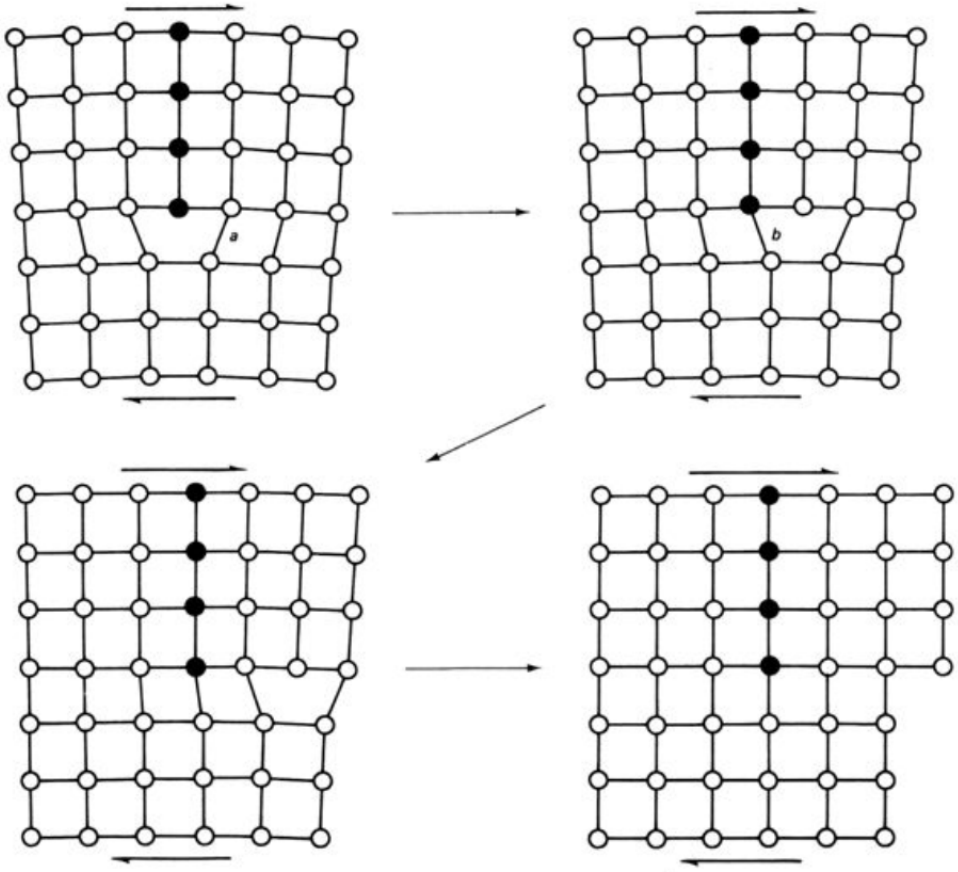

Figure 2.3: A diagram representing the dislocation creep mechanism. We can see the entire line of atoms dislocating through the crystalline lattice when under applied stress. Extracted for Turcotte and Schubert (2014)

In dislocation creep, the defects in the lattice are not just atoms, but an entire line of atoms that will dislocate when subjected to stresses (Turcotte and Schubert, 2014). This mechanism is very sensitive to the stresses applied to the rocks, and as a result, the relationship between stresses and strain rate is no longer linear and starts to be exponential.

Such mechanisms can be incorporated assuming a viscosity η given by the following Arrhenius equation:

$$\eta = A\dot{\epsilon}_{II}^{\frac{1-n}{n}} d^m exp\left(\frac{E^* + PV^*}{RT}\right) \tag{2.73}$$

where E^* and V^* are activation energy and activation volume per mole, p and T are pressure and temperature, R is the gas constant, d is the grain size, m is the grain size exponent, J_2 is the second invariant of the deviatoric strain rate tensor, n is the exponent of the deviatoric strain rate tensor, and the coefficient A is a coefficient which varies depending on the amount of water, molten material and mineralogy. The second invariant

$\dot{\epsilon}_{II}$ of the deviatoric tensor can be written as

$$\dot{\epsilon}_{II} = \left(\frac{\dot{\epsilon}'_{ij}\dot{\epsilon}'_{ij}}{2} \right)^{\frac{1}{2}} \tag{2.74}$$

and $\dot{\epsilon}'_{ij}$ are the components of the deviatoric strain rate tensor $\dot{\boldsymbol{\epsilon}}$.

Considering a viscosity dependent only on temperature and depth and also assuming that there is no significant variation in the size of the grains, i.e., d is constant and that there is no dislocation creep ($n = 0$), resulting in a Newtonian fluid, i.e., the viscosity is independent of the state of mantle tension. Thus, the equation 2.73 reduces to

$$\eta = \eta_0 exp \left(\frac{E^* + PV^*}{RT} \right) \tag{2.75}$$

where η_0 is the reference viscosity.

2.6.4 Brittle Deformation

Brittle deformation, being a type of plasticity, is an irreversible deformation where a rock fracture occurs, such as geological faults. This type of deformation is predominant in the colder portions, under lower lithostatic pressures of the Earth, and essentially in the shallower portions of the lithosphere (crust and upper part of the mantle).

In this deformation, the crystal lattice breaks, and a fault occurs in the rock, which can be on the microscopic scale or extend up to kilometers. By Byerlee's Law (Byerlee, 1968, 1978), brittle deformation occurs when the stress reaches the limit given by:

$$\sigma_{yield} = c_0 + \mu p \tag{2.76}$$

where c_0 is the internal cohesion of the rock, and μ is the coefficient of friction of the rock.

Another way to represent this behavior in rocks is through the Drucker-Prager criterion (Drucker and Prager, 1952), which can be written as:

$$\sigma_{yield} = c_0 \cos\phi + P \sin\phi \tag{2.77}$$

where ϕ is the internal angle of friction.

Considering the relationships between stresses and deformations of materials is not a simple task, in addition, these relationships can be complex, and deformations can still occur as a combination of elastic, viscous, and brittle deformation on Earth.

2.6.5 Transport Equation

In addition to pressure, temperature, and velocity, there may be other important conditions for the evolution of the problem studied, such as the variation in the chemical composition of the material.

When considering thermochemical models, taking into account the compositional variation, it is necessary to include, together with the conservation equations, a transport equation. This equation describes the motion of the compositions considering the advective processes in the Earth's mantle. This equation can be expressed as (Gerya, 2019):

$$\frac{\partial f}{\partial t} + u_i f_{,i} = 0 \tag{2.78}$$

where f is the compositional field. This advection equation assumes that for a given location, changes in composition over time are caused by the transport of material by the stream with velocity v.

Chapter 3

Model Description

In this work, I aim to evaluate the interaction between the asthenospheric mantle flow and a thick cratonic lithosphere, taking into account realistic rheology for the mantle and crust. I used a thermo-mechanical numerical model to simulate the relative movement of cratonic keels over the asthenospheric mantle to evaluate how this motion affects the mantle flow around cratonic regions, modifies the intraplate stress field, and induces vertical displacements in the lithosphere.

The sublithospheric mantle behaves like a fluid on geological timescales (Schubert et al., 2001). The numerical simulation of mantle convection to reproduce the evolution of a cratonic lithosphere interacting with the sublithospheric mantle consists of solving the differential equations related to the conservation of mass, momentum, and energy (Zhong et al., 2007), respectively:

$$u_{i,i} = 0 \tag{3.1}$$

$$\sigma_{ij,j} + g_i \rho = 0 \tag{3.2}$$

$$\frac{\partial T}{\partial t} + u_i T_{,i} = \kappa T_{,ii} + \frac{H}{c_p \rho} + \frac{u_i g_i \alpha T}{c_p} \tag{3.3}$$

where

$$\sigma_{ij} = -P\delta_{ij} + \eta(u_{i,j} + u_{j,i}) \tag{3.4}$$

$$\rho = \rho_0(1 - \alpha(T - T_0)) \tag{3.5}$$

u_i is the i-th component of velocity, η the viscosity, T is the temperature, ρ_0 is the reference density at $T = T_0 = 0°C$, P is the pressure, t time, σ_{ij} is the stress tensor, κ is the thermal diffusivity, g the acceleration of gravity, α the coefficient of thermal expansion, H the radiogenic heat production per unit of mass, c_p the specific heat and δ_{i3} the Kronecker delta (Table 3.1). The repeated indices mean the sum, and the indexes after the comma represent the partial derivative of the respective spatial coordinate.

Table 3.1 - Fixed parameters and their respective values used in numerical simulations. Values taken from Sacek (2017).

Parameter	**Description**	**Value**
α	Coefficient of thermal expansion	3.28×10^{-5} °C^{-1}
κ	Thermal Diffusivity	1.0×10^{-6} m^2/s
T_b	Basal temperature	1500 °C
T_{top}	Top temperature	0 °C
R	Gas constant	8.31 J/mol K
g	Acceleration of gravity	9.8 m/s^2
c_p	Specific heat	1250 J/kgK

In Equation 3.3, the first term on the left side corresponds to the local temperature variation. The second term corresponds to the contribution of advective movements. The first term on the right side of the equation represents thermal diffusivity, and the second term on the right corresponds to radiogenic heat production (internal heat production). The last term in the energy equation is related to the adiabatic heating.

When considering the compositional variation, it is necessary to include, together with the conservation equations, a transport equation. This equation describes the motion of the material compositions considering the advective processes in the Earth's mantle. One can express the transport equation as:

$$\frac{\partial C}{\partial t} + u_i C_{,i} = 0 \tag{3.6}$$

where C is the compositional field presented in Equation 3.7.

I used the computational code Mandyoc (Sacek et al., 2022) in the present work. To numerically solve the mass and momentum conservation equations, this code used the

finite element method (Zhong et al., 2007). The energy conservation equation was solved using the finite element method with the Petrov-Garlekin streamline-upwind formulation proposed by Brooks and Hughes (1982). The code is parallelized using the Portable, Extensible Toolkit for Scientific Computation (PETSc) (Balay et al., 2022).

I used visco-plastic rheology where the effective viscosity η_{eff} is calculated by the combined effect of plastic and viscous rheology. The viscous component (η_{visc}) is given by:

$$\eta_{visc} = C\, A^{\frac{1}{n}}\, \dot{\varepsilon}_{II}^{\frac{1-n}{n}}\, exp\left(\frac{E_a + VP}{nRT}\right) \tag{3.7}$$

where C is a compositional scaling factor of viscosity, n is the power law exponent, A is the pre-exponential scaling factor, $\dot{\varepsilon}_{II} = \left(\dot{\varepsilon}'_{ij}\dot{\varepsilon}'_{ij}/2\right)^{1/2}$ is the square root of the second invariant of the strain rate tensor, R is the universal gas constant, and E_a and V are the activation energy and volume respectively (Table 3.2).

For the plastic regime, the brittle behavior is obtained when the stress reaches the limit given by the Drucker-Prager criterion (Drucker and Prager, 1952).

$$\sigma_{yield} = c_0\, \cos\phi\, +\, P\, \sin\phi \tag{3.8}$$

where c_0 is the internal cohesion of the rock, and ϕ is the angle of internal friction. Plastic strain softening is also taken into account (Figure 3.1c), with variable ϕ and c_0 as a function of cumulative deformation. The plastic component (η_{plast}) is given by:

$$\eta_{plast} = \frac{\sigma_{yield}}{2\,\dot{\varepsilon}_{II}} \tag{3.9}$$

Thus, the effective viscosity (η_{eff}) is given by a combination of the plastic and viscous (Moresi and Solomatov, 1998) components, as:

$$\eta_{eff} = min(\eta_{plast}, \eta_{visc}) \tag{3.10}$$

The free surface is simulated by the sticky-air approach (Crameri et al., 2012) where a layer of low density and low viscosity is inserted above the upper crust to emulate the air and the topographic response is obtained by mapping the interface between the air layer and upper crust.

The composition and the cumulative strain are tracked through time by particles that

permeate each finite element of the domain. Initially, each element contains 40 particles randomly distributed.

Table 3.2 - Rheological parameters of numerical scenarios according to respective layer.

Description	Symbol	Unit	Air	Upper Crust	Lower Crust	Lithospheric Mantle	Asthenosphere
Creep flow law	–	–	–	Wet quartz[1]	Wet quartz[1]	Dry olivine[2]	Wet olivine[2]
Power law exponent	n	–	1	4	4	3.5	3/1[5]
Scale Factor	C	–	1	1	10	1	1
Reference density	ρ_0	kg/m^3	1	2700	2800	3354	3378
Pre-exponent constant	A	Pa^{-n}/s	1.0×10^{-18}	8.574×10^{-28}	8.574×10^{-28}	2.4168×10^{-15}	1.393×10^{-14}/66250[5]
Activation Energy	E_a	kJ/mol	0	222	222	540	429/240000[5]
Activation Volume	V	m^3/mol	0	0	0	25×10^{-6}	15×10^{-6}/5×10^{-6}[5]
Heat Production[3]	H	W/kg	0	9.26×10^{-10}	2.86×10^{-10}	9.0×10^{-12}	0
Cohesion[4]	c_0	MPa	–	20→4	20→4	20→4	20→4
Internal friction angle[4]	$\phi_{eff}(\varepsilon)$	–	–	15°→2°	15°→2°	15°→2°	15°→2°
Strain softening interval[4]	–	–	–	1.05→0.05	1.05→0.05	1.05→0.05	1.05→0.05

[1]: Extracted Gleason e Tullis (1995). [2]: Extracted from Karato e Wu (1993). [3]: Extracted from Andrés-Martínez et al. (2019) for upper and lower crust. [4]: Extracted from Salazar-Mora et al. (2018).

3.1 Model setup

For this work, I used two-dimensional models with an extension of 3 000 km in the horizontal direction and 700 km in the vertical direction with 2 km of grid resolution in both directions, resulting in 525 000 elements.

The domain is subdivided into five layers: air, upper crust, lower crust, lithospheric mantle, and asthenospheric mantle. The thickness of each layer is, respectively, 40, 15, 20, 65 and 560 km resulting in a lithosphere with 100 km thick. Figures 3.1 and 3.2 show the numerical setup. The white layer is the "sticky air" layer, the dark brown layer represents the upper crust, the light brown layer represents the lower crust, the dark green represents the lithosphere mantle and the light green represents the asthenospheric mantle. Table 3.2 shows the values of the parameters for each layer. The values of E_a, V, n and A were taken from Karato and Wu (1993) and Gleason and Tullis (1995). The choice of these values was to reproduce the rheologies of quartz and hydrated and dehydrated olivine in our models.

I explored six different groups of scenarios: the first I added a thicker cratonic keel in the central portion of the model of 100 km thick (Figure 3.1a), the second with a cratonic keel 200 km thick, and the third with no cratonic keel. The other three groups follow the same pattern of cratonic thickness as the first three groups, however, I assumed a linear thinning of the lithosphere on the right border of the model to simulate a free lithospheric

border (Figure 3.2a). Therefore, the lithosphere is only mechanically connected with the left side of the domain.

The initial thermal structure of the lithosphere is only depth-dependent and is represented by the black vertical profile in Figures 3.1a and 3.2a. We considered a model with a temperature of T_0 at the top and T_b at the bottom (see Table 3.1). The temperature is obtained by the solution of the steady-state diffusion equation:

$$\kappa \frac{\partial T(z)}{\partial z^2} + \frac{H(z)}{c_p} = 0 \tag{3.11}$$

where $H(z)$ is the internal heat production of each layer (Table 3.2), assuming that the surface is at 0°C (T_0) and the base of the lithosphere is at 1300°C. Only under the cratonic keel, we assumed an initial linear variation of temperature with depth (T_l) as:

$$T_l(z) = \frac{T_{la} z}{L} \tag{3.12}$$

where $T_{la} = 1300$°C is the temperature at the lithosphere-asthenosphere boundary (LAB), and L is the cratonic thickness.

The asthenospheric temperature increases adiabatically up to the bottom of the domain (T_a). This expression is obtained by integrating the adiabatic temperature gradient (Mckenzie and Bickle, 1988) and can be expressed as:

$$T_a(z) = T_p e^{-g\alpha z/c_p} \tag{3.13}$$

where g is gravity, α the coefficient of thermal expansion, z the depth, c_p the specific heat of the mantle, and $T_p = 1262$°C is the potential temperature for the mantle, which represents the temperature the mantle would be at if it were decompressed and brought to the surface ($z = 0$). The temperature was fixed in all boundaries during the numerical simulations, and the nodes in the air layer were maintained at $T_0 = 0$°C.

The velocity boundary conditions are represented by the horizontal black lines at the left and right borders of the domain indicated in Figures 3.1a and 3.2a and were chosen to ensure the conservation of mass following a similar procedure adopted by Silva and Sacek (2022). In this case, new asthenospheric material enters the numerical domain on the left side, compensating material removal at the right border by the movement of

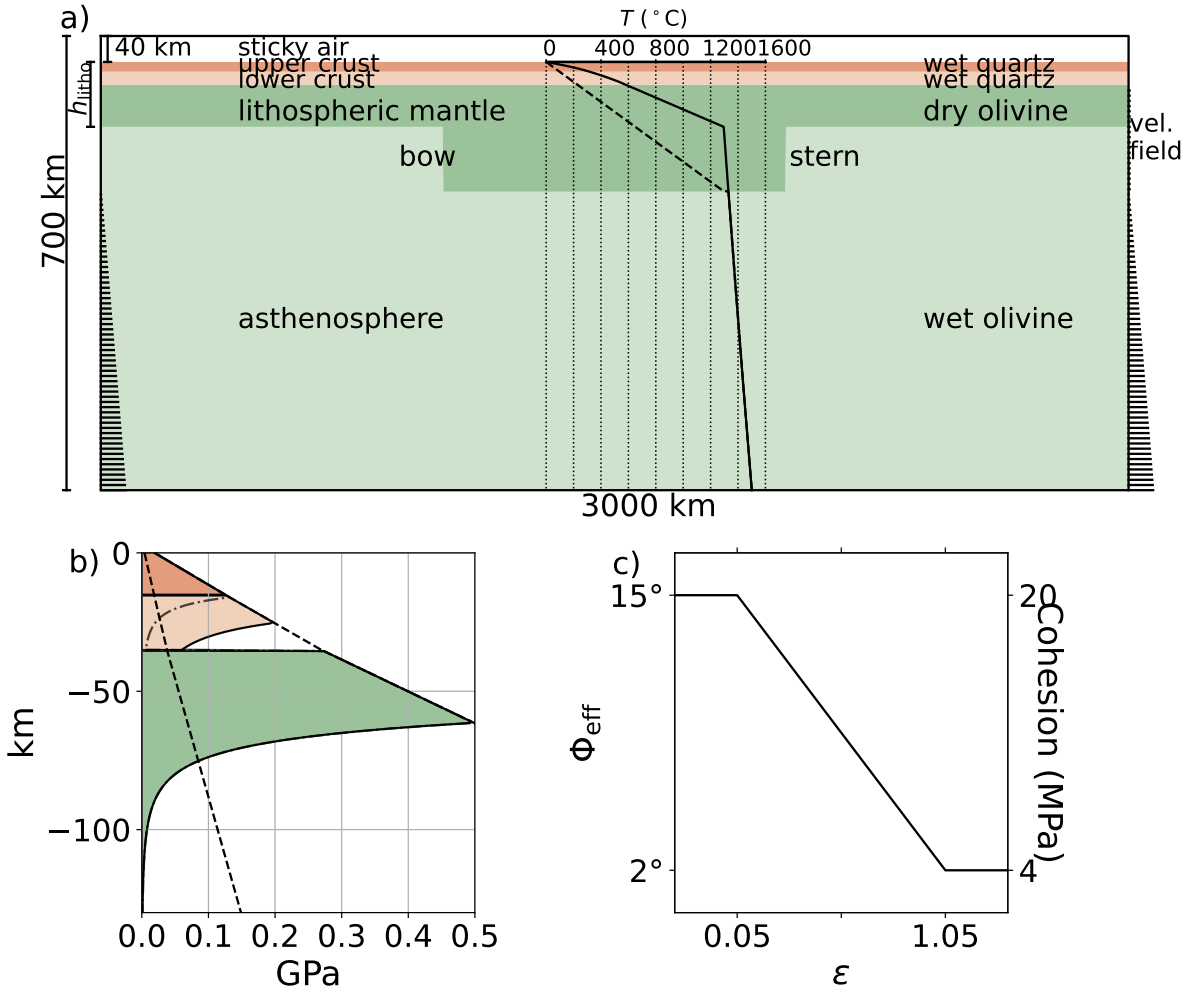

Figure 3.1: a) Numerical setup for the scenarios of Groups I, II, and III. The white layer is the "sticky air" layer, the dark brown layer represents the upper crust, the light brown layer represents the lower crust, the dark green represents the lithosphere mantle and the light green represents the asthenospheric mantle. b) Initial yield strength envelope (YSE) for numerical scenarios, the dash dot line in the lower crust represents the decoupled lithosphere ($C_{lc} = 1$), and the solid line represents the coupled lithosphere ($C_{lc} = 10$). c) Strain softening.

the lithosphere relative to the asthenospheric mantle. This velocity boundary condition represents a reference frame fixed on the lithospheric plate, observing the asthenospheric mantle flowing rightward. This is equivalent to a reference frame fixed on the bottom of the upper mantle observing the lithosphere moving to the left. In an analogy with a boat, we defined the "cratonic bow" as the portion of the keel facing the counterflow of the asthenosphere while the "cratonic stern" is the opposite side of the keel (Figures 3.1 and 3.2). We tested different relative velocities (v_r) between the lithosphere and the bottom of the upper mantle: 0, 1, 2, 4, and 8 cm/yr.

The normal and tangential components of the velocity were fixed on both lateral boundaries. In contrast, at the upper and lower boundaries, the normal velocity component

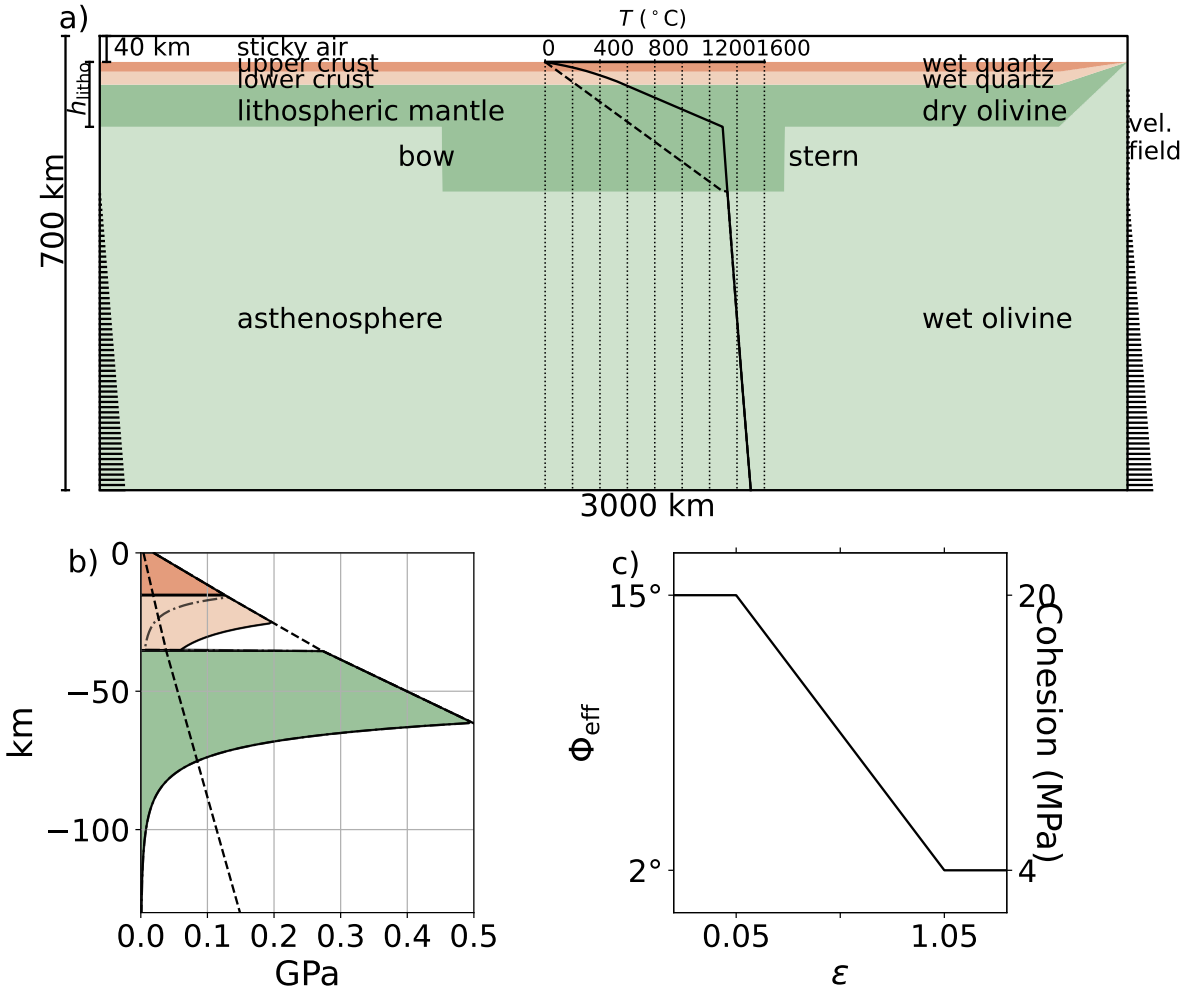

Figure 3.2: a) Numerical setup for the scenarios of Groups IV, V, and VI. The white layer is the "sticky air" layer, the dark brown layer represents the upper crust, the light brown layer represents the lower crust, the dark green represents the lithosphere mantle and the light green represents the asthenospheric mantle. b) Initial yield strength envelope (YSE) for numerical scenarios, the dash dot line in the lower crust represents the decoupled lithosphere ($C_{lc} = 1$), and the solid line represents the coupled lithosphere ($C_{lc} = 10$). c) Strain softening.

was fixed and the tangential component was free.

3.2 Classification of the numerical scenarios

The numerical scenarios are divided into six main groups according to the cratonic keel thickness and lithosphere geometry: Groups I, II, and III using the lithosphere geometry shown in Figure 3.1 (lithosphere connected with both sides of the domain) with a cratonic thickness of 100, 200, and 0, respectively. Groups IV, V, and VI using the lithospheric geometry shown in Figure 3.2 (lithosphere connected only with the left side of the domain) with a cratonic thickness of 100, 200, and 0, respectively.

These six groups are subdivided into two subgroups of scenarios. One for a "decoupled lithosphere" and the second for a "coupled lithosphere". The difference between them is the scale factor for viscosity for the lower crust C_{lc}: in the decoupled model $C_{lc} = 1$, while for the coupled model $C_{lc} = 10$ (Figures 3.1b and 3.2b), assuming the quartz rheology for the entire crust, meaning that for $C_{lc} = 10$ this layer is 10 times more viscous at the same temperature, pressure and strain rate regime when compared to $C_{lc} = 1$. A portion of the stress can still be vertically transmitted through the different layers depending on the stress and temperature of the entire lithosphere. Nevertheless, for clarity in the text, I have chosen to define the scenario with a stronger coupling as the "coupled lithosphere" and the one with a weaker coupling as the "decoupled lithosphere".

To investigate the effects of relative velocity between the lithosphere and the base of the model, each subgroup contains five scenarios with different velocities, ranging from $v_r = 0{-}8$ cm/year, compatible with the range of absolute velocity of the lithospheric plates, based on the HS3-NUVEL 1A model (Gripp and Gordon, 2002) (see arrows in Figure 1.1), considering that the velocity of the plates is calculated relative to the hotspots.

Chapter 4

Numerical Results

In this section, I show the results of the numerical scenarios using a realistic rheological behavior for the crust and mantle as presented in Chapter 3.

4.1 Effects in the intraplate stress near a cratonic keel

To evaluate the effects on the intraplate stress, I calculated the deviatoric stress (σ_{xx}) in the x direction as:

$$\sigma_{xx} = \eta_{eff}\dot{\epsilon}_{xx} \tag{4.1}$$

where η_{eff} is the effective viscosity, and $\dot{\epsilon}_{xx}$ is the strain rate component given by:

$$\dot{\epsilon}_{xx} = \frac{\partial v_x}{\partial x} \tag{4.2}$$

where v_x is the x component of the velocity. Initially, I present the results of the coupled lithosphere ($C_{lc} = 10$) scenarios. The reference models ($v_r = 0$ cm/yr) for Groups I and II (Figures 4.1a - 4.4a) and IV - V (Figures 4.7a - 4.10a) have similar patterns of stress throughout the model domain with predominantly extensional stresses in the lithosphere adjacent to the cratonic keel and compressional stresses predominantly in the cratonic keel. However, this pattern does not occur in Groups III (Figures 4.5a - 4.6a) and VI (Figures 4.11a - 4.12a) because of the absence of the cratonic keel.

After 40 Myr, the magnitude of the horizontal stresses for Group I was approximately $2 - 3$ MPa (Figures 4.2a), $\sim$ 20 MPa (Figures 4.4a) for Group II, $3 - 4$ MPa (Figures 4.8a) for Group IV, and $8 - 10$ MPa (Figures 4.10a) for Group V. Group III shows a compressional regime in the border, and extensional regime in the center of the numerical

scenario (Figure 4.6a), while Group VI presents a extensional regime for the whole model domain (Figure 4.12a). Both Groups III and VI present magnitudes lower than 2 MPa.

These stresses are predominantly due to an isostatic-flexural adjustment of the lithosphere because, at the initial stage, there are isostatic differences between the cold cratonic keel and its neighboring regions.

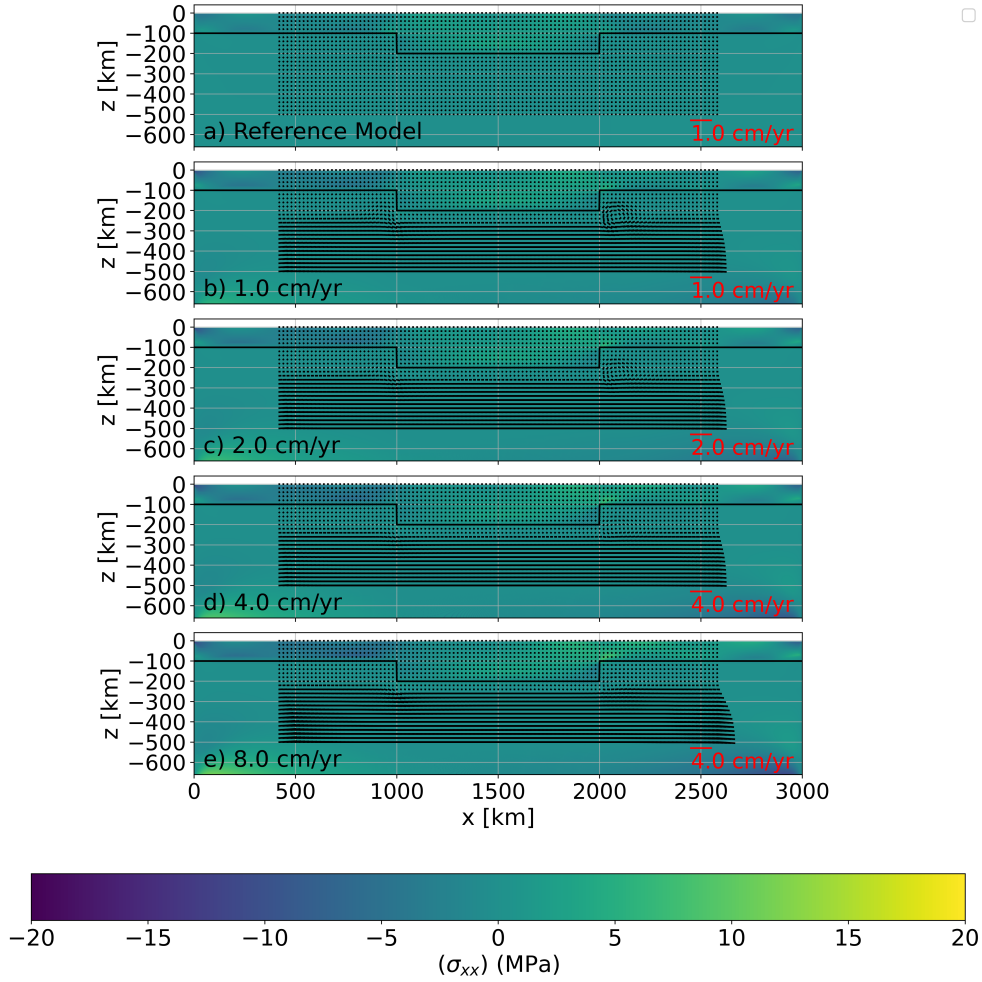

Figure 4.1: Stress field of the numerical scenarios of Group I with a coupled lithosphere ($C_{lc} = 10$), after 40 Myr, with a cratonic keel of 100 km thick, and, with a relative velocity between the lithosphere and the base of the model varying between $v_r = 0 - 8$ cm/year. The black line delimits the lithosphere. Observe that the scale of the velocity vector, indicated in red, varies among the graphs.

When a relative velocity between the lithosphere and the base of the model is imposed (Figures 4.1b-e, 4.3b-e, 4.7b-e, and, 4.9b-e) there is a significant change in the stress pattern in comparison with the reference models (Figures 4.1a, 4.3a, 4.7a, and, 4.9a). Extensional stresses primarily act in the cratonic bow (left portion) of the lithosphere, while compressional stresses are predominant in the cratonic stern (right portion). The crust in the left portion of the craton is in the extensional stress regime, changing to a

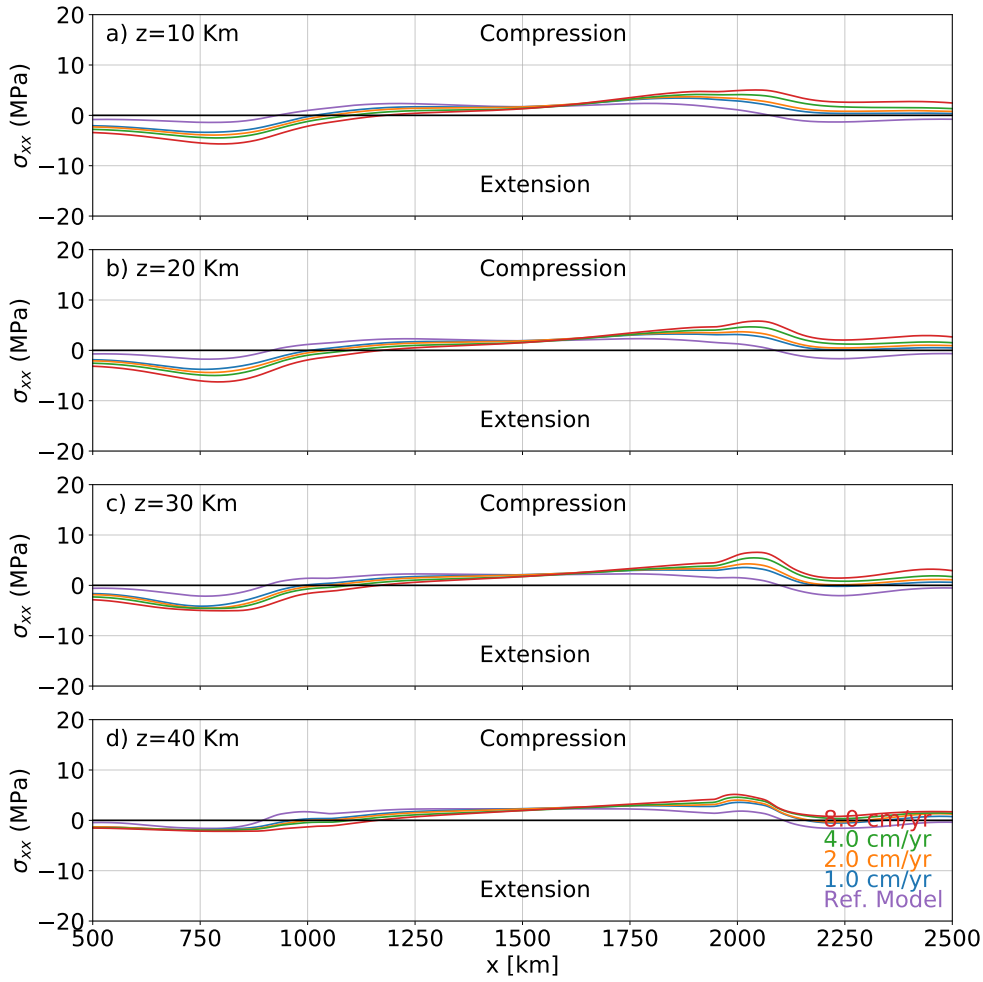

Figure 4.2: Stress profile after 40 Myr of the numerical scenarios of Group I with a coupled lithosphere ($C_{lc} = 10$), with a cratonic keel of 100 km thick, and, with a relative velocity between the lithosphere and the base of the model varying between $v_r = 0 - 8$ cm/year. Profiles were taken in different depths (z). The black line delimits the extensional/compressional regime of stresses.

compressional regime on the right side. The point at which the transition occurs varies slightly with changing velocity, with higher velocities extending the transition point further into the interior of the craton. It also varies with the cratonic thick, reaching approximately 200 km for Groups I and IV (Figures 4.2 and 4.8), 250 km for Group II (Figure 4.4), and 500 km for Group V (Figure 4.10).

Additionally, higher velocities increase the stress magnitude in the lithosphere. For Groups I and IV, with a relative velocity $v_r = 1$ cm/year, the stresses in the crust range from 2 to 3 MPa, and 2 to 8 MPa, respectively, while in the model with $v_r = 8$ cm/year, the stresses were in the range of 3 to 6 MPa and 6 to 12 MPa, respectively (Figures 4.2a-d and 4.8a-d). As for Groups II and V, when considering a thicker cratonic keel (200 km thick), the stresses in the lithosphere exhibited a substantial increase in magnitude. The

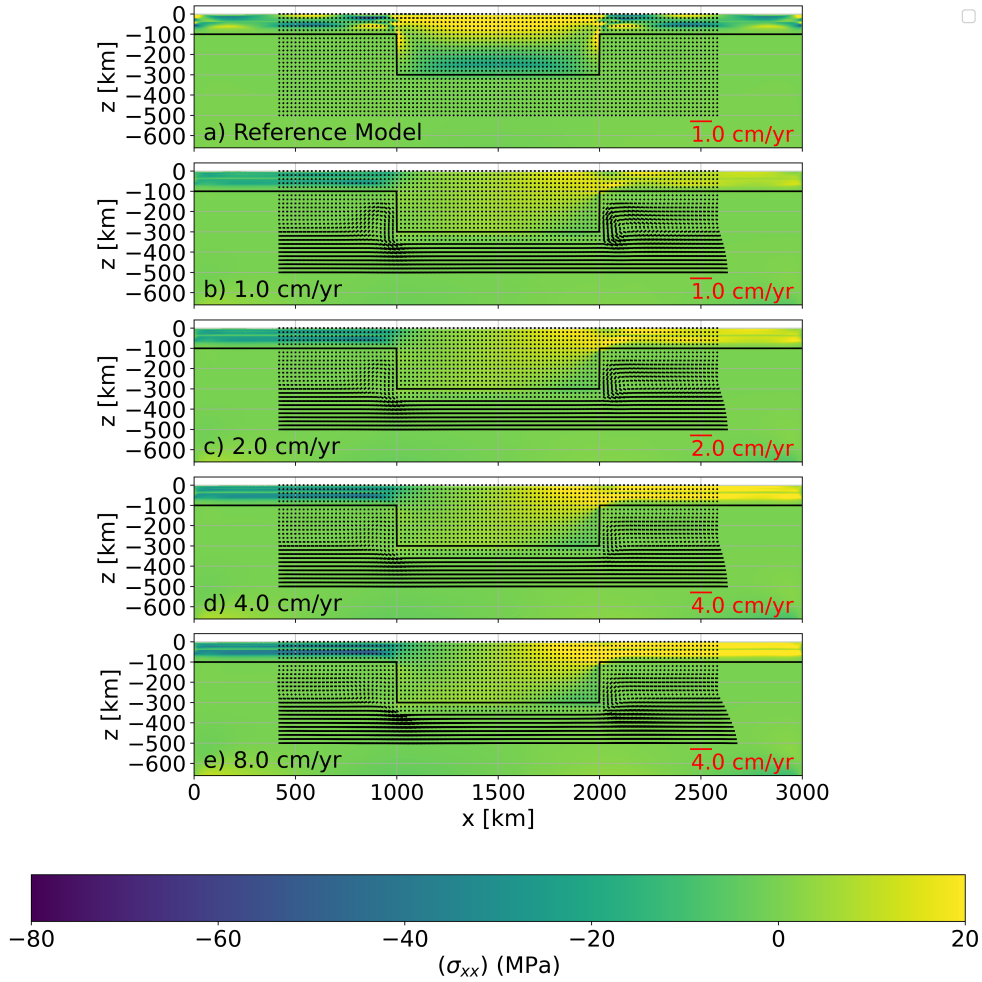

Figure 4.3: Stress field of the numerical scenarios of Group II with a coupled lithosphere ($C_{lc} = 10$), after 40 Myr, with a cratonic keel of 200 km thick, and, with a relative velocity between the lithosphere and the base of the model varying between $v_r = 0 - 8$ cm/year. The black line delimits the lithosphere. Observe that the scale of the velocity vector, indicated in red, varies among the graphs.

maximum stress magnitude of $\sim$ 20 MPa for Group II and $\sim$ 40 MPa for Group V, for the scenario with $v_r = 1$ cm/year and over 50 MPa and 90 MPa, respectively for the scenario with $v_r = 8$ cm/year (Figure 4.10). In the numerical scenarios without a cratonic keel (Figures 4.6 and 4.12) there is a minimal increase in the stresses in the lithosphere (< 1 MPa) when increasing the relative velocity.

I performed new experiments considering a decoupled lithosphere ($C_{lc} = 1$) for the same set of scenarios presented above. For an analogy, the lithosphere is like a "jelly sandwich" (Burov et al., 2006), with a less viscous region separating the crust and the lithospheric mantle. This is seen comparing Figures 4.13 - 4.16. The lithosphere for the models with a decoupled lithosphere presents a less viscous region near $z = 25$ km (Figures 4.15 and 4.16) which does not occur on the coupled scenarios (Figures 4.13 and 4.14). Also, for

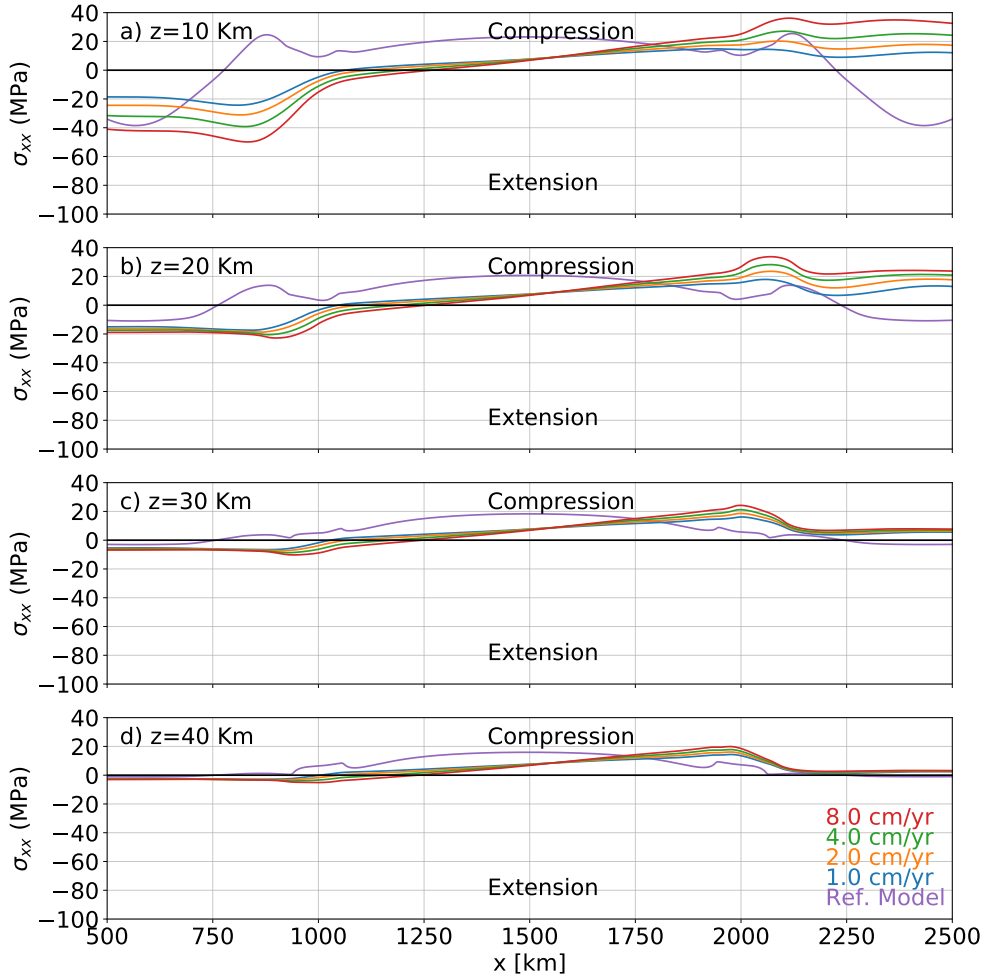

Figure 4.4: Stress profile after 40 Myr of the numerical scenarios of Group II with a coupled lithosphere ($C_{lc} = 10$), with a cratonic keel of 200 km thick, and, with a relative velocity between the lithosphere and the base of the model varying between $v_r = 0 - 8$ cm/year. Profiles were taken in different depths (z). The black line delimits the extensional/compressional regime of stresses.

the reference scenario ($v_r = 0$) cm/yr the asthenosphere is more viscous (Figures 4.13a - 4.16a) than in the scenarios with relative movement between the lithosphere and the base of the model ((Figures 4.13b-e - 4.16b-e)). This difference occurs for two reasons: First, the strain rate tensor is affected by the velocity field, thus affecting the effective viscosity. Second, the heat transfer due to advection is enhanced with a higher velocity field, which in turn keeps the asthenospheric mantle warm for a longer time.

For the decoupled scenario of Groups I (Figures 4.17 and 4.18) and IV (Figures 4.21 and 4.22), there is no significant variation observed in comparison with the coupled model (Figures 4.1, 4.2, 4.7, and 4.8).

Now, for Groups II (Figures 4.19 and 4.20) and V (Figures 4.23 and 4.24) the decoupled scenarios had an increase in the maximum stress magnitude in the lithosphere of approxi-

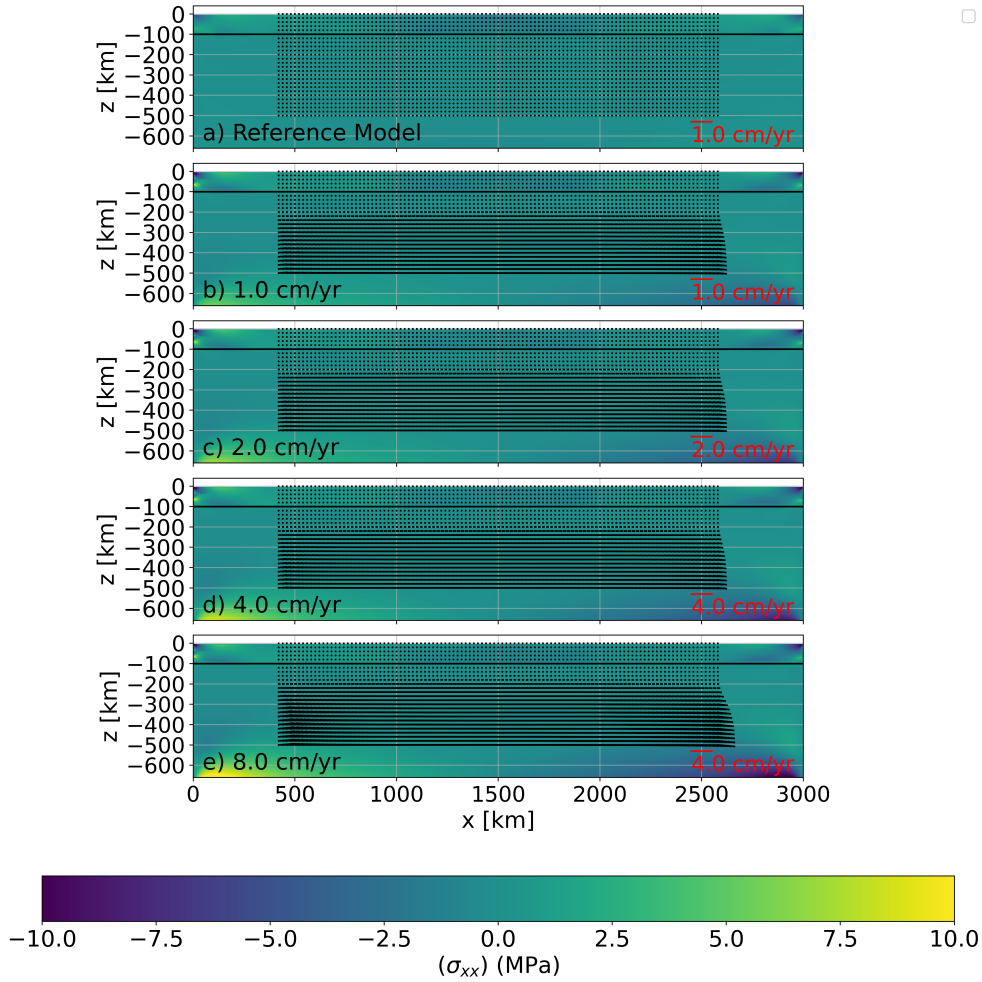

Figure 4.5: Stress field of the numerical scenarios of Group III with a coupled lithosphere ($C_{lc} = 10$), after 40 Myr, with no cratonic keel, and, with a relative velocity between the lithosphere and the base of the model varying between $v_r = 0 - 8$ cm/year. The black line delimits the lithosphere. Observe that the scale of the velocity vector, indicated in red, varies among the graphs.

mately 10 MPa. The decoupled lithosphere implies a less rigid lithospheric plate, so the same basal drag on the cratonic keel, as in the coupled scenario, results in higher stresses in the decoupled scenarios.

One major difference between models of Groups I, II, and III and models of Group IV, V, and VI both for the coupled and the decoupled lithospheres, is the stress pattern in the right border. While Groups I, II, and III have a symmetrical pattern within the right and left border. For Groups IV, V, and VI this is not the case, as the intraplate stresses are dissipated throughout the mechanically free border on the right side. Except for the decoupled model of Group V with $v_r = 8$ cm/yr (Figure 4.24, red line) where the stresses were not dissipated. In this scenario, the cratonic keel and the lithosphere were dragged to the right and the lithosphere reached the right border of the model (Figure

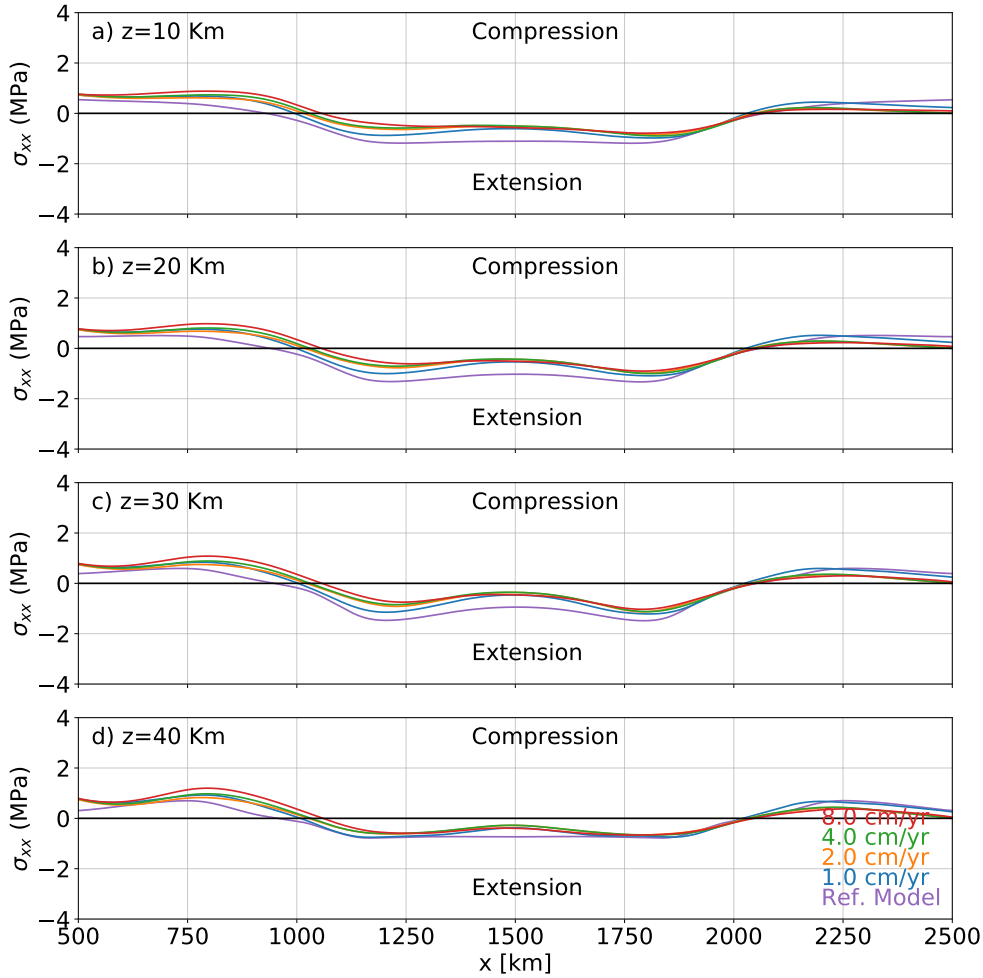

Figure 4.6: Stress profile after 40 Myr of the numerical scenarios of Group III with a coupled lithosphere ($C_{lc} = 10$), with no cratonic keel, and, with a relative velocity between the lithosphere and the base of the model varying between $v_r = 0 - 8$ cm/year. Profiles were taken in different depths (z). The black line delimits the extensional/compressional regime of stresses.

4.16e). Furthermore, the magnitude of the stresses was drastically reduced to the left portion of the cratonic keel, and the viscosity structure at approximately $x = 800$ km resembles the formation of a rift (Figures 4.24 and 4.16e). In the same scenario with a coupled lithosphere (Figure 4.14e) this drag of the cratonic keel and the lithosphere was relatively small compared with the decoupled scenario, which supports the idea of a more rigid and stronger lithosphere on the coupled scenario.

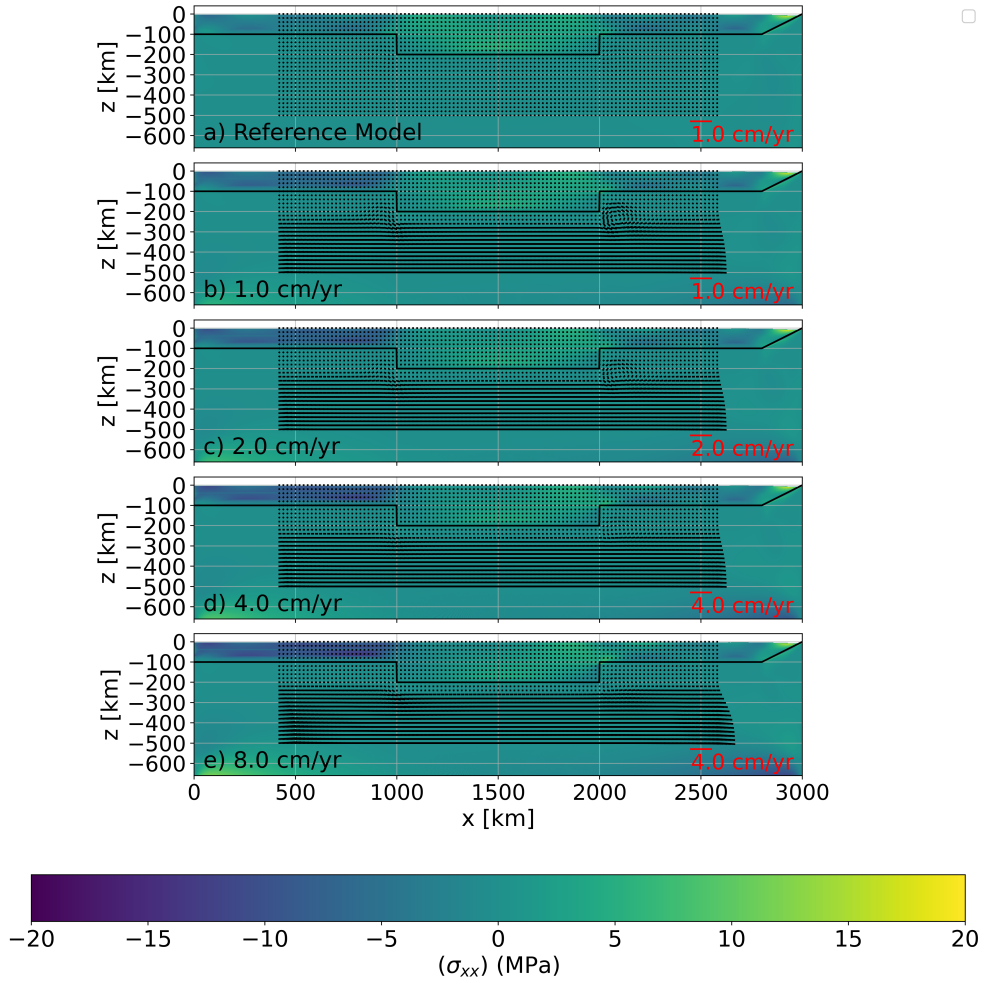

Figure 4.7: Stress field of the numerical scenarios of Group IV with a coupled lithosphere ($C_{lc} = 10$), after 40 Myr, with a cratonic keel of 100 km thick, and, with a relative velocity between the lithosphere and the base of the model varying between $v_r = 0 - 8$ cm/year. The black line delimits the lithosphere. Observe that the scale of the velocity vector, indicated in red, varies among the graphs.

4.2 *Edge-driven convection induced in the asthenosphere by lateral variations in lithospheric thickness*

In the reference scenario (with $v_r = 0$ cm/year) of Group V (200 km cratonic keel), for a coupled and decoupled lithosphere, it is possible to see the edge-driven convection (King and Anderson, 1998) at the borders of the craton (Figures 4.9a and 4.23a). This occurs essentially due to the lateral variation of lithospheric thickness and thermal effects related to the horizontal conduction of heat from the asthenosphere to the cratonic keel, resulting in the cooling of the adjacent asthenospheric mantle and consequent downward flow. Due to the symmetry of the cratonic keel in the model, the convective pattern in the reference scenario is the same on both sides of the keel.

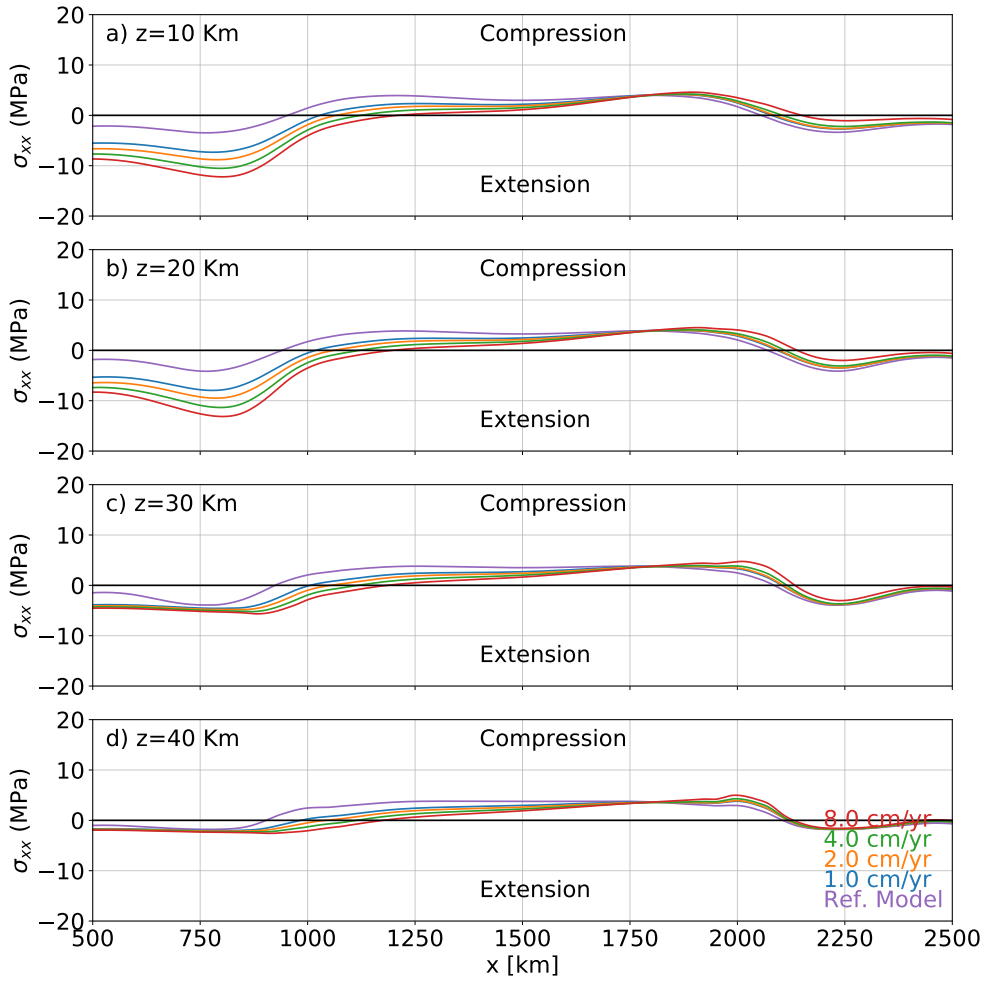

Figure 4.8: Stress profile after 40 Myr of the numerical scenarios of Group IV with a coupled lithosphere ($C_{lc} = 10$), with a cratonic keel of 100 km thick, and, with a relative velocity between the lithosphere and the base of the model varying between $v_r = 0 - 8$ cm/year. Profiles were taken in different depths (z). The black line delimits the extensional/compressional regime of stresses.

However, with the imposed velocity of the lithosphere relative to the base of the model, this symmetry disappears (Figures 4.9b-e and 4.23b-e). The convective cells are affected by the horizontal asthenospheric flow and can be amplified or suppressed depending on the direction of lithospheric movement relative to the base of the upper mantle (King and Anderson, 1998). The vigor of the edge-driven convection is smaller along the cratonic bow (left side) than along the cratonic stern (e.g. Figure 4.9b-d).

Furthermore, this effect is not restricted to these two models and is visible in all models with a cratonic keel. Even in models of Groups I and IV, with a cratonic keel of 100 km (Figures 4.1, 4.7, 4.21,4.7) the edge-driven convection starts to be visible and is affected by the relative motion of the lithosphere and the base of the model.

Due to the choice of the length of the velocity vectors and due to the differences in

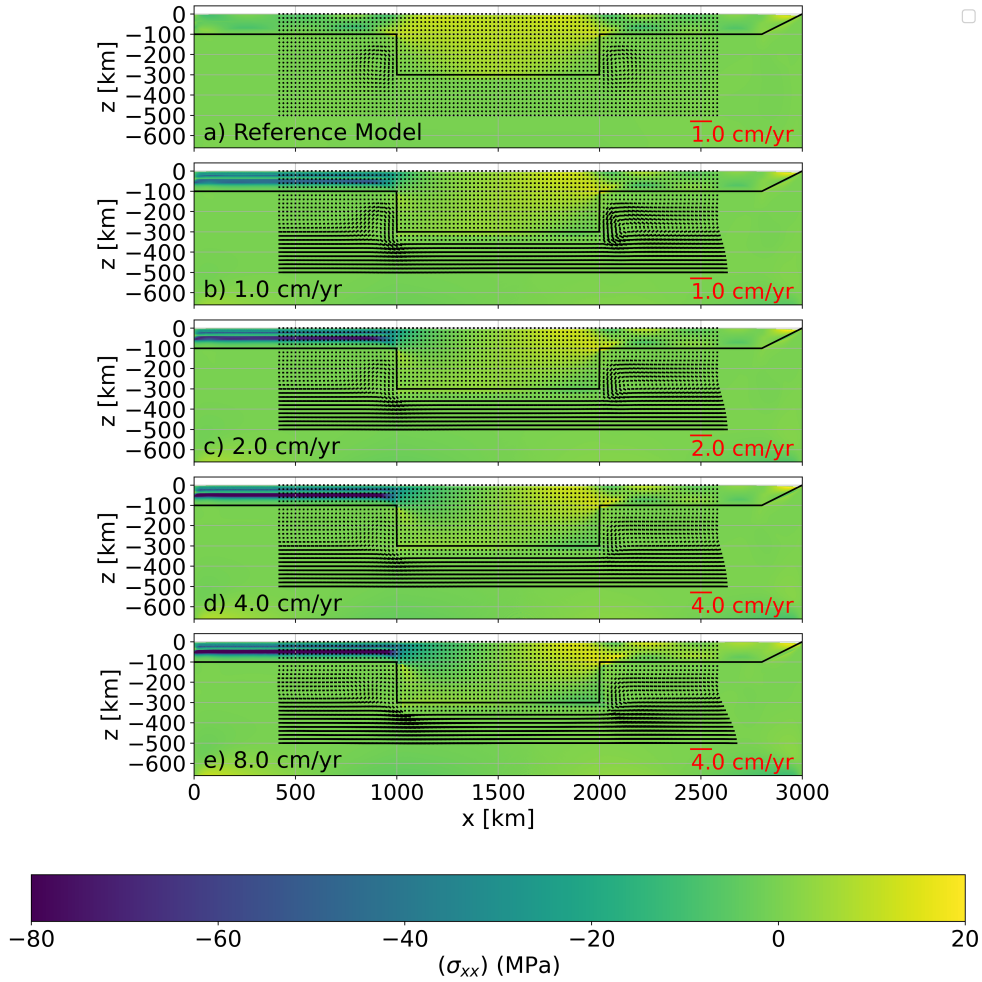

Figure 4.9: Stress field of the numerical scenarios of Group V with a coupled lithosphere ($C_{lc} = 10$), after 40 Myr, with a cratonic keel of 200 km thick, and, with a relative velocity between the lithosphere and the base of the model varying between $v_r = 0 - 8$ cm/year. The black line delimits the lithosphere. Observe that the scale of the velocity vector, indicated in red, varies among the graphs.

velocity scales in Figures 4.7 and 4.9, the edge-driven convection is more visible in scenarios with lower velocities. However, the edge-driven convection is more vigorous in the higher velocity scenarios. Also, a thicker cratonic keel produced an even more vigorous convection cell in the adjacency of the cratonic region (e.g. Figure 4.9e).

4.3 Topographic effects

Ultimately, I calculated the evolution of the dynamic topography for the scenarios of Groups I, II, IV, and V (Figures 4.25 to 4.32) both for the coupled and decoupled lithosphere, showing the results in intervals of 5 Myr.

For the coupled and decoupled scenarios of Groups I and IV, with a cratonic keel of 100 km (Figures 4.25, 4.27,4.29, and 4.31), the differences between the dynamic topography

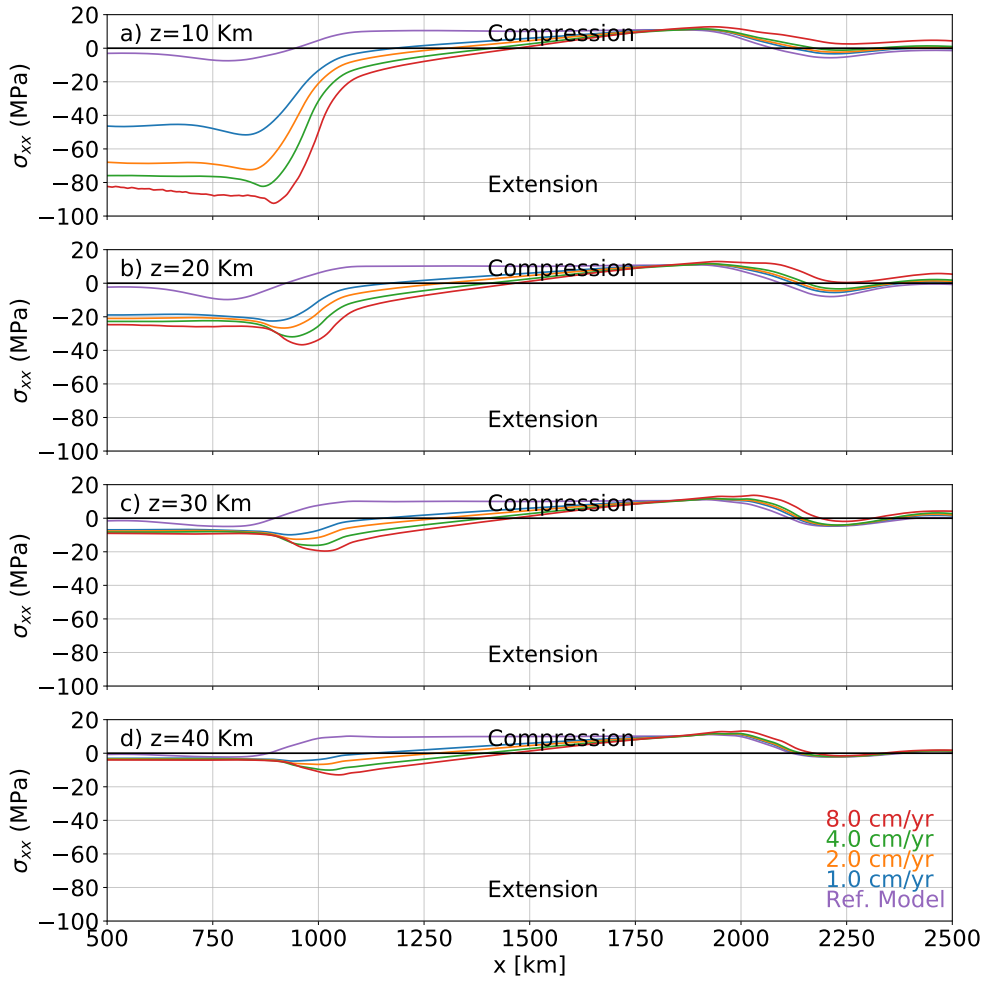

Figure 4.10: Stress profile after 40 Myr of the numerical scenarios of Group V with a coupled lithosphere ($C_{lc} = 10$), with a cratonic keel of 200 km thick, and, with a relative velocity between the lithosphere and the base of the model varying between $v_r = 0 - 8$ cm/year. Profiles were taken in different depths (z). The black line delimits the extensional/compressional regime of stresses.

and the reference model oscillated around zero, without a clear correlation with the position of the cratonic keel. The only notable difference is a subsidence of < 200 m in the center of the cratonic keel ($x = 1500$ km) for the scenarios of Group IV with $v = 8$ cm/yr (Figures 4.27 and 4.31).

On the other hand, in the scenarios of Groups II and V, with a thicker cratonic keel, regional subsidence on the right side of the cratonic region ($x = 2000 - 2300$ km) is observed (Figures 4.26, 4.28, 4.30, and 4.32). This subsidence is enhanced for higher velocities, varying from ~ 200 m for the scenario with $v_r = 1$ cm/yr to > 600 m for the coupled scenario of Group V with $v_r = 8$ cm/yr. For the decoupled model of Group V, this value gets near to ~ 1000 m. However, it is important to remember that this is the model where the cratonic keel was dragged to the right by the basal traction, and this can

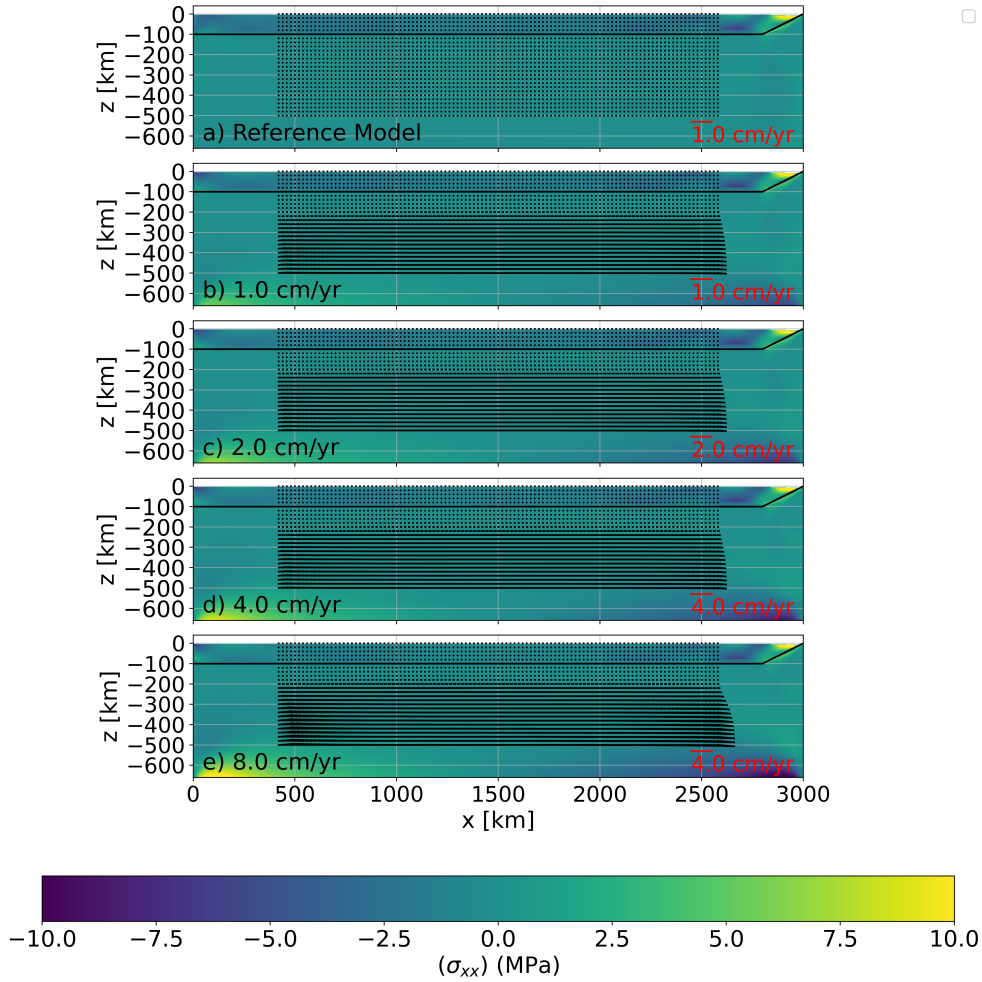

Figure 4.11: Stress field of the numerical scenarios of Group VI with a coupled lithosphere ($C_{lc} = 10$), after 40 Myr, with no cratonic keel, and, with a relative velocity between the lithosphere and the base of the model varying between $v_r = 0 - 8$ cm/year. The black line delimits the lithosphere. Observe that the scale of the velocity vector, indicated in red, varies among the graphs.

be a result of the lithosphere colliding on the right border of the model domain.

Also, in the Group V and coupled scenario with $v_r = 8$ cm/yr (Figure 4.32), there is a small subsidence at $x = 1000$ km of < 200 m. Additionally, a broad positive dynamic topography is also observed on the left portion of the craton ($x < 900$ km), in the coupled and decoupled models of Group II and the coupled model of Group V (Figures 4.26, 4.28, and 4.30). For the decoupled model of Group V (Figure 4.32), there is an abrupt decrease in the dynamic topography at $x = 900$ km when compared to the coupled model.

Except for the scenario with a decoupled lithosphere of Group V (Figure 4.32), it appears that the degree of coupling of the lithosphere does not have an impact on the dynamic topography.

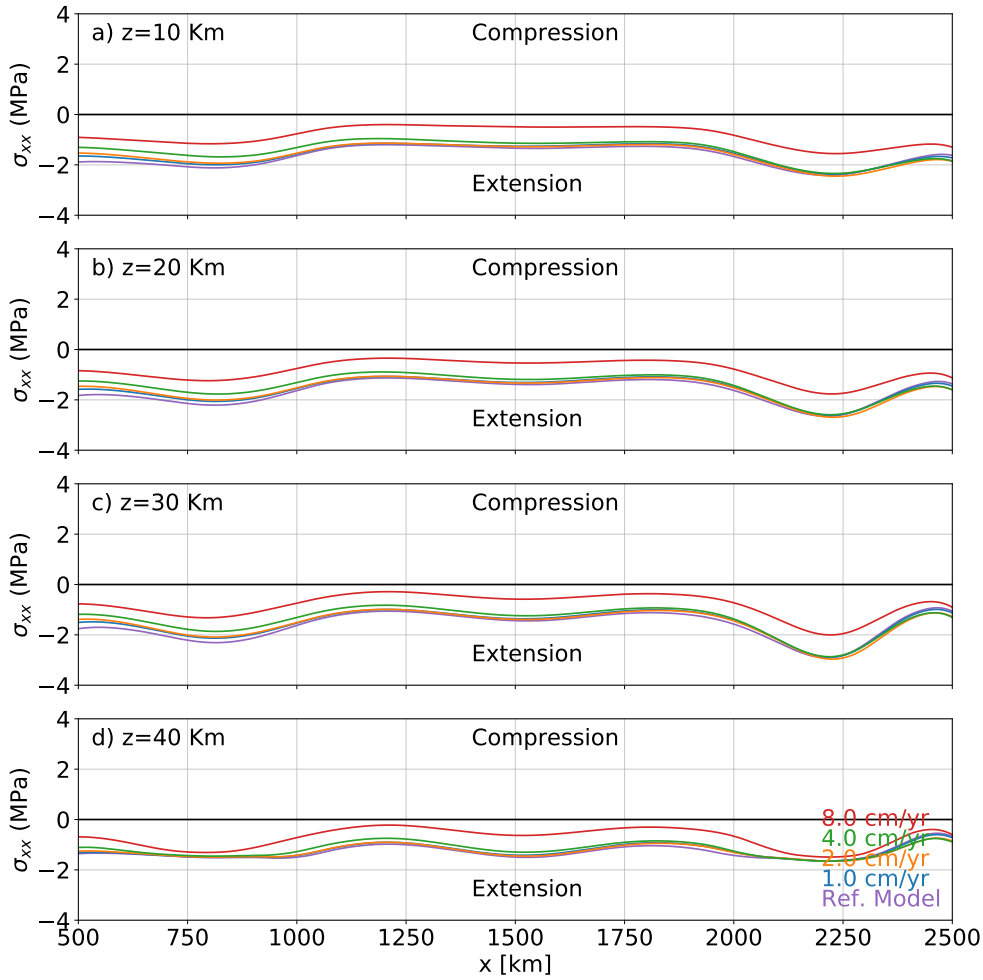

Figure 4.12: Stress profile after 40 Myr of the numerical scenarios of Group VI with a coupled lithosphere ($C_{lc} = 10$), with no cratonic keel, and, with a relative velocity between the lithosphere and the base of the model varying between $v_r = 0 - 8$ cm/year. Profiles were taken in different depths (z). The black line delimits the extensional/compressional regime of stresses.

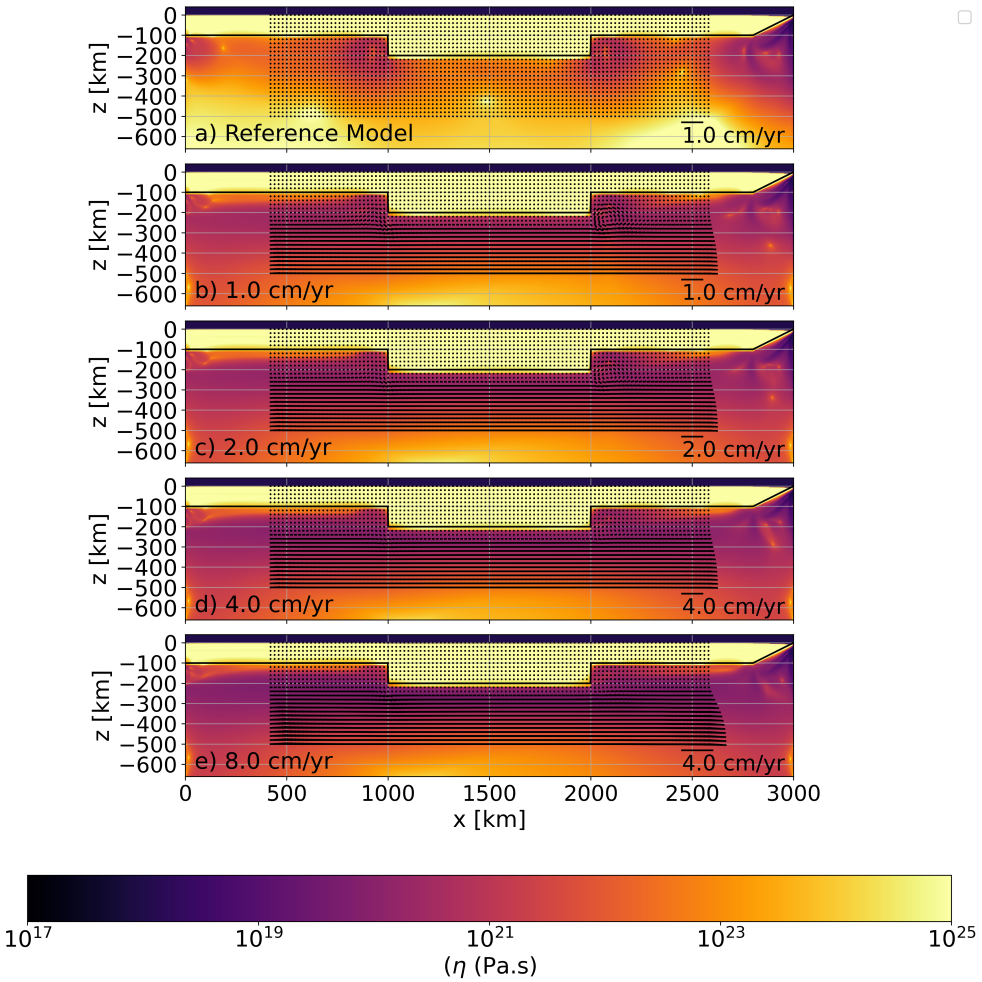

Figure 4.13: Viscosity structure of the numerical scenarios of Group IV with a coupled lithosphere ($C_{lc} = 10$), with a cratonic keel of 100 km thick, and, with a relative velocity between the lithosphere and the base of the model varying between $v_r = 0 - 8$ cm/year. The black line delimits the lithosphere. Observe that the scale of the velocity vector, indicated in black on the right side, varies among the graphs.

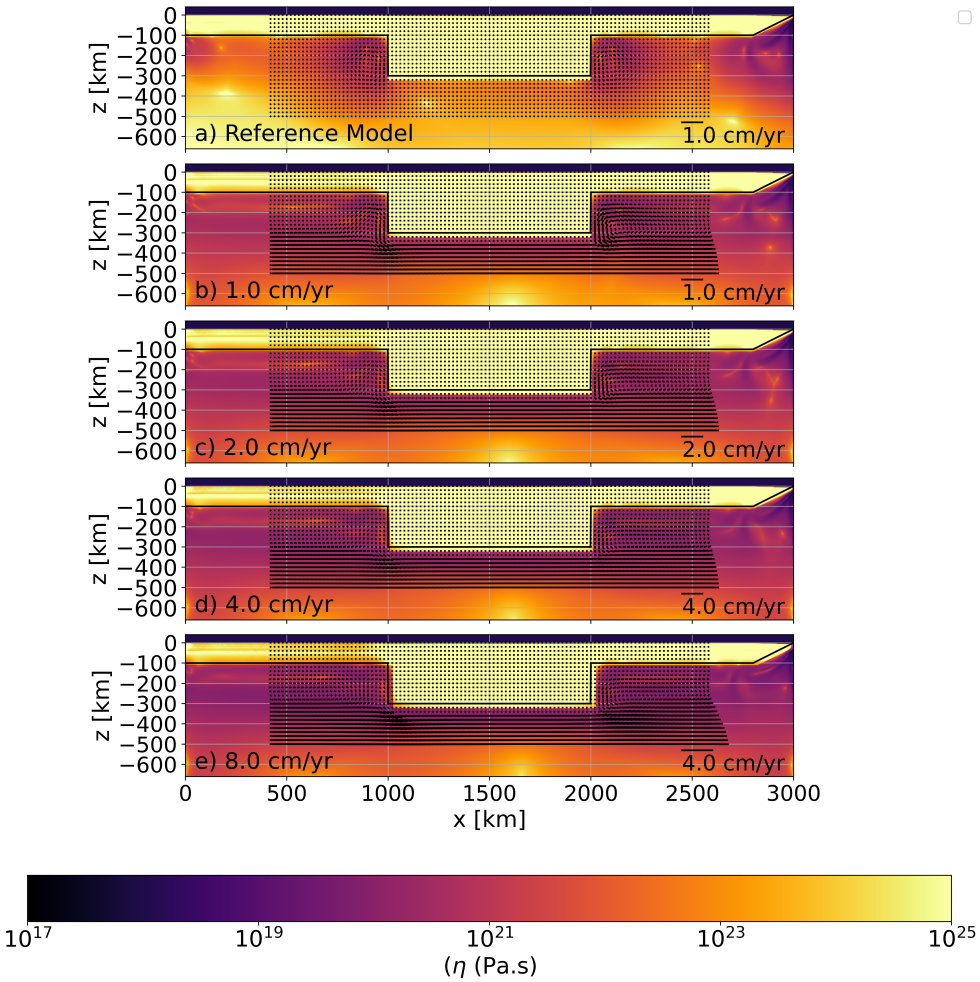

Figure 4.14: Viscosity structure of the numerical scenarios of Group V with a coupled lithosphere ($C_{lc} = 10$), with a cratonic keel of 200 km thick, and, with a relative velocity between the lithosphere and the base of the model varying between $v_r = 0 - 8$ cm/year. The black line delimits the lithosphere. Observe that the scale of the velocity vector, indicated in black on the right side, varies among the graphs.

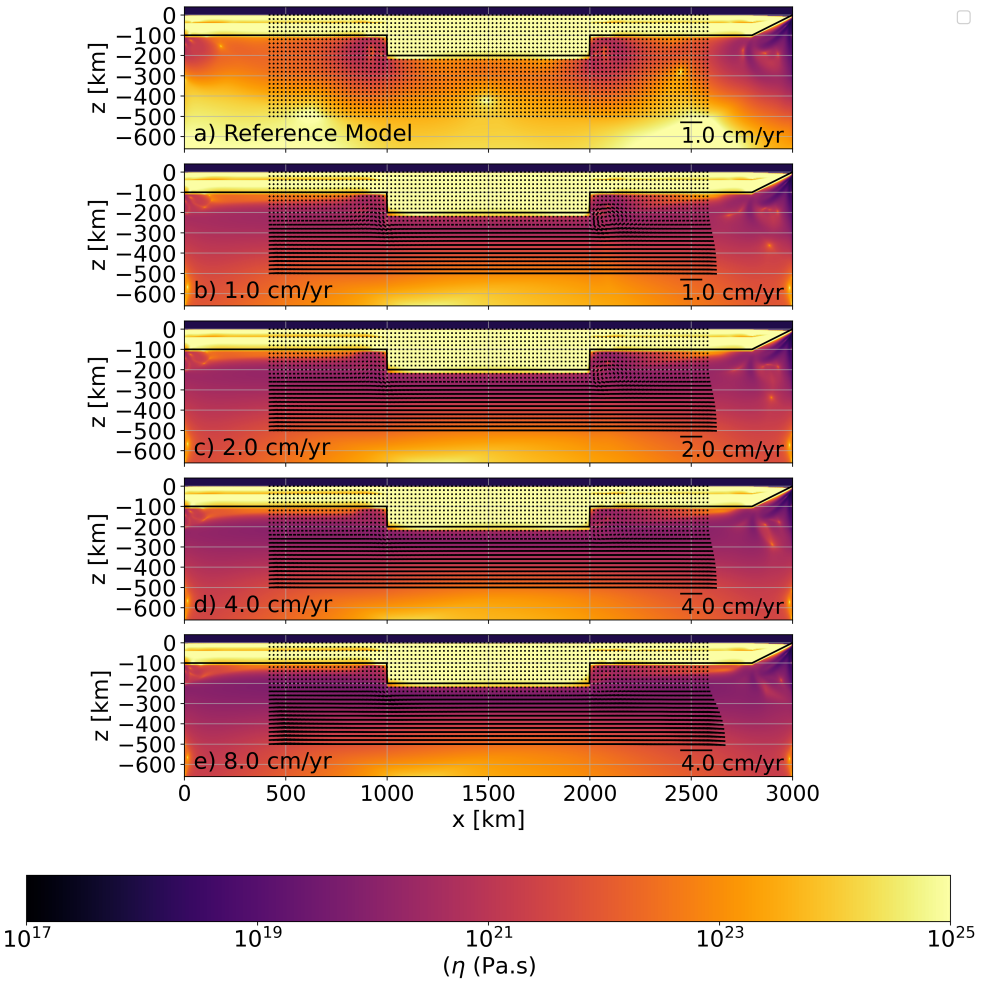

Figure 4.15: Viscosity structure of the numerical scenarios of Group IV with a decoupled lithosphere ($C_{lc} = 1$), with a cratonic keel of 100 km thick, and, with a relative velocity between the lithosphere and the base of the model varying between $v_r = 0 - 8$ cm/year. The black line delimits the lithosphere. Observe that the scale of the velocity vector, indicated in black on the right side, varies among the graphs.

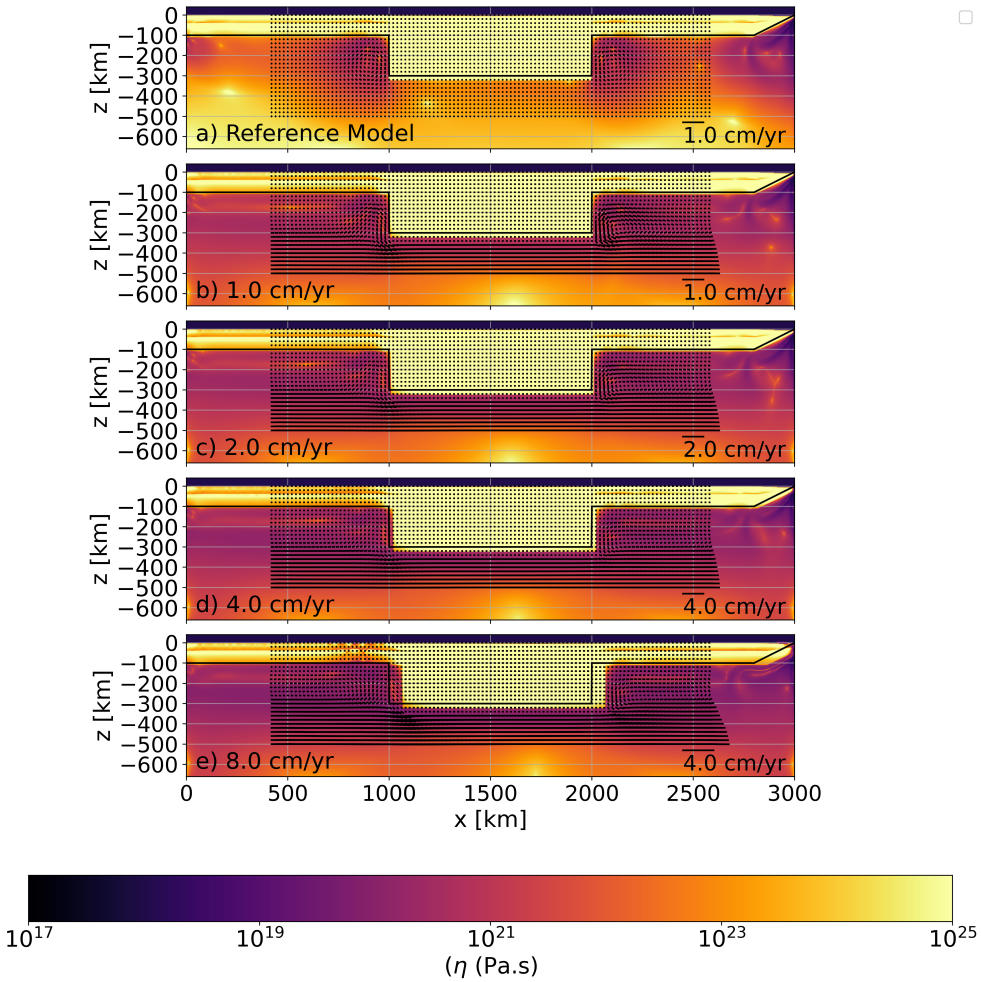

Figure 4.16: Viscosity structure of the numerical scenarios of Group V with a decoupled lithosphere ($C_{lc} = 1$), with a cratonic keel of 200 km thick, and, with a relative velocity between the lithosphere and the base of the model varying between $v_r = 0 - 8$ cm/year. The black line delimits the lithosphere. Observe that the scale of the velocity vector, indicated in black on the right side, varies among the graphs.

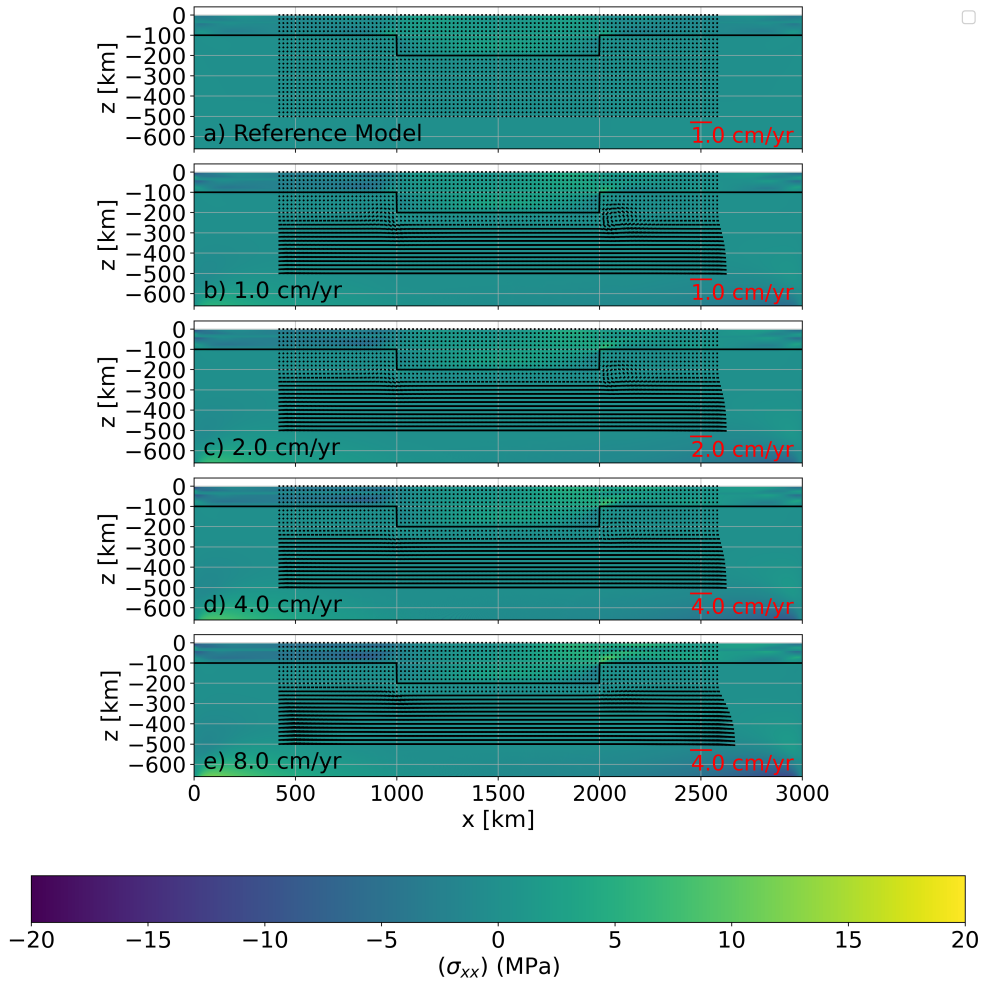

Figure 4.17: Stress field of the numerical scenarios of Group I with a decoupled lithosphere ($C_{lc} = 1$), after 40 Myr, with a cratonic keel of 100 km thick, and, with a relative velocity between the lithosphere and the base of the model varying between $v_r = 0 - 8$ cm/year. The black line delimits the lithosphere. Observe that the scale of the velocity vector, indicated in red, varies among the graphs.

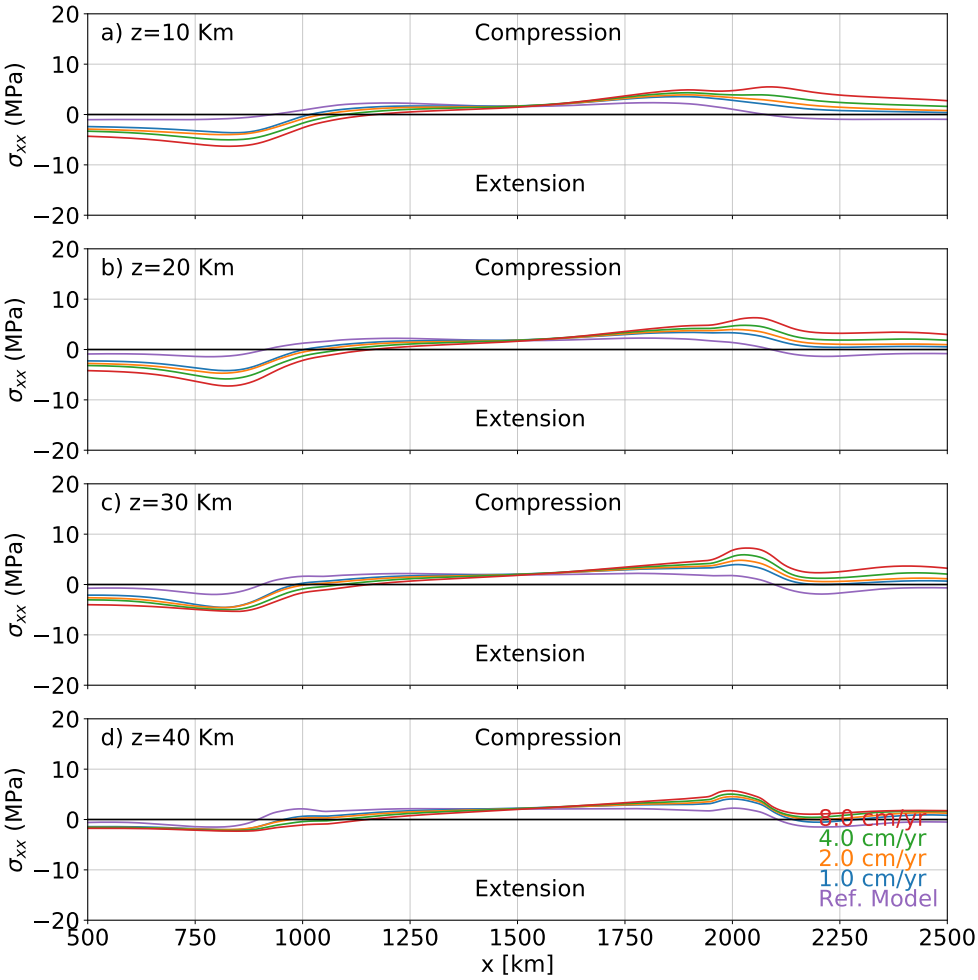

Figure 4.18: Stress profile after 40 Myr of the numerical scenarios of Group I with a decoupled lithosphere ($C_{lc} = 1$), with a cratonic keel of 100 km thick, and, with a relative velocity between the lithosphere and the base of the model varying between $v_r = 0 - 8$ cm/year. Profiles were taken in different depths (z). The black line delimits the extensional/compressional regime of stresses.

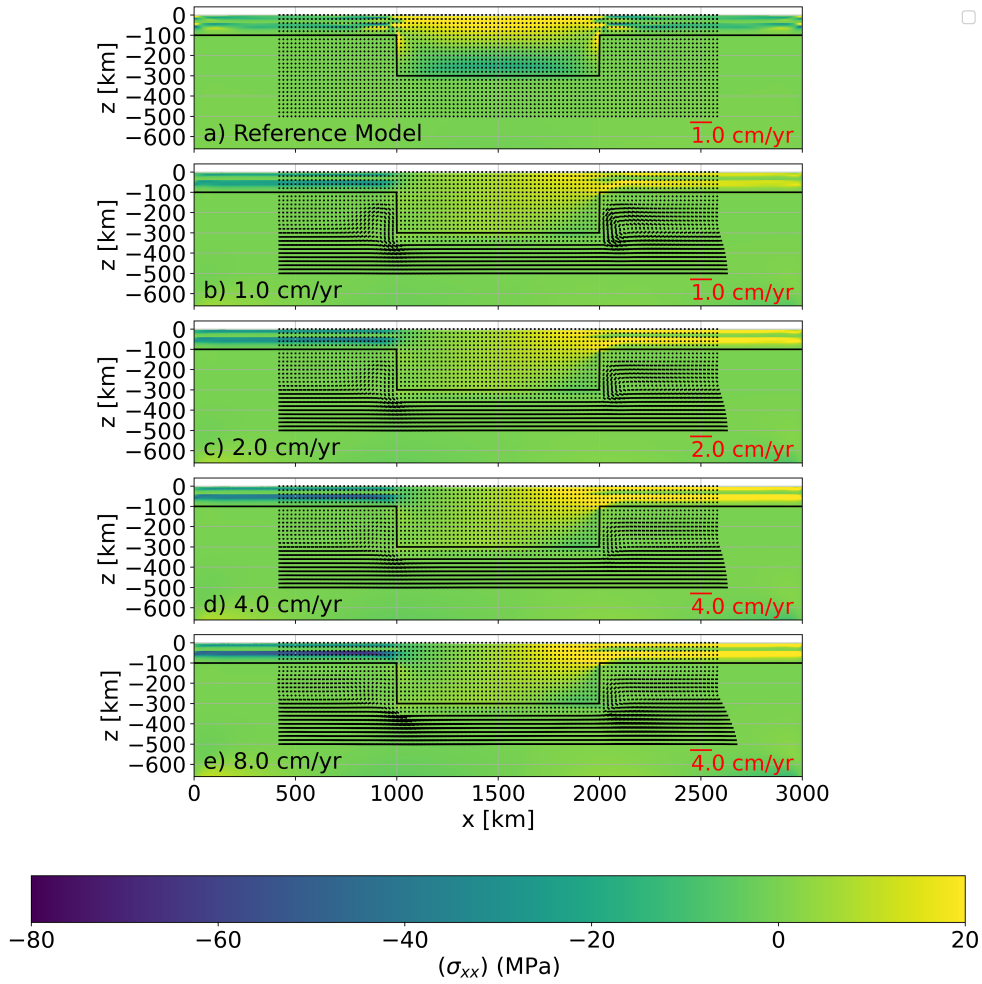

Figure 4.19: Stress field of the numerical scenarios of Group II with a decoupled lithosphere ($C_{lc} = 1$), after 40 Myr, with a cratonic keel of 200 km thick, and, with a relative velocity between the lithosphere and the base of the model varying between $v_r = 0 - 8$ cm/year. The black line delimits the lithosphere. Observe that the scale of the velocity vector, indicated in red, varies among the graphs.

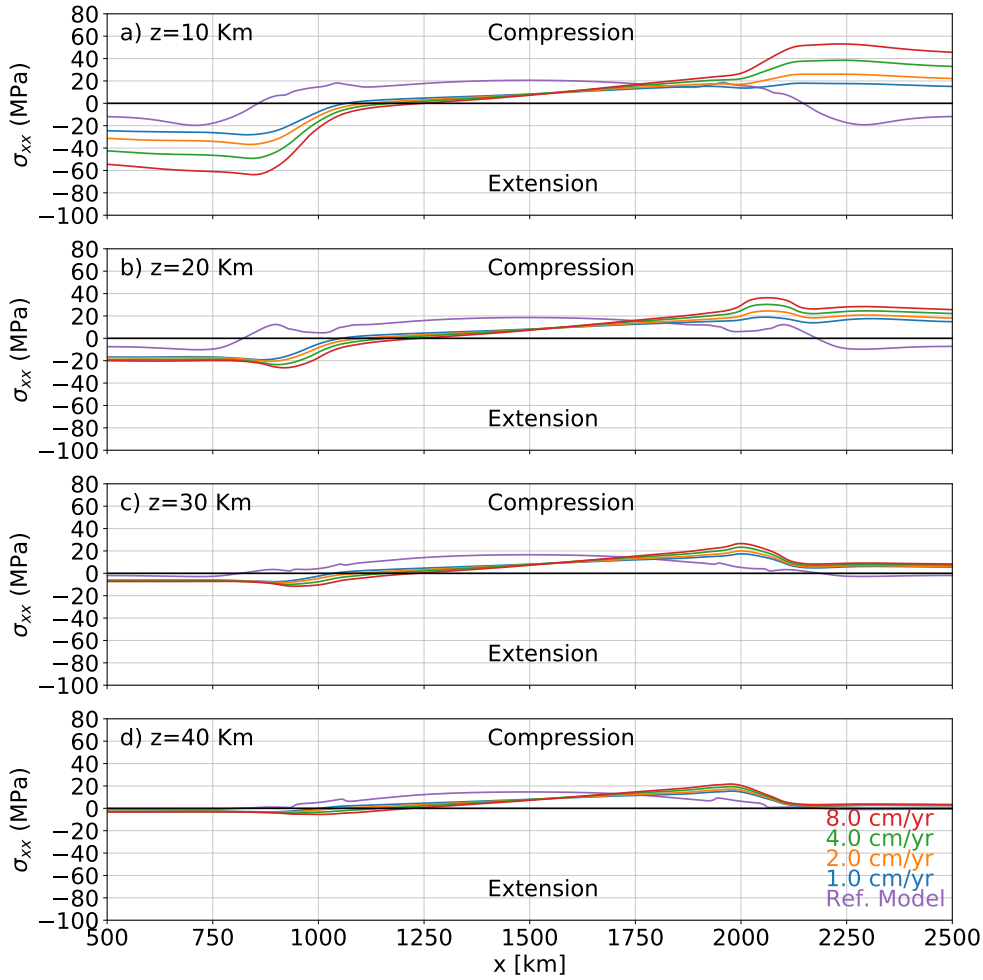

Figure 4.20: Stress profile after 40 Myr of the numerical scenarios of Group II with a decoupled lithosphere ($C_{lc} = 1$), with a cratonic keel of 200 km thick, and, with a relative velocity between the lithosphere and the base of the model varying between $v_r = 0 - 8$ cm/year. Profiles were taken in different depths (z). The black line delimits the extensional/compressional regime of stresses.

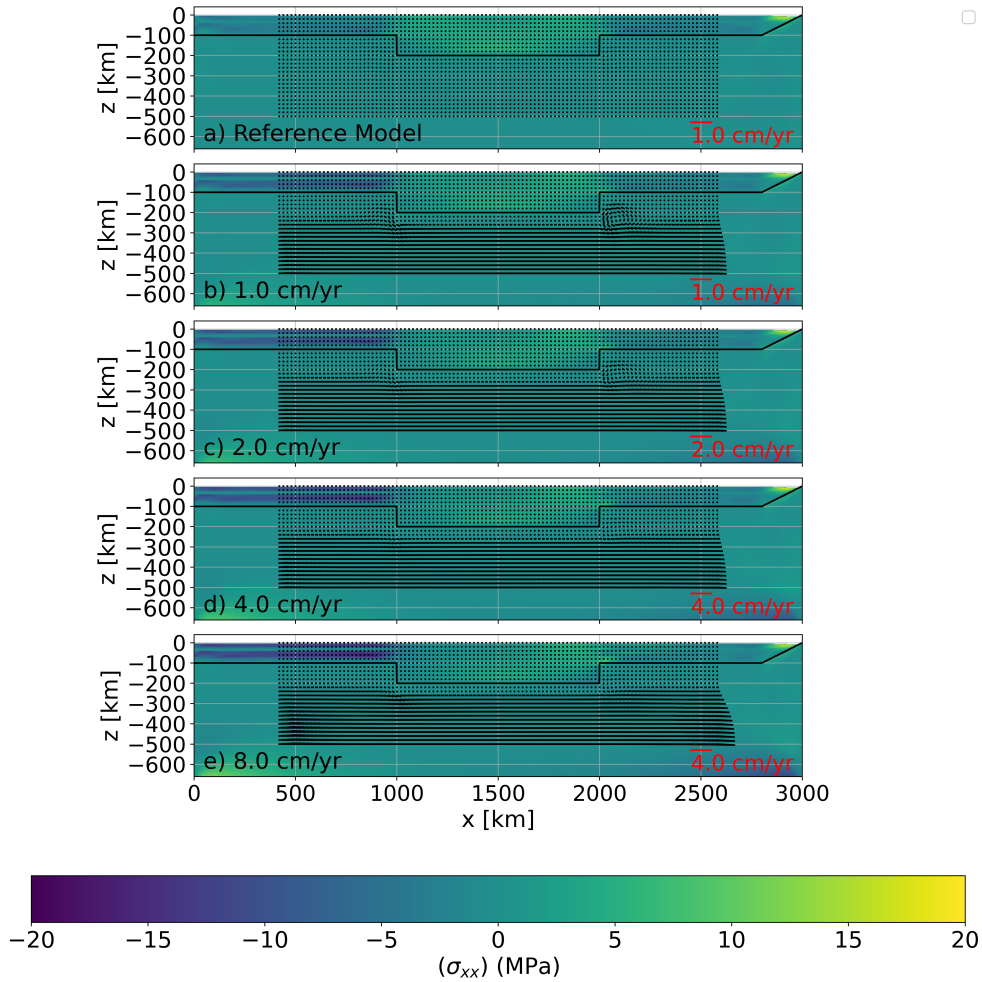

Figure 4.21: Stress field of the numerical scenarios of Group IV with a decoupled lithosphere ($C_{lc} = 1$), after 40 Myr, with a cratonic keel of 100 km thick, and, with a relative velocity between the lithosphere and the base of the model varying between $v_r = 0 - 8$ cm/year. The black line delimits the lithosphere. Observe that the scale of the velocity vector, indicated in red, varies among the graphs.

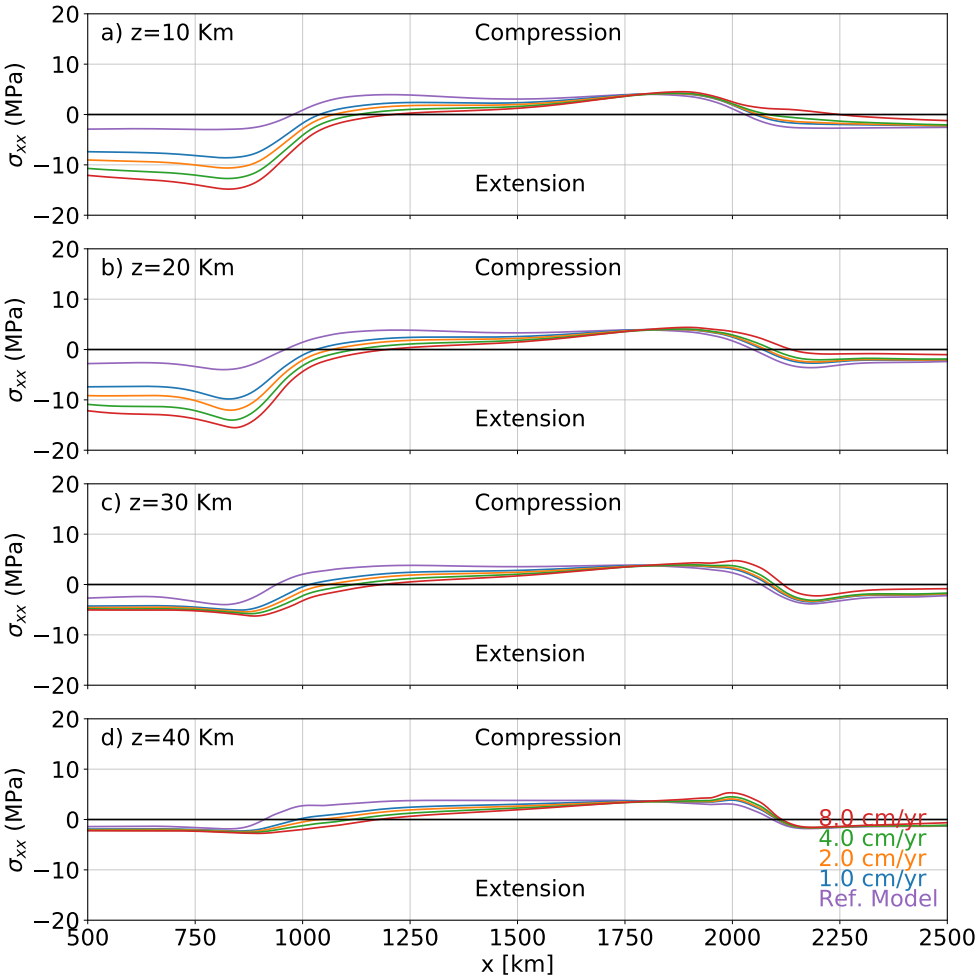

Figure 4.22: Stress profile after 40 Myr of the numerical scenarios of Group IV with a decoupled lithosphere ($C_{lc} = 1$), with a cratonic keel of 100 km thick, and, with a relative velocity between the lithosphere and the base of the model varying between $v_r = 0 - 8$ cm/year. Profiles were taken in different depths (z). The black line delimits the extensional/compressional regime of stresses.

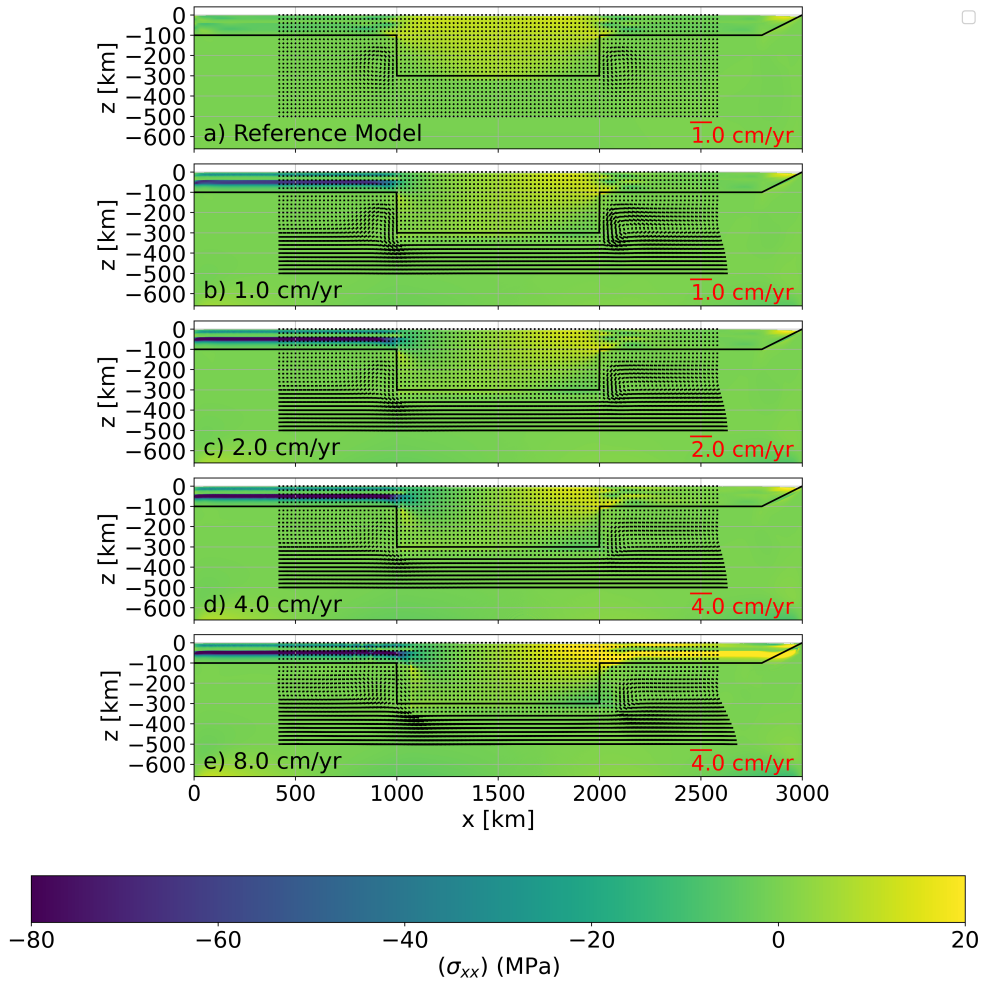

Figure 4.23: Stress field of the numerical scenarios of Group V with a decoupled lithosphere ($C_{lc} = 1$), after 40 Myr, with a cratonic keel of 200 km thick, and, with a relative velocity between the lithosphere and the base of the model varying between $v_r = 0 - 8$ cm/year. The black line delimits the lithosphere. Observe that the scale of the velocity vector, indicated in red, varies among the graphs.

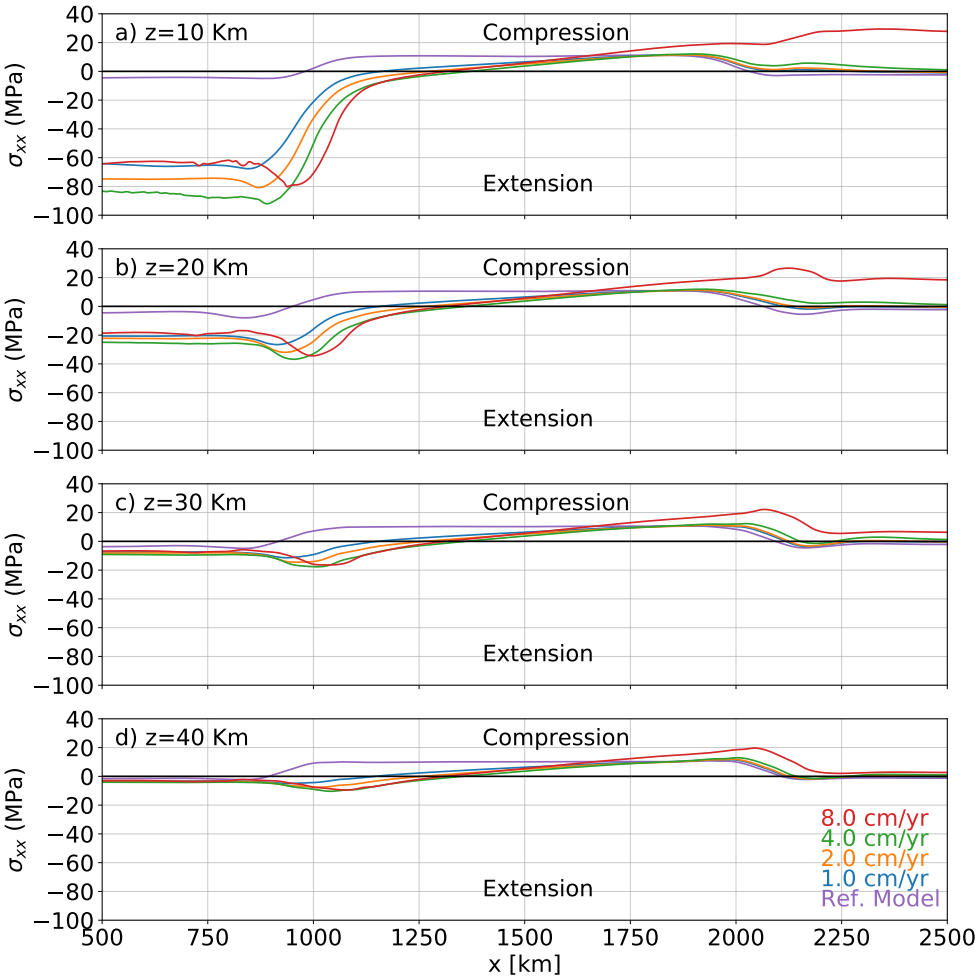

Figure 4.24: Stress profile after 40 Myr of the numerical scenarios of Group V with a decoupled lithosphere ($C_{lc} = 1$), with a cratonic keel of 200 km thick, and, with a relative velocity between the lithosphere and the base of the model varying between $v_r = 0 - 8$ cm/year. Profiles were taken in different depths (z). The black line delimits the extensional/compressional regime of stresses.

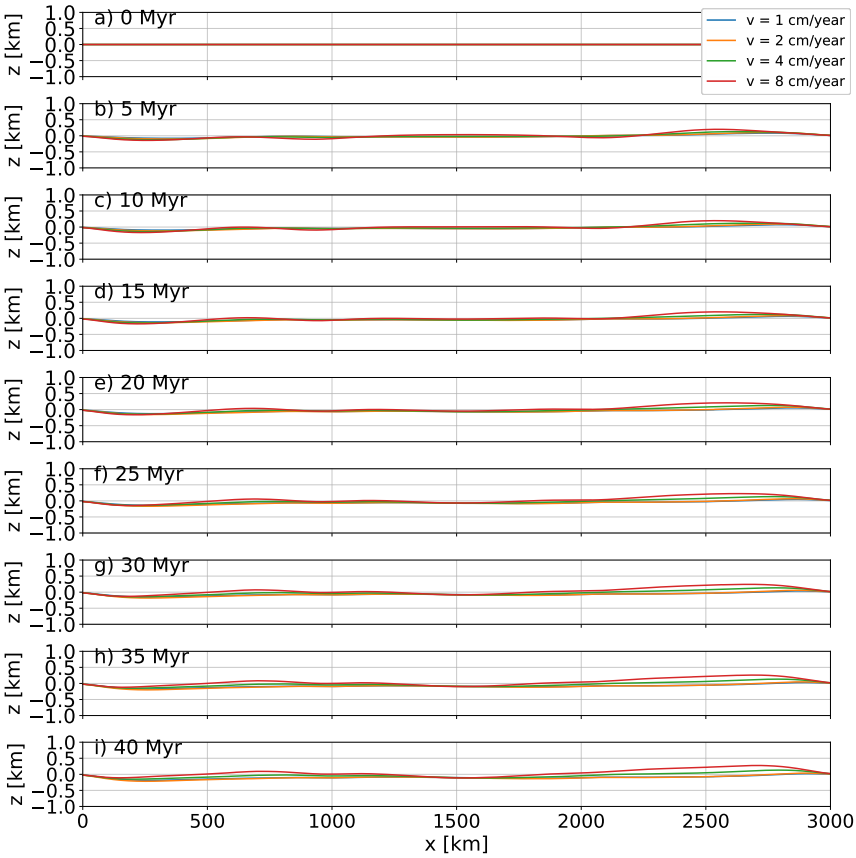

Figure 4.25: Difference between the dynamic topography from models of Group I with a velocity varying between $v_r = 1 - 8$ cm/yr and the reference model ($v_r = 0$ cm/yr) with a cratonic keel of 100 km thick, and a coupled lithosphere ($C_{lc} = 10$).

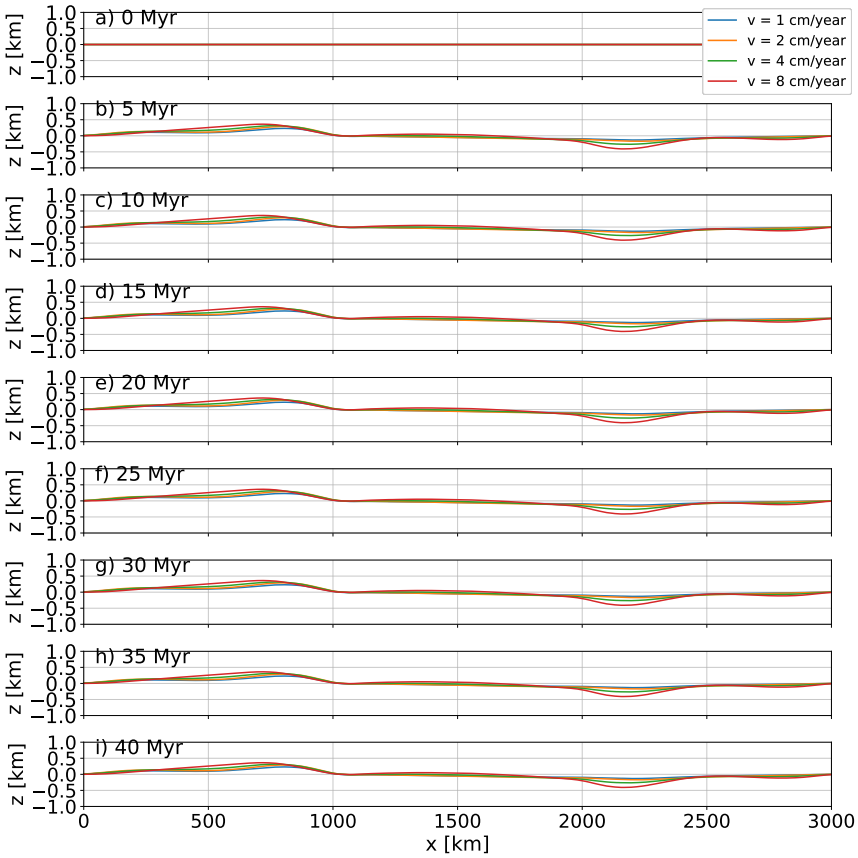

Figure 4.26: Difference between the dynamic topography from models of Group II with a velocity varying between $v_r = 1 - 8$ cm/yr and the reference model ($v_r = 0$ cm/yr) with a cratonic keel of 200 km thick, and a coupled lithosphere ($C_{lc} = 10$).

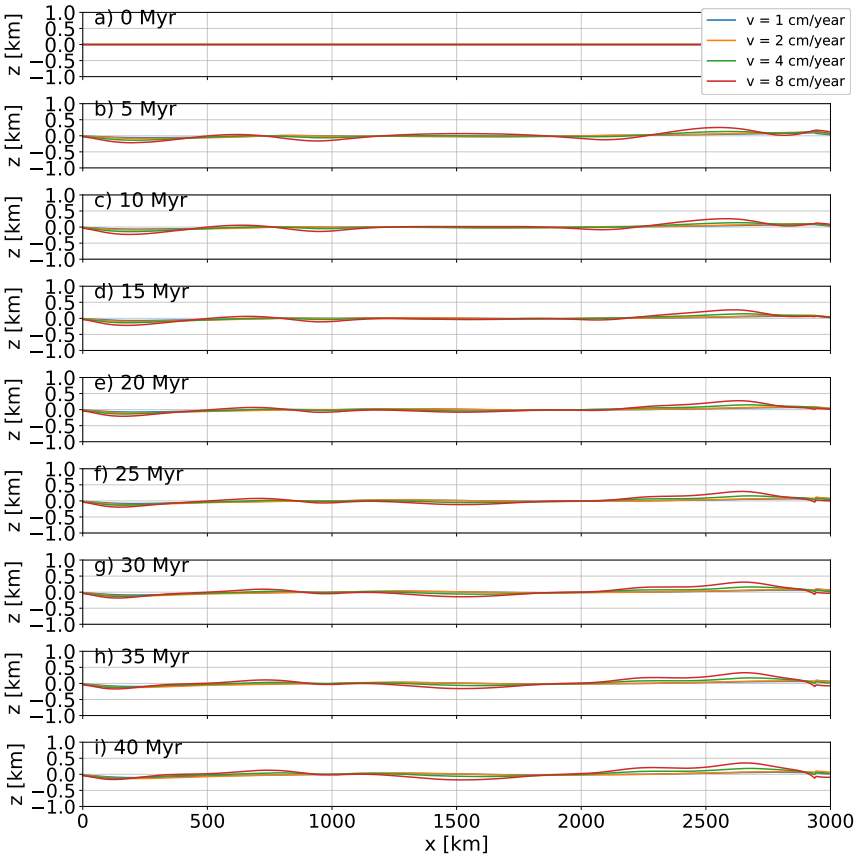

Figure 4.27: Difference between the dynamic topography from models of Group IV with a velocity varying between $v_r = 1 - 8$ cm/yr and the reference model ($v_r = 0$ cm/yr) with a cratonic keel of 100 km thick, and a coupled lithosphere ($C_{lc} = 10$).

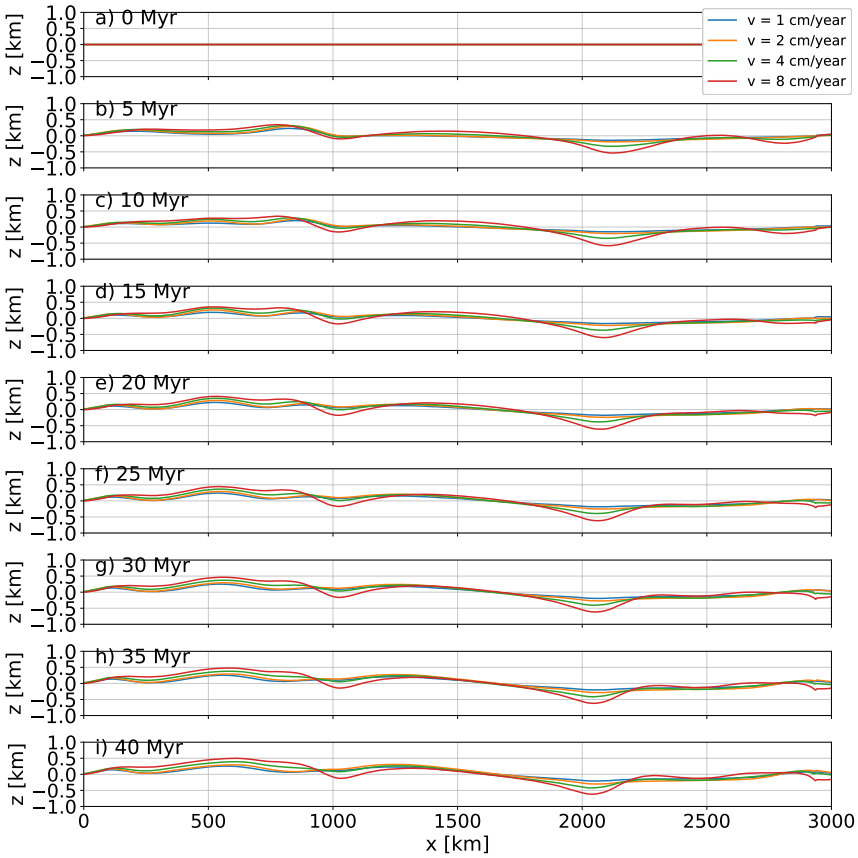

Figure 4.28: Difference between the dynamic topography from models of Group V with a velocity varying between $v_r = 1 - 8$ cm/yr and the reference model ($v_r = 0$ cm/yr) with a cratonic keel of 200 km thick, and a coupled lithosphere ($C_{lc} = 10$).

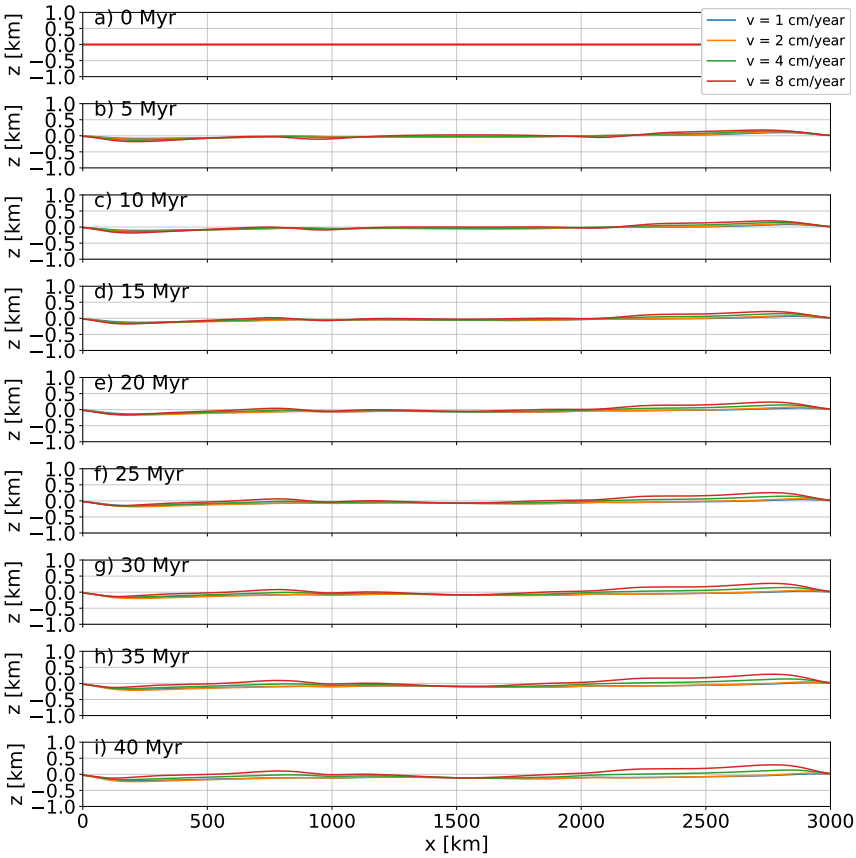

Figure 4.29: Difference between the dynamic topography from models of Group I with a velocity varying between $v_r = 1 - 8$ cm/yr and the reference model ($v_r = 0$ cm/yr) with a cratonic keel of 100 km thick, and a decoupled lithosphere ($C_{lc} = 1$).

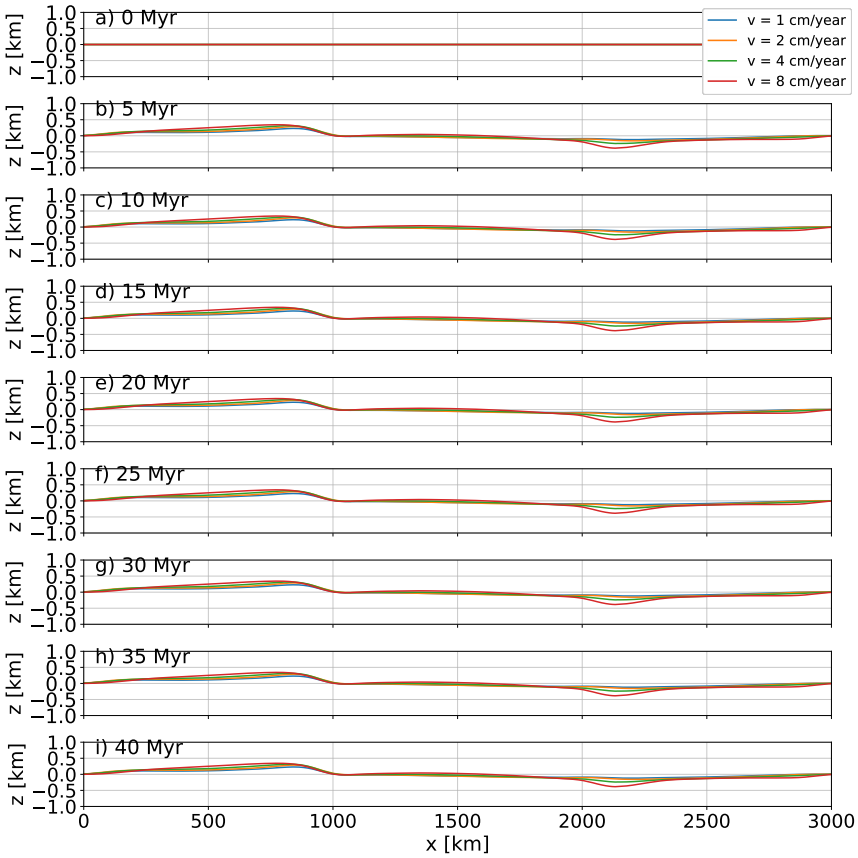

Figure 4.30: Difference between the dynamic topography from models of Group II with a velocity varying between $v_r = 1 - 8$ cm/yr and the reference model ($v_r = 0$ cm/yr) with a cratonic keel of 200 km thick, and a decoupled lithosphere ($C_{lc} = 1$).

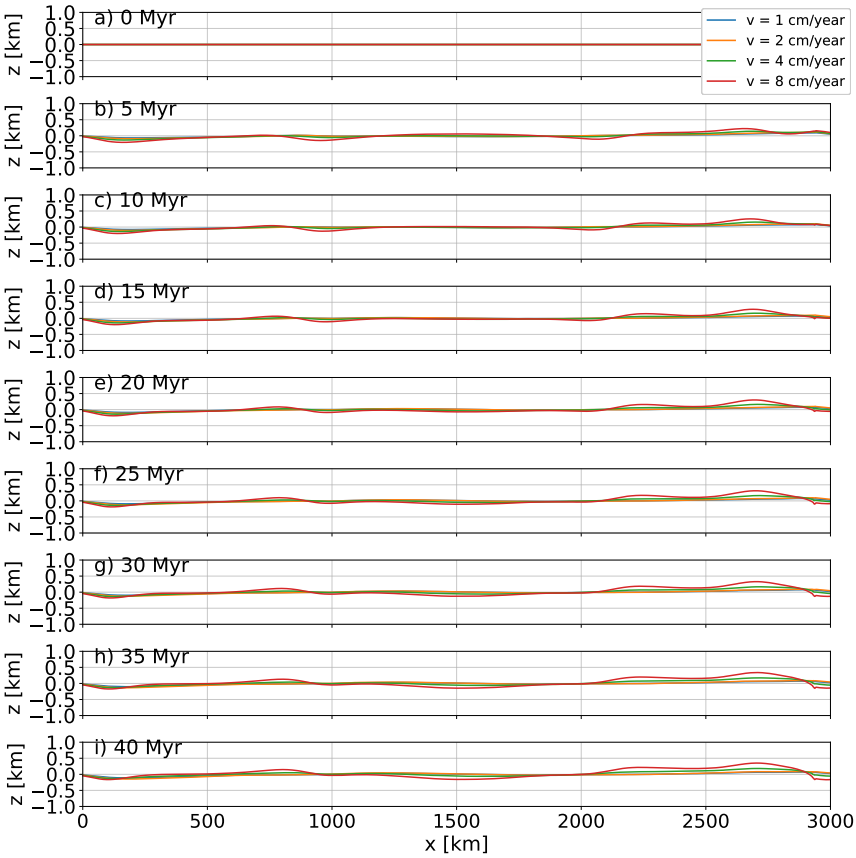

Figure 4.31: Difference between the dynamic topography from models of Group IV with a velocity varying between $v_r = 1 - 8$ cm/yr and the reference model ($v_r = 0$ cm/yr) with a cratonic keel of 100 km thick, and a decoupled lithosphere ($C_{lc} = 1$).

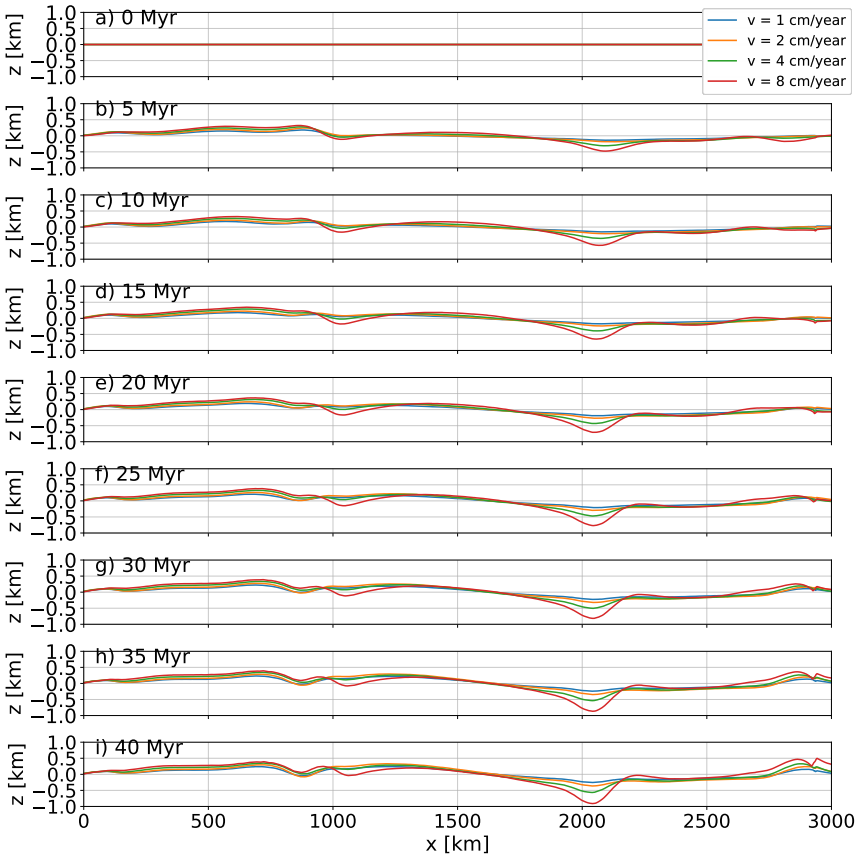

Figure 4.32: Difference between the dynamic topography from models of Group V with a velocity varying between $v_r = 1 - 8$ cm/yr and the reference model ($v_r = 0$ cm/yr) with a cratonic keel of 200 km thick, and a decoupled lithosphere ($C_{lc} = 1$).

Chapter 5

Discussion

5.1 *Dynamic topography induced by asthenospheric flow under cratonic keels*

Dynamic topography is the topographic perturbation induced by the convective movement in the mantle and consequent stresses at the base of the lithosphere. This topography component differs from the isostatic or "tectonic" topography (Braun, 2010) because it only persists while there is convection in the mantle. Upward movement in the asthenosphere induces positive dynamic topography while downward movement induces a regional subsidence.

In the numerical scenarios, the imposition of a relative velocity between the lithosphere and the base of the upper mantle perturbed the convective pattern in the mantle, especially enhancing the edge-driven convection along the cratonic stern, i.e. when the asthenospheric flow occurs from the cratonic keel towards the thinner lithospheric portion (Figure 5.1). This is especially visible in the coupled and decoupled scenarios of Groups II and V, where the cratonic keel is thicker (Figures 4.3b-e, 4.9b-e, 4.19b-e, and 4.23b-e). In these scenarios, the downward movement of the edge-driven convection adjacent to the craton induces negative dynamic topography (subsidence) with a wavelength of $\sim$ 300 km and amplified magnitude for the scenarios with faster relative velocity (Figures 4.26, 4.28, 4.30, and 4.32). The topographic perturbations in the numerical scenarios are calculated assuming an air-loaded condition. Therefore, the amplitude S of a few hundred meters of subsidence along the cratonic stern can be amplified due to the load of water and/or sedimentary layer. For simplicity, assuming local isostasy, the amplification in the vertical displacement $w = S\rho_i/(\rho_m - \rho_i)$, where ρ_i is the density of the infilling material, can be

$w \approx 0.43h$ for water ($\rho_i = 1000$ kg/m^3) and $w = 2h$ for sedimentary layer with mean density $\rho_i = 2200$ kg/m^3. Therefore, the total subsidence $S + w$ can be of the order of one kilometer considering the load of the sedimentary layers.

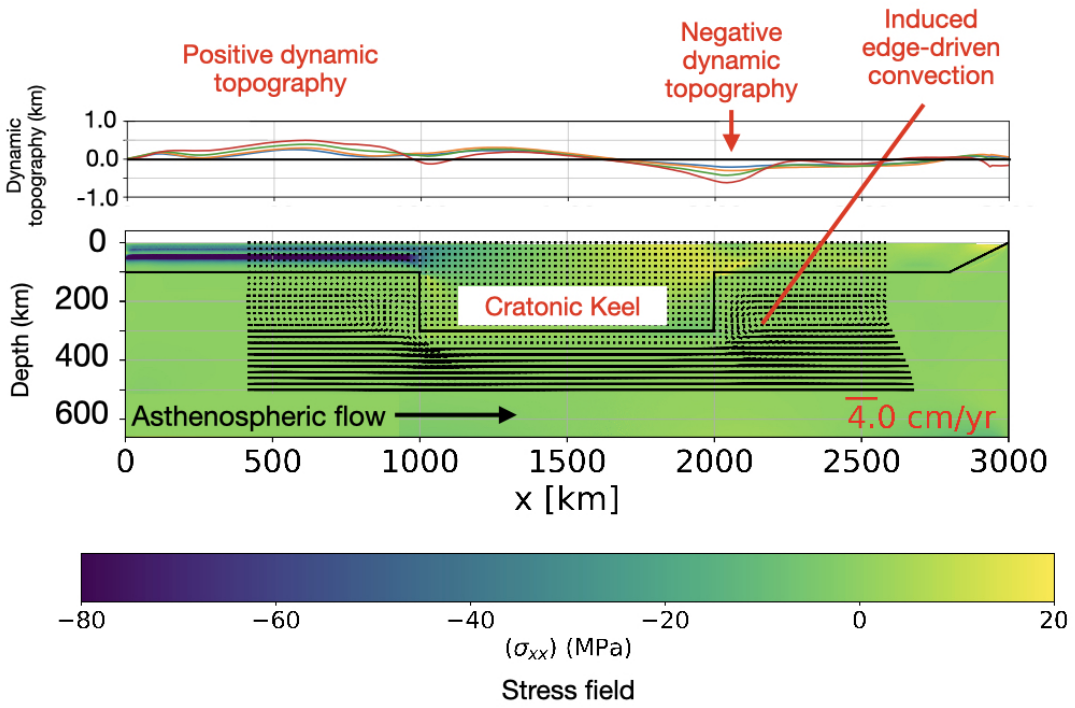

Figure 5.1: A graphical summary of the numerical results of the coupled scenario of Group V with a cratonic keel of 200 km, $C_{lc} = 10$, and $v_r = 8$ cm/yr. Showing the main features observed in the model.

One plate that presents a thick cratonic keel with more than 200 km and a high velocity (∼7.4 cm/year) with respect to HS3-NUVEL-1A hotspot reference frame is the Australian Plate. The speed of the northward movement of Australia towards Southeastern Asia is anomalously high relative to other plates with thick continental lithosphere (Figure 1.1) and is mainly guided by the subduction of oceanic slabs along the New Guinea–Pocklington subduction zone (Schellart and Spakman, 2015).

The Australian Plate combines the ingredients to create vigorous edge-driven convection along the cratonic stern, which represents the southern portion of Australia. This region is characterized by a regional negative anomalous topography (Czarnota et al., 2013) of the order of 1 km that cannot be explained by simple isostatic equilibrium (see dots in Figure 5.2).

The wavelength of the negative dynamic topography predicted in our model of approxi-

mately 300 km is probably superposed to a long wavelength negative dynamic topography centered on the Australian–Antarctic discordance (Sandiford, 2007). The northward movement of the plate induced the continuous displacement of the southern margin outside this long wavelength negative dynamic topography (Sandiford, 2007), creating a N-S tilt of the entire continent, resulting in a continuous uplift and consequent decrease of the magnitude of the negative dynamic topography in the southern portion of Australia since the Miocene (Czarnota et al., 2013). The modeled magnitude of the long wavelength dynamic topography is of the order of -250 and -300 m southward of Australia (Heine et al., 2010), assuming a water-loaded scenario. Therefore, I propose that the magnitude of dynamic topography along the southern margin of Australia can be explained by the combination of long-wavelength features induced by deeper components of mantle convection superposed with the subsidence induced by edge-driven convection in the upper mantle.

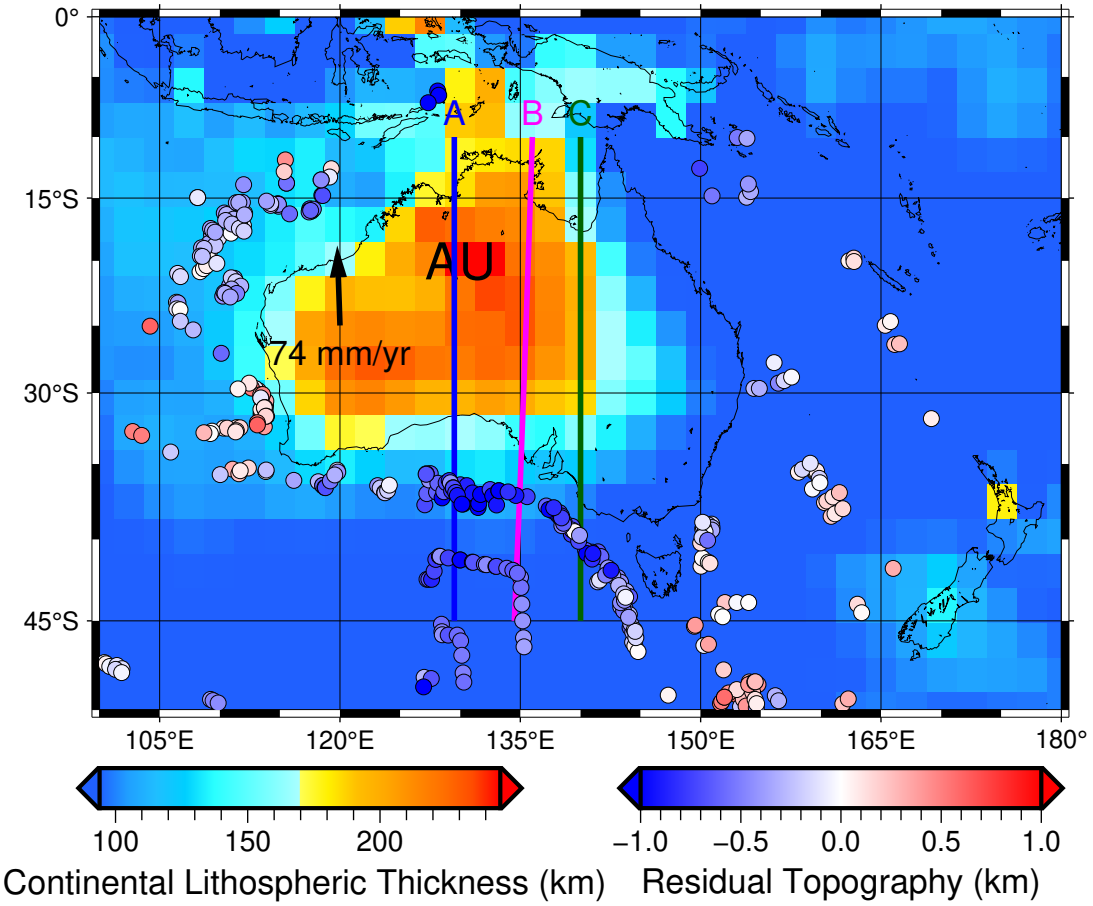

Figure 5.2: Map of the continental lithospheric thickness and residual topography of the Australian Plate. The continental lithospheric thickness data extracted from Priestley and McKenzie (2013) and topography data from Czarnota et al. (2013).

Furthermore, the N-S continental tilt (Sandiford, 2007) can be partially explained by

the decrease in the absolute northward speed of Australia since 30 Ma (see Figure 1a in Schellart and Spakman, 2015), with a decrease estimated in 2 cm/year during this time interval. Based on the numerical scenarios, I expect that the plate slowdown results in a decrease in the amplitude of the dynamic topography (compare the different curves in Figure 4.28). As a consequence, the cratonic stern is uplifted and the region adjacent to the cratonic bow subsides, reproducing the continental tilt as observed in Australia. Therefore, the numerical scenarios indicate that the absolute value of dynamic topography is positive along the adjacent margin of the cratonic bow and negative along the cratonic stern margin, but changes in the speed of the lithospheric plate through the geological time can modulate the amplitude of the dynamic topography, inducing uplift or subsidence.

It is important to highlight that the numerical scenarios do not take into account the influence of the subducting slab and the consequent influence on mantle convection. Therefore, we cannot reproduce the complex convective pattern of northern Australia due to the proximity to the New Guinea–Pocklington subduction zone.

5.2 Influence of the asthenospheric flow under cratonic keels on the crustal stress state

The numerical models with different relative plate velocities show that higher velocities induce higher horizontal deviatoric stress in the lithosphere, which agrees with the velocity having a direct relation to the basal drag force exerted on the lithosphere by the asthenospheric flow (Turcotte and Schubert, 2014). Varying the velocity from 1 to 8 cm/year increased the lithospheric stress by a factor of 2 to 4. Furthermore, the thin asthenospheric layer beneath the cratonic keel increases shear traction from viscous drag (Conrad and Lithgow-Bertelloni, 2006; van Summeren et al., 2012).

Models with a velocity of $v_r = 4$ cm/year and a cratonic keel 100 km thick which resembles the velocity and the cratonic thickness for the South American Plate (Figure 1.1) produced horizontal deviatoric stress of approximately 7 MPa. For the South American Plate, the magnitude of the lithospheric stress is around $20 - 30$ MPa (Figure 5.3 Assumpção et al., 2016; Coblentz and Richardson, 1996), so the stress induced by the asthenospheric mantle flow alone can explain $20\% - 30\%$ of the total lithospheric stress.

Models with a velocity of $v_r = 1 - 2$ cm/year and a cratonic keel 100 km thick which

resembles the velocity and cratonic thickness for the African Plate (Figure 1.1) produced horizontal deviatoric stress of approximately $3 - 5$ MPa of magnitude. Coblentz and Sandiford (1994) predicted tectonic stresses in continental Africa to varying from $8 - 15$ MPa, so the models could reproduce about 20% of the total lithospheric stress.

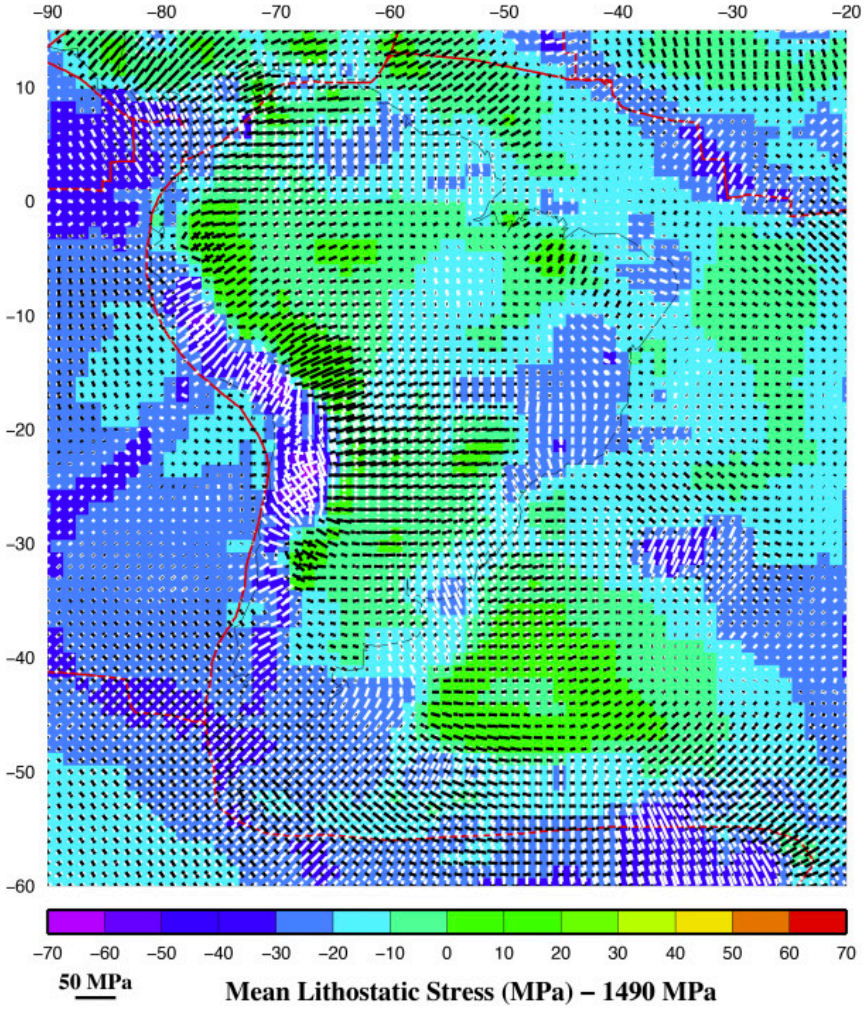

Figure 5.3: Main stresses due to Gravitational Potential Energy (GPE) calculated from lateral density variations based on the CRUST1.0 model. Extracted from Assumpção et al. (2016)

For the Australian Plate, there are lateral variations in the continental thickness (Farrington et al., 2010), so we decided to compare both models with a cratonic keel of 100 and 200 km thick and velocity $v_r = 8$ cm/year. We extracted the predicted stresses for three different profiles (Figure 5.2) across the Australian continent from Reynolds et al. (2002), which considered three tectonic processes to model the forces acting on the Indo-Australian Plate: First, they accounted for intraplate sources related to lateral variations in gravitational potential energy in the lithosphere. This includes ridge push and buoyancy forces associated with continental margins and elevated continental crust. Second, it considered

plate boundary forces, which account for collisional and subduction boundaries, mostly in the northern region and at the New Zealand boundary. Lastly, drag forces acting on the base of the plate were considered, but these forces were primarily used to balance the net torque acting on the plate.

The extracted σ_{xx} and σ_{yy} for continental Australia needed to be transformed into a system of coordinates equivalent to the direction of the plate velocity. This transformation is achieved using the following equation:

$$\sigma'_{xx} = \sigma_{xx}cos\theta + \sigma_{yy}sin\theta + 2\tau_{xy}sin\theta cos\theta \tag{5.1}$$

where θ is the angle between the σ_{xx} component of the principal stress and the direction of the movement of the plate.

In the scenario with a cratonic keel of 100 km thickness, the horizontal stresses had maximum magnitudes of approximately $7 - 9$ MPa, and Reynolds et al. (2002) predicted that the lithospheric stress is approximately $9 - 25$ MPa (Figure 5.4). So the deviatoric stresses produced by the interaction of asthenospheric flow with the base of the lithosphere in this scenario can represent a portion of the total stresses in continental Australia. On the other hand, in the numerical scenario with a thicker cratonic keel (200 km thick), the stresses resulting from the relative motion of the lithosphere reach magnitudes of almost 20 MPa of compressional stresses in the upper crust in the region equivalent to the southern portion of the Australia continent, compatible with the magnitude predicted by Reynolds et al. (2002).

In the northern part of the continent, the numerical scenarios predicted extensional stresses, which greatly differs from Reynolds et al. (2002) which predicted compressional stresses. The numerical scenarios presented here have some limitations as the plate boundaries are not included, especially for subduction zones that can highly interfere with the mantle flow (Hu et al., 2017), or collisional boundaries that have a significant effect on the intraplate stresses (Coblentz et al., 1995, 1998; Reynolds et al., 2002), which is supposed to be the main factor for this difference, because the northern portion of the Indo-Australian Plate is surrounded by collisional boundaries (Eurasian Plate, Sumatra, New Guinea).

Also, a 2D model limits the mantle flow around a craton which on a three-dimensional model can flow in more directions and at the same time allows for more complex keel

geometries to be explored. Paul et al. (2023) show that mantle flow is diverted downward beneath thick and viscous cratonic roots, which induces compressive stress regimes within cratonic interiors. In this work, it was noticed the predominance of extensional forces in the cratonic bow and compressional efforts at the cratonic stern.

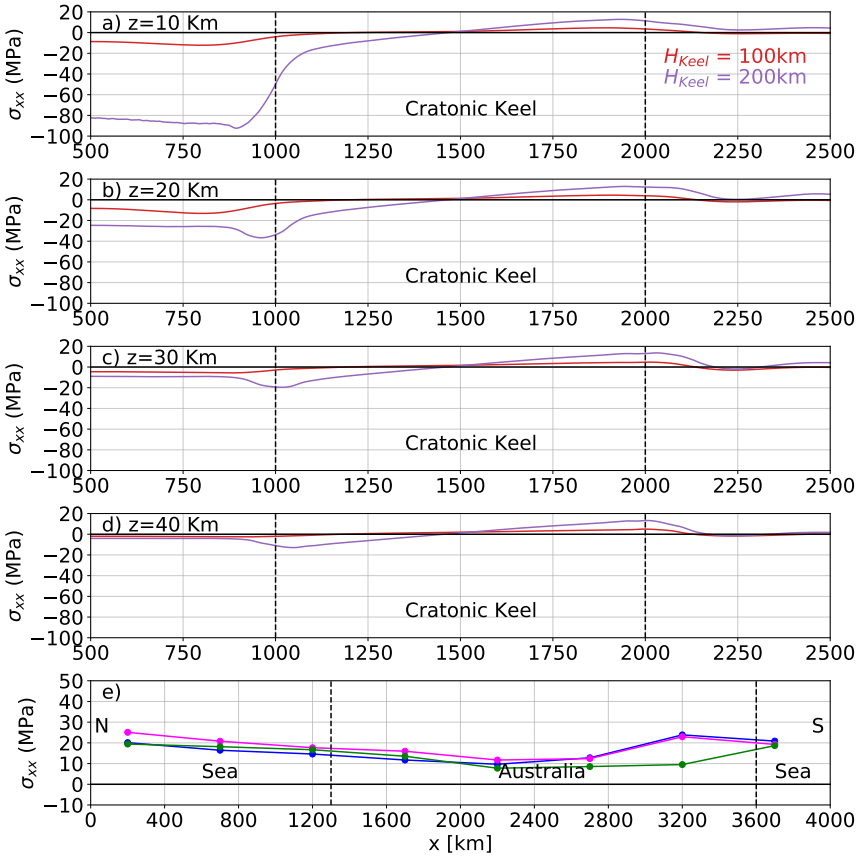

Figure 5.4: a-d) Stress profile after 40 Myr of the numerical scenarios for both models, where relative velocity between the lithosphere and the base of the model $v_r = 8$ cm/year. Profiles were taken in different depths (z). e) Data extracted from Reynolds et al. (2002). The colors are respective to the profile in Figure 5.2. The black line delimits the extensional/compressional regime of stresses.

Chapter 6

Conclusion

This thesis aimed to evaluate the interaction of asthenospheric flow with cratonic keels, using 2D thermo-mechanical numerical simulations taking into account realistic rheological behavior for the crust and mantle. These numerical scenarios showed that the asthenospheric flow under the cratonic lithosphere induced extensional stresses in the cratonic bow and compressional stresses in the cratonic stern. The magnitude of the deviatoric stress induced by this asthenospheric flow affects the stresses in the entire lithospheric plate, with an important impact on the upper crust. Moreover, the relative velocity between the lithosphere and the base of the upper mantle and the cratonic thickness influence the magnitude of the intraplate stress, with higher velocities and thicker cratons increasing the magnitude of the stresses. Another aspect that can influence the magnitude of the stresses in the lithosphere is the degree of coupling between the upper crust, and the lithospheric mantle. A higher degree of coupling makes the lithospheric plate more rigid implying lower intraplate stresses. On the other hand, a decoupled lithosphere, being less rigid, is more susceptible to the basal drag and presents stresses of higher magnitudes.

The edge-driven convection adjacent to the cratonic lithosphere is affected by the horizontal asthenospheric flow induced by the lithospheric movement relative to the base of the upper mantle. It is reduced along the cratonic bow and amplified along the cratonic stern. In the scenarios with a thick cratonic keel (200 km), the vigor of the edge-driven convection along the cratonic stern is sufficient to induce negative dynamic topography of hundreds of meters, which can be amplified with the load of water and sediments.

The numerical results can explain part of the regional topographic and bathymetric evolution of Australia predicting a regional subsidence along the southern margin.

Additionally, the slowdown of the northward movement of the Australian plate during

the last 30 Ma could have contributed to a decrease in the amplitude of the dynamic topography perturbation, resulting in a relative uplift of the southern margin of Australia and a relative subsidence along the northern margin, partially explaining the N-S continental tilt of the plate.

This thesis provided important insights into the complex interaction between the asthenospheric mantle dynamics and thick cratonic keel, highlighting its influences on the lithospheric stresses, and dynamic topography. However, 2D models have limitations when considering the inherently three-dimensional nature of geological processes. Therefore, the use of 3D is necessary to address some aspects as the plate boundaries and the asthenospheric flow around cratonic keels in more complex geometries.

Bibliography

Alboussière T., Ricard Y., Reflections on dissipation associated with thermal convection, Journal of Fluid Mechanics, 2013, vol. 725, p. R1

Andrés-Martínez M., Pérez-Gussinyé M., Armitage J., Morgan J. P., Thermomechanical implications of sediment transport for the architecture and evolution of continental rifts and margins, Tectonics, 2019, vol. 38, p. 641

Assumpção M., Dias F. L., Zevallos I., Naliboff J. B., Intraplate stress field in South America from earthquake focal mechanisms, Journal of South American Earth Sciences, 2016, vol. 71, p. 278

Balay S., Abhyankar S., Adams M. F., Benson S., Brown J., Brune P., Buschelman K., Constantinescu E., Dalcin L., Dener A., Eijkhout V., Faibussowitsch J., Gropp W. D., Hapla V., Isaac T., Jolivet P., Karpeev D., Kaushik D., Knepley M. G., Kong F., Kruger S., May D. A., McInnes L. C., Mills R. T., Mitchell L., Munson T., Roman J. E., Rupp K., Sanan P., Sarich J., Smith B. F., Zampini S., Zhang H., Zhang H., Zhang J., , 2022 Technical Report ANL-21/39 - Revision 3.18 PETSc/TAO Users Manual. Argonne National Laboratory

Bird P., An updated digital model of plate boundaries, Geochemistry, Geophysics, Geosystems, 2003, vol. 4

Braun J., The many surface expressions of mantle dynamics, Nature Geoscience, 2010, vol. 3, p. 825

Brooks A. N., Hughes T. J., Streamline upwind/Petrov-Galerkin formulations for convection dominated flows with particular emphasis on the incompressible Navier-Stokes

equations, Computer Methods in Applied Mechanics and Engineering, 1982, vol. 32, p. 199

Burov E., Watts A., et al., The long-term strength of continental lithosphere:"jelly sandwich"or"crème brûlée"?, GSA today, 2006, vol. 16, p. 4

Burov E. B., Rheology and strength of the lithosphere, Marine and petroleum Geology, 2011, vol. 28, p. 1402

Byerlee J. D., Brittle-ductile transition in rocks, Journal of Geophysical Research (1896-1977), 1968, vol. 73, p. 4741

Byerlee J. D., , 1978 in , Rock friction and earthquake prediction. Springer pp 615–626

Christensen U. R., Yuen D. A., Layered convection induced by phase transitions, Journal of Geophysical Research: Solid Earth, 1985, vol. 90, p. 10291

Coblentz D. D., Richardson R. M., Analysis of the South American intraplate stress field, Journal of Geophysical Research: Solid Earth, 1996, vol. 101, p. 8643

Coblentz D. D., Sandiford M., Tectonic stresses in the African plate: Constraints on the ambient lithospheric stress state, Geology, 1994, vol. 22, p. 831

Coblentz D. D., Sandiford M., Richardson R. M., Zhou S., Hillis R., The origins of the intraplate stress field in continental Australia, Earth and Planetary Science Letters, 1995, vol. 133, p. 299

Coblentz D. D., Zhou S., Hillis R. R., Richardson R. M., Sandiford M., Topography, boundary forces, and the Indo-Australian intraplate stress field, Journal of Geophysical Research: Solid Earth, 1998, vol. 103, p. 919

Conrad C. P., Lithgow-Bertelloni C., Influence of continental roots and asthenosphere on plate-mantle coupling, Geophysical Research Letters, 2006, vol. 33

Cooper C., Lenardic A., Moresi L., The thermal structure of stable continental lithosphere within a dynamic mantle, Earth and Planetary Science Letters, 2004, vol. 222, p. 807

Crameri F., Schmeling H., Golabek G. J., Duretz T., Orendt R., Buiter S. J. H., May D. A., Kaus B. J. P., Gerya T. V., Tackley P. J., A comparison of numerical surface topography calculations in geodynamic modelling: an evaluation of the 'sticky air' method, Geophysical Journal International, 2012, vol. 189, p. 38

Curbelo J., Duarte L., Alboussiere T., Dubuffet F., Labrosse S., Ricard Y., Numerical solutions of compressible convection with an infinite Prandtl number: comparison of the anelastic and anelastic liquid models with the exact equations, Journal of Fluid Mechanics, 2019, vol. 873, p. 646

Czarnota K., Hoggard M. J., White N., Winterbourne J., Spatial and temporal patterns of Cenozoic dynamic topography around Australia, Geochemistry, Geophysics, Geosystems, 2013, vol. 14, p. 634

Doin M.-P., Fleitout L., Christensen U., Mantle convection and stability of depleted and undepleted continental lithosphere, Journal of Geophysical Research, 1997, vol. 102, p. 2771

Drucker D. C., Prager W., Soil mechanics and plastic analysis or limit design, Quarterly of applied mathematics, 1952, vol. 10, p. 157

Farrington R. J., Stegman D. R., Moresi L. N., Sandiford M., May D. A., Interactions of 3D mantle flow and continental lithosphere near passive margins, Tectonophysics, 2010, vol. 483, p. 20

Forsyth D., Uyeda S., On the relative importance of the driving forces of plate motion, Geophysical Journal International, 1975, vol. 43, p. 163

Gassmöller R., Dannberg J., Bangerth W., Heister T., Myhill R., On formulations of compressible mantle convection, Geophysical Journal International, 2020, vol. 221, p. 1264

Gerya T., Introduction to Numerical Geodynamic Modelling. Cambridge University Press, 2019

Gleason G. C., Tullis J., A flow law for dislocation creep of quartz aggregates determined with the molten salt cell, Tectonophysics, 1995, vol. 247, p. 1

Gripp A. E., Gordon R. G., Young tracks of hotspots and current plate velocities, Geophysical Journal International, 2002, vol. 150, p. 321

Heine C., Müller R. D., Steinberger B., DiCaprio L., Integrating deep Earth dynamics in paleogeographic reconstructions of Australia, Tectonophysics, 2010, vol. 483, p. 135

Hu J., Faccenda M., Liu L., Subduction-controlled mantle flow and seismic anisotropy in South America, Earth and Planetary Science Letters, 2017, vol. 470, p. 13

Jarvis G. T., Mckenzie D. P., Convection in a compressible fluid with infinite Prandtl number, Journal of Fluid Mechanics, 1980, vol. 96, p. 515

Jordan T. H., The continental tectosphere, Reviews of Geophysics, 1975, vol. 13, p. 1

Karato S., Wu P., Rheology of the upper mantle: a synthesis., Science (New York, N.Y.), 1993, vol. 260, p. 771

King S. D., Archean cratons and mantle dynamics, Earth and Planetary Science Letters, 2005, vol. 234, p. 1

King S. D., Anderson D. L., Edge-driven convection, Earth and Planetary Science Letters, 1998, vol. 160, p. 289

King S. D., Ritsema J., African hot spot volcanism: small-scale convection in the upper mantle beneath cratons, Science, 2000, vol. 290, p. 1137

Landau L. D., Lifshitz E. M., Fluid Mechanics. vol. 6, Pergamon Press, 1987, 539

Landau L. D., Lifshitz E. M., Kosevich A. M., Pitaevskii L. P., Theory of elasticity: volume 7. vol. 7, Elsevier, 1986

Lenardic A., Moresi L.-N., Mühlhaus H., Longevity and stability of cratonic lithosphere: insights from numerical simulations of coupled mantle convection and continental tectonics, Journal of Geophysical Research: Solid Earth, 2003, vol. 108

Leng W., Zhong S., Viscous heating, adiabatic heating and energetic consistency in compressible mantle convection, Geophysical Journal International, 2008, vol. 173, p. 693

Lithgow-Bertelloni C., Richards M. A., The dynamics of Cenozoic and Mesozoic plate motions, Reviews of Geophysics, 1998, vol. 36, p. 27

Mckenzie D., Bickle M., The volume and composition of melt generated by extension of the lithosphere, Journal of petrology, 1988, vol. 29, p. 625

Moresi L., Solomatov V., Mantle convection with a brittle lithosphere: thoughts on the global tectonic styles of the Earth and Venus, Geophysical Journal International, 1998, vol. 133, p. 669

O'Neill C., Lenardic A., Griffin W., O'Reilly S. Y., Dynamics of cratons in an evolving mantle, Lithos, 2008, vol. 102, p. 12

Paul J., Conrad C. P., Becker T. W., Ghosh A., Convective Self-Compression of Cratons and the Stabilization of Old Lithosphere, Geophysical Research Letters, 2023, vol. 50, p. e2022GL101842

Petersen K. D., Nielsen S. B., Clausen O. R., Stephenson R., Gerya T. V., Small-scale mantle convection produces stratigraphic sequences in sedimentary basins, Science (New York, N.Y.), 2010, vol. 329, p. 827

Pollack H. N., Cratonization and thermal evolution of the mantle, Earth and Planetary Science Letters, 1986, vol. 80, p. 175

Priestley K., McKenzie D., The relationship between shear wave velocity, temperature, attenuation and viscosity in the shallow part of the mantle, Earth and Planetary Science Letters, 2013, vol. 381, p. 78

Rayleigh LIX. On convection currents in a horizontal layer of fluid, when the higher temperature is on the under side, The London, Edinburgh, and Dublin Philosophical Magazine and Journal of Science, 1916, vol. 32, p. 529

Reynolds S. D., Coblentz D. D., Hillis R. R., Tectonic forces controlling the regional intraplate stress field in continental Australia: Results from new finite element modeling, Journal of Geophysical Research: Solid Earth, 2002, vol. 107, p. ETG

Ricard Y., , 2015 in Schubert G., ed., , Treatise on Geophysics, Volume 7. Mantle Dynamics 2nd edn, Elsevier Oxford pp 23 – 71

Sacek V., Post-rift influence of small-scale convection on the landscape evolution at divergent continental margins, Earth and Planetary Science Letters, 2017, vol. 459, p. 48

Sacek V., Assunção J., Pesce A., da Silva R. M., Mandyoc: A finite element code to simulate thermochemical convection in parallel, Journal of Open Source Software, 2022, vol. 7, p. 4070

Sacek V., Ussami N., Upper mantle viscosity and dynamic subsidence of curved continental margins, Nature Communications, 2013, vol. 4, p. 1

Salazar-Mora C. A., Huismans R. S., Fossen H., Egydio-Silva M., The Wilson cycle and effects of tectonic structural inheritance on rifted passive margin formation, Tectonics, 2018, vol. 37, p. 3085

Salazar-Mora C. A., Sacek V., Lateral flow of thick continental lithospheric mantle during tectonic quiescence, Journal of Geodynamics, 2021, vol. 145, p. 101830

Sandiford M., The tilting continent: a new constraint on the dynamic topographic field from Australia, Earth and Planetary Science Letters, 2007, vol. 261, p. 152

Schellart W. P., Spakman W., Australian plate motion and topography linked to fossil New Guinea slab below Lake Eyre, Earth and Planetary Science Letters, 2015, vol. 421, p. 107

Schubert G., Turcotte D. L., Olson P., Mantle convection in the earth and planets 1st edn. Cambridge Monographs on Mechan, Cambridge University Press, 2001

Shahnas M. H., Pysklywec R. N., Anomalous topography in the western Atlantic caused by edge-driven convection, Geophysical research letters, 2004, vol. 31

Silva R. d., Sacek V., Influence of Surface Processes on Postrift Faulting During Divergent Margins Evolution, Tectonics, 2022, vol. 41, p. e2021TC006808

Steinberger B., Becker T. W., A comparison of lithospheric thickness models, Tectonophysics, 2016

Turcotte D., Schubert G., Geodynamics 3rd edn. Cambridge University Press, 2014, 636

van Summeren J., Conrad C. P., Lithgow-Bertelloni C., The importance of slab pull and a global asthenosphere to plate motions, Geochemistry, Geophysics, Geosystems, 2012, vol. 13

Zhong S., Yuen D., Moresi L., , 2007 in Schubert G., ed., , Treatise on Geophysics. Elsevier Amsterdam pp 227 – 252